# Athermal Photonic Devices and Circuits on a Silicon Platform

by

Vivek Raghunathan

B.Tech., Metallurgical and Materials Science and Engineering,
Indian Institute of Technology Madras (2007)

Submitted to the Department of Materials Science and Engineering
in partial fulfillment of the requirements for the degree of

Doctor of Philosophy

at the

MASSACHUSETTS INSTITUTE OF TECHNOLOGY

February 2013

Author . . . . . . . . . . . . . . . . . . . . . . . . . . . . . . . . . . . . . . . . . . . . . . . . . . . . . . . .
Department of Materials Science and Engineering
January 22, 2013

Certified by . . . . . . . . . . . . . . . . . . . . . . . . . . . . . . . . . . . . . . . . . . . . . . . . . . . . .
Lionel C. Kimerling
Thomas Lord Professor of Materials Science and Engineering
Thesis Supervisor

Accepted by . . . . . . . . . . . . . . . . . . . . . . . . . . . . . . . . . . . . . . . . . . . . . . . . . . . . .
Gerbrand Ceder
Chair, Departmental Committee on Graduate Students

# Athermal Photonic Devices and Circuits on a Silicon Platform

by

Vivek Raghunathan

Submitted to the Department of Materials Science and Engineering
on January 22, 2013, in partial fulfillment of the
requirements for the degree of
Doctor of Philosophy

## Abstract

In recent years, silicon based optical interconnects has been pursued as an effective solution that can offer cost, energy, distance and bandwidth density improvements over copper. Monolithic integration of optics and electronics has been enabled by silicon photonic devices that can be fabricated using CMOS technology. However, high levels of device integration result in significant local and global temperature fluctuations that prove problematic for silicon based photonic devices. In particular, high temperature dependence of Si refractive index (thermo-optic (TO) coefficient) shifts the filter response of resonant devices that limit wavelength resolution in various applications.

Active thermal compensation using heaters and thermo-electric coolers are the legacy solution for low density integration. However, the required electrical power, device foot print and number of input/output (I/O) lines limit the integration density. We present a passive approach to an athermal design that involves compensation of positive TO effects from a silicon core by negative TO effects of the polymer cladding. In addition, the design rule involves engineering the waveguide core geometry depending on the resonance wavelength under consideration to ensure desired amount of light in the polymer. We develop exact design requirements for a TO peak stability of 0 pm/K and present prototype performance of 0.5 pm/K. We explore the material design space through initiated chemical vapor deposition (iCVD) of 2 polymer cladding choices. We study the effect of cross-linking on the optical properties of a polymer and establish the superior performance of the co-polymer cladding compared to the homo-polymer.

Integration of polymer clad devices in an electronic-photonic architecture requires the possibility of multi-layer stacking capability. We use a low temperature, high density plasma chemical vapor deposition of $SiO_2/SiN_x$ to hermetically seal the athermal. Further, we employ visible light for post-fabrication trimming of athermal rings by sandwiching a thin photosensitive layer of $As_2S_3$ in between amorphous Si core and polymer top cladding.

System design of an add-drop filter requires an optimum combination of channel counts performance and power handling capacity for maximum aggregate bandwidth. We establish the superior performance of athermal add-drop filter compared to a standard silicon filter treating bandwidth as the figure-of-merit.

Thesis Supervisor: Lionel C. Kimerling
Title: Thomas Lord Professor of Materials Science and Engineering

# Acknowledgments

My PhD at MIT started the day my advisor, Prof. Lionel C. Kimerling "Kim", embraced me into the electronic materials ("EMAT") family. I would like to thank him for introducing me to the world of photons. Under his mentorship, I had the freedom to pursue my research interests and colloborate with a lot of groups. His ability to break down a complex problem into simpler solvable ones has always guided me in the right direction everytime I hit a roadblock during a research project. His constant encouragements coupled with an amazing sense of wit make him an extremely friendly person to talk to. My thesis is a reflection of an effort to understand and validate a small fraction of what Kim knows in the field of photonics. His vision and leadership has always been a source of inspiration and are the assets that I would always refer to during the course of my career. I would like to thank Kim for everything he has done by dedicating a joke to him: "The biggest advantage of working in photonics is that there is always a light at the end of the tunnel". Thanks Kim!

I would like to take this opportunity to thank Dr. Jurgen Michel for providing me the much needed reality check during the course of my thesis. This includes demarcating the "practical solutions" and the "ideal solutions" from the list of approaches that Kim and myself would have agreed upon. He gave me a better sense of things that the scientific community actually cares about.

The EMAT mentor list is not complete without the mention of Dr.Anu Agarwal. I would like to thank her for her valuable inputs and friendly conversations that made my life easy in EMAT. She provided the much needed push in my final project and taught me the value of patience by proof-reading my thesis. I would like to thank her for her significant role in my thesis.

With a deep sense of gratitude, I wish to express my sincere thanks to the 2 non-EMAT members of my thesis committee: Prof. Michael F. Rubner and Prof. Karen K. Gleason. Their valuable inputs during the committee meetings improved the quality of my thesis by a significant amount.

EMAT would be dysfunctional without Kim's administrative assistant, Ms. Lisa

Sinclair. She is an important cog in the EMAT wheel and I would consider myself hard-working even if I do half of what she does in a day. Thanks Lisa for helping me with scheduling and rescheduling my meetings with Kim, for being patient enough to explain the travel reimbursement procedures, detailing out the shipping protocols through the EMAT account, helping with the accounting of instrument usage and for the most innovative and delicious cakes that I have ever seen and had. On a similar note, I would also like to think Ms. Angelita Mireles for being an amazing academic administrator of DMSE.

Great scientific works, more often than not, are results of collective effort of a group of intellectually curious minds working towards a common goal. My thesis stands in testimony to this statement and I take this chance to thank everyone with whom I have collaborated. Thanks to Dr.Jeujun Hu, Dr.Winnie Ye and Dr.Rong Sun of EMAT for kickstarting my PhD life at MIT by explaining the basics of my first project and helping me with fabrication and measurements. Also, thanks to Tomoyuki Izuhara from Enablence Inc for providing me with the polymer sample. My first project would not have been a success without their help. My collaboration with two polymer experts from Prof. Karen K. Gleason's group (ChemE, MIT): Dr.Jingjing Xu and Dr.Jose Luis Yague, yielded useful insights into the optical properties of the polymer and enabled me to successfully explore the material design aspect of my thesis. Optical measurement systems at Politechnico di Milano in Italy complemented the equipments that EMAT owned at MIT. This paved way for useful knowledge transfer between MIT and Politechnico di Milano. Collaboration with Prof. Andrea Melloni's group at Politechnico di Milano was just one of many collaborative efforts between our groups. Thanks to device measurements and useful discussions with Stefano Grillanda, Francesco Morichetti, Anotonio Canciamilla, and Prof.Andrea Melloni, I was able to address a crucial challenge associated with my devices. Vivek Singh and Dr.Anu Agarwal's contribution for the aforementioned collaborative effort with Politechnico Di Milano was equally valuable. Lastly, my collaboration with Shiyun Lin and Prof. Kenneth Crozier of Harvard School of Engineering triggered my interest in the system design aspect of the devices we study in this thesis.

Working in a large group like EMAT proved to be a learning experience not only because of weekly group meetings, but also due to the light-hearted conversations the group indulges in during our group outings. Everyone in the group has contributed to my personality improvement. I would like to thank everyone who are and have been a part of EMAT, during the course of my PhD, for listening to my talks, tolerating my jokes and helping me in research: Dr.Jeujun Hu, Dr.Winnie Ye, Dr.Rong Sun, Dr.Kevin A. McComber, Dr.Jifeng Liu, Dr.Jianfei Wang, Dr.Xiaochen Sun, Dr.Timothy W Zens, Dr.Lirong Zeng Broderick, Dr.Donghwan Ahn, Dr.Xiaoman Duan, Dr.Lin Zhang, Dr.Jianwei Mu, Dr.Pao Tai, Michiel Vanhoutte, Rodolfo Camacho-Aguilera, Louisa Chiao, Yan Cai, Vivek Singh, Neil Patel, Brian Albert, Brian Pearson, Wei Yu, Corentin Monmeyran and Zhaohong Han. I would also like to thank all the staff at Harvard CNS and MIT-MTL for training me and also ensuring a smooth functioning of the fabrication facility.

Life inside and outside MIT has been fun and memorable mainly due to my friends. Thanks to Kushal Kedia, Abishek Kashinath, Dr.Vikrant Vaze, Vibhu Prakash Saxena, Sarvee Diwan, Dr.Raghavendra Hosur, Harshad Kasture, Dr.Sahil Sahni, Dr.Mukul Kabir and Sriram Emani for the most helpful break sessions inside MIT. Thanks to Sumeet Kumar and Sudhish Kumar Bakku for being awesome apartment-mates and great friends. Thanks to Harish Sundaresh, Vignesh Sundaresh, Dr.Vivek Inder Sharma, Dr.Dipanjan Sen, Dr.Srikanth Patala, Chaitanya Misal, Dr.Shahriar Khushrushahi, Manish Gaurav and Ram Krishan Kumar for amazing weekends. Thanks to Dr.Varun Ramanujam, Dr.Vivek Jaiswal, Dr.Koushik Balasubramaniam, Ankur Sinha, and Nikhil Galagali for the most competitive cricket tournaments played inside MIT. Frequent chats and trips with my friends from undergraduate school; Sowmitra Singh, Tapasvi Lolla, Hridesh Kedia, Dr.Aravind R Iyengar, Dr.Amit Darbal, Vinu Rohit Krishnan, Vivek Sunder and Sebastian Thomas; have resulted in some unforgettable moments. Finally, I would like to thank my school friend, K. C. Pradeep Kumar, for all the ridiculously funny conversations.

This section would not be complete without thanking my parents, Shri.K. R.

Raghunathan and Smt.Geetha Raghunathan for their unconditional love and support. I would also like to share this moment of happiness with my loving sister Bharathi Raghunathan, my grandmother Smt. Suseela Ranganathan, my uncle Srikanth, my aunt Nirmala and my uncles Kumar and Santhanam. They rendered enormous support during the whole tenure of my research.

This thesis work has been partly sponsored under the Defense Advanced Research Projects Agency's (DARPA) Athermal Photonics Circuits (APhoCs) program. The program was executed by the Microsystems Technology Office (MTO) under Award No. W911NF-09-1-0059, Program manager: Mike Haney. It has also been partly funded by the Fully LASER integrated photonics program under APIC corporation and DARPA UHPC program.

# Contents

# List of Figures

# List of Tables

# Chapter 1

# Introduction

## 1.1 Scaling Information Technology

Ultra large scale integration (ULSI) of silicon (Si) based electronics has ensured an exponential increase in the computation performance (operations-per-second) and communication capacity (bits/second) at a constant cost in the information technology (IT) sector. Moore's law [1] governs the scaling of the chips and states that the number of integrated transistors on a chip doubles every 18 months. This is reflected in the exponential increase in the clock speed performance (Fig. (1-1)) of the microprocessors over the last 40 years [2]. However, starting in 2002, the observed increase in the computation performance (Giga operations per second, GOPS) has not been consistent with the expected increase based on the transistor scaling. This mismatch, as pointed out by Agarwal [3], is known as "Moore's gap" (Fig. (1-2)). This gap can be largely attributed to the bottlenecks associated with electrical interconnects.

### 1.1.1 Scaling limits for electrical interconnects

Moving forward, the bottleneck for bandwidth and clock speed performance for microprocessors will arise due to the fundamental limitations of copper based electrical interconnects. The Shannon-Hartley limit [4] determines the ultimate channel capac-

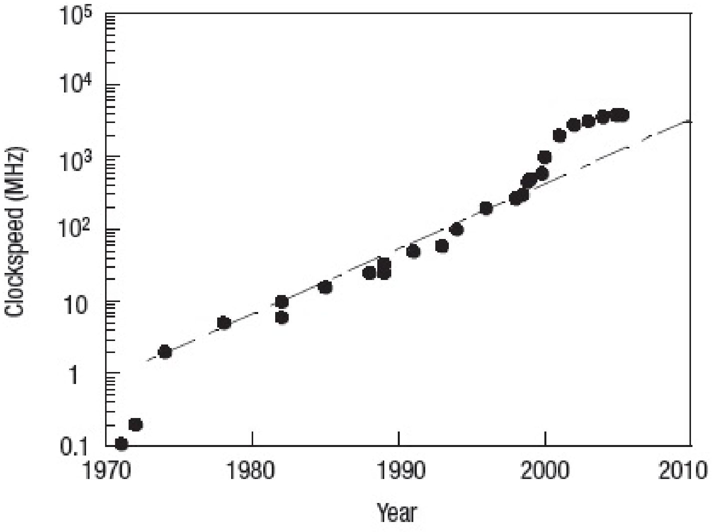

Figure 1-1: Clock speeds of microprocessors over time follows Moore's law (reproduced from [2]).

ity ($C$ in bits-per-second) of an interconnect and is given by

$$C = B\log_2(1+\frac{S}{N}) \tag{1.1}$$

where $B$ is the bandwidth in Hertz, $S/N$ is the ratio of signal power, $S$, to noise power, $N$ and is a unitless quantity. The energy required to increase the capacity of a channel scales linearly with bandwidth. The Shannon-limit for electrical interconnects is around 100 GHz. However, the power consumption associated with copper interconnects increases drastically at high bandwidths due to frequency dependent losses: skin effect and tangent delta loss (Tan delta).

The skin effect occurs in a conductor at high frequencies, whereby current flows only near the surface of the conductor with an effective "skin depth". This reduces the associated cross-section of the copper thereby raising the electrical resistance ($R$) and $I^2R$ losses. The skin depth, $\delta$, increases with the resistivity ($\rho$) and decreases with the angular frequency ($\omega$) and the magnetic permeability ($\mu$) of the conductor (Eq. 1.2). The skin depth of copper reduces from 2.1 $\mu$m at 1 GHz to 0.65 $\mu$m at 10

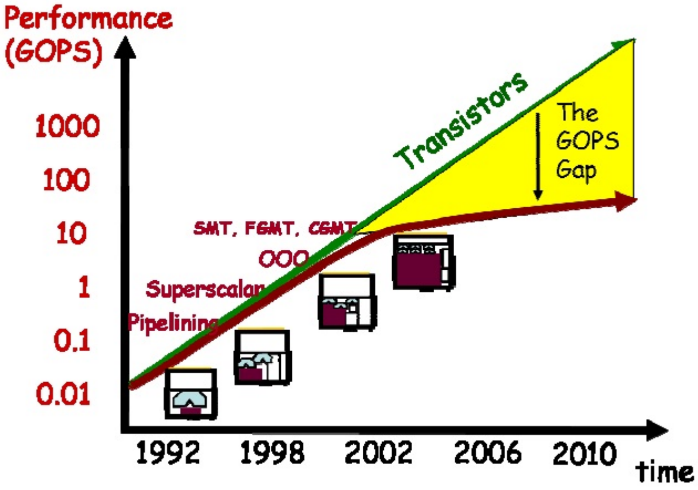

Figure 1-2: The "Moore's Gap" reflects the difference between the expected increase and the observed increase in the Giga operations per second (GOPS) performance of a microprocessor [3].

GHz and 0.21 $\mu$m at 100 GHz.

$$\delta = \sqrt{\frac{2\rho}{\omega\mu}} \tag{1.2}$$

The Tan delta losses are associated with the dielectrics surrounding the conductors and is proportional to the signal frequency. Doubling the frequency doubles the loss (loss = frequency×tan delta of the dielectric). Both the loss mechanisms bring the limit of copper interconnects further down from the Shannon-limit.

Finally, the resistive-capacitive (RC) delay associated with any electrical interconnect limits the maximum bandwidth that can be realized. With the Moore's law driving the need for low gate lengths for higher switching speeds, a bottleneck is reached due to the increasing propagation delay associated with the interconnects [5] between the transistors, resulting in "Moore's gap" (Fig. (1-3)). These limitations drive the need for optical technology that does not suffer from such drawbacks.

### 1.1.2 Optics to the rescue

Optical technology that uses photons as information carriers as opposed to electrons is a promising solution that overcomes "Moore's gap" at high bandwidths. Leverag-

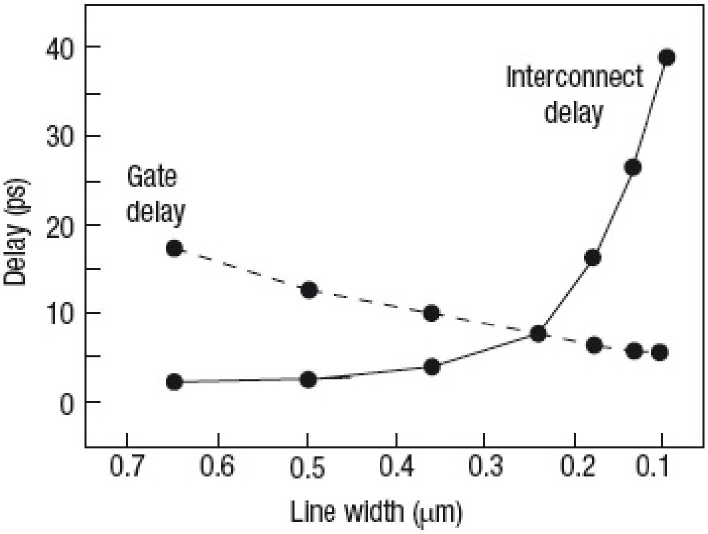

Figure 1-3: Trends in the gate delay and interconnect delay reflecting with IC fabrication technology reflecting the "interconnect bottleneck" (reproduced from [5]).

ing wavelength division multiplexing (WDM) for bandwidth multiplication has been realized in a well established optical fibre technology for long-haul communications. The Shannon limit for optical carriers is around 200 THz. The bandwidth-distance product has been used as a figure-of-merit (FoM) to evaluate the economic viability of a communication technology and optics has been proved to be a disruptive technology solution that was preferred when the FoM reached 10 Mb/s·km (Fig. (1-4)). Considering a similar situation at the board level where the interconnects lengths are of the order of 10-100 cm, there is a need for a transition to optics when the bandwidth requirements reach 10-100 Gb/s. Similarly, a transition to the optics is desired for the on-chip communication when the bandwidth requirements reach 1 Tb/s as the interconnect lengths are approximately 1 cm.

## 1.2 Electronic-photonic integrated circuits

With the internet traffic growing at a rate of 40% per year [6], the projected energy consumption by information technology has become an unsustainable fraction of the world electrical power generation under the current copper interconnect based technology. The challenges of energy consumption and communication bandwidth with

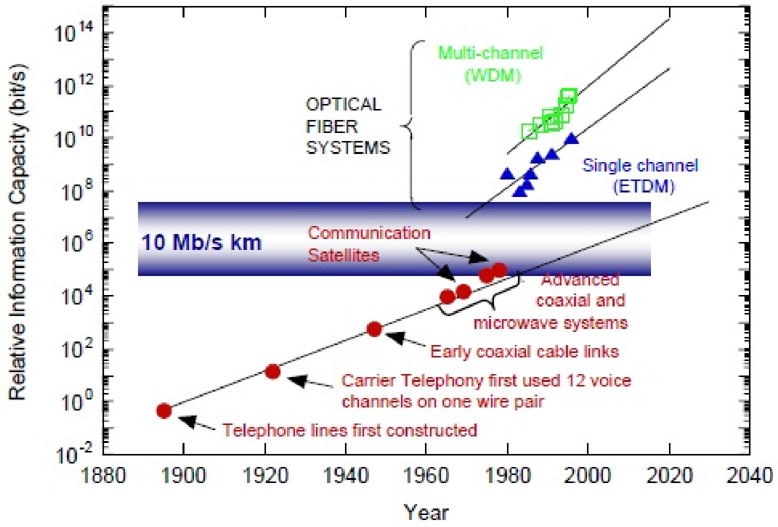

Figure 1-4: Communication capacity of a long-haul data link (copper or optical fibre) reveals the superiority of optical technology over time when the bandwidth-data product reached 10 Mb/s·km. (reproduced from [5]).

the copper interconnects call for a new scaling paradigm at the chip level. Power efficiency, the new driver of Moore's law, calls for dense electronic-photonic integration on a CMOS platform. Silicon microphotonics offers scalable solutions to the anticipated barriers of input/output (I/O) density, interconnection bandwidth and latency, and electronic/photonic partitioning through monolithic integration [7]. The new electronic-photonic platform that realizes the photonic functionality in CMOS, bridges the gap between CMOS architecture and fibre optic technology. The proposed architecture in this thesis uses electronics for computation and photonics for communication. Monolithic integration (Fig. (1-5)) on the existing CMOS platform proves to be power efficient (energy/bit) and more attractive than the electrical interconnects in the longer run. There are two possible scenarios (Fig. (1-5)) while considering the monolithic integration of active and passive photonic devices: 1. The current scheme of integration uses Front-End-Of-Line (FEOL) processes (high temperature CVD processes) that enable access to high quality single crystalline silicon and germanium for photonic applications; 2. In the future, Back-End-Of-Line (BEOL) integration involving polycrystalline and amorphous materials for passive and active optical components are desired owing to their design space flexibility and footprint advantages.

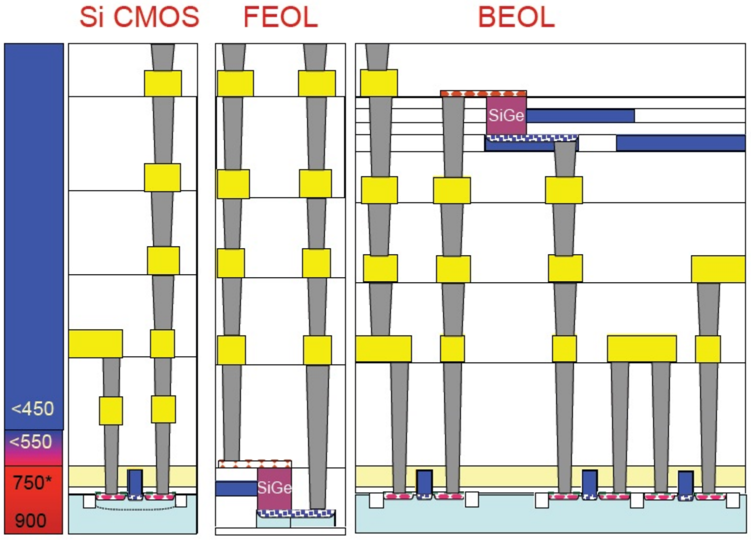

Figure 1-5: Various scenarios for monolithic integration of photonic devices in a silicon CMOS process: (a) Front-end-of-line (FEOL) process regime supports high temperature CVD processes, (b) Back-end-of-line (BEOL) photonic interconnect stack calls for a development of low temperature processes.

### 1.2.1 ATAC multicore processor architecture

Electronic-photonic integration at the chip level presents a new scalable approach in multicore architectures moving forward. As the computation is spread across multiple cores on a chip, the distribution of instructions and communication of intermediate values between cores account for a significant fraction of the execution time due to latency and contention for communication resources. Commercial multicore chips typically use a bus to interconnect cores that are not scalable for thousands of cores due to an increased bus wire length. Other solutions involving point-to-point mesh networks [8] mitigate the interconnect scalability issue by avoiding long global interconnects. However, the mesh network increases programming complexity by requiring locality in lines of code for point-to-point coordination. This requires multiple routing hops with a lot of overlapping messages that increase the latency. This thesis is influenced by an All-to-All Computing (ATAC) microprocessor architecture, proposed by G. Kurian et.al. [9], that scales easily to thousands of cores. ATAC is a tiled microprocessor architecture with an optical broadcast network that improves the bandwidth performance, the energy scalability and the ease of programmability of multicore processors. The proposed optical broadcast network relieves the need for locality in programming.

### Architecture overview

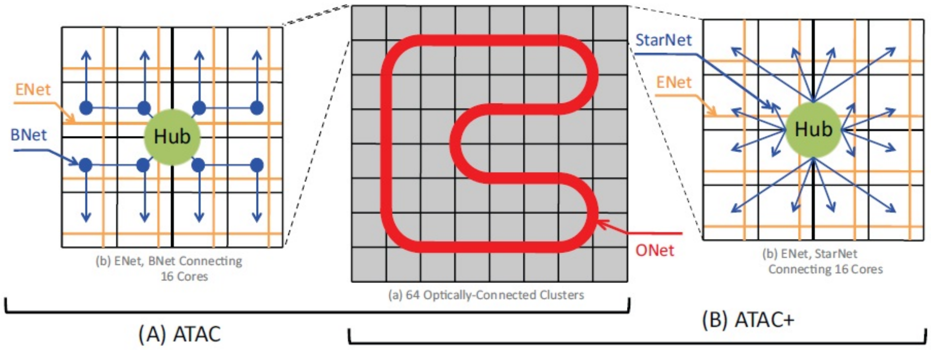

Figure 1-6: (A) ATAC architecture and (B) ATAC+ architecture (Reproduced from [10]).

ATAC considers a 1024 core architecture in which the cores are organized into 64 clusters with 16 cores each. Within each cluster, the cores communicate through a conventional short-range, point-to-point mesh network. An electrical networking architecture, *ENet*, is ideal for such predictable, short-range communication (Fig. (1-6)). A global optical interconnect (*ONet*) is added to the underlying 2D array of cores for energy-efficient, long-distance communication with low latency. Each cluster is connected to the *ONet* through a single *hub* that serves as the interface between the electrical and optical components (Fig. (1-6)). Communication from the core to the *hub* occurs through *ENet*. A similar electrical network, *BNet*, is used for data transfer from the *hub* to the cores. Since, *BNet* is dedicated for broadcast information, it does not require any routers, crossbars, or internal buffering. This thesis primarily focuses on the influence of the broadcast photonic network, *ONet*, on the microprocessor performance. Other details about the ATAC architecture are not relevant for this study and have been covered extensively elsewhere [9, 10].

### Optical communication through *ONet*

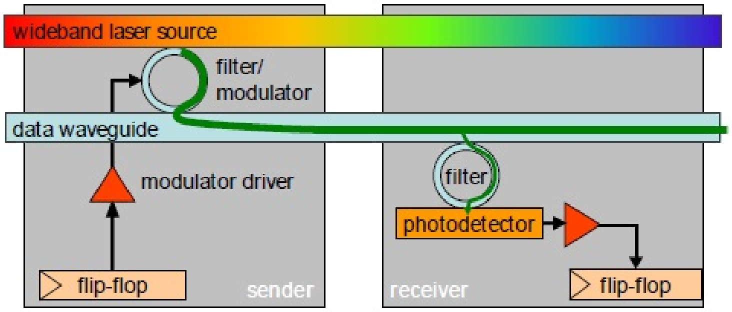

Figure 1-7: Optical communication in ATAC architecture (Reproduced from [9]).

*ONet* leverages wavelength division multiplexing (WDM) to achieve contention-free, low-latency global communication between clusters. Further, all the hubs are interconnected via optical waveguides to form a closed loop (Fig. (1-6)). Optical data transmission between 2 *hubs* in an ATAC architecture (Fig. (1-7)) typically requires the following components:

1. Optical power source: 1. Material: III-V (Hybrid integration) or Germanium (Monolithic integration) based laser 2. Wavelength of operation: Coarse WDM (CWDM), with wider channel spacings, uses 1310 nm as the center wavelength. Dense WDM (DWDM), on the other hand, uses 1550 nm as the center wavelength. ATAC requires 64 channels and the bandwidth of the broadband laser decides the channel spacing.

2. Optical bus: Si/a-Si/$Si_3N_4$ based waveguides as optical channels for data transfer. In ATAC, they serve to interconnect all the hubs.

3. Optical modulators: Si based ring/mach-zehnder modulators or Germanium based electro-absorption modulators: Optical switches for electrical-optical conversion of the data stream. It provides a way to imprint bit streams onto wavelengths. In ATAC, each hub has a modulator tuned to a unique wavelength to send information.

4. Optical filters: Si/a-Si based ring resonators/mach-zehnders: For mulitplexing (combining) and demultiplexing (filtering out) a set (4/8/16/32/64) of wavelegths. At the source end, the optical filter couples only a specific wavelength from the power supply waveguide to the data waveguide. At the receiver end, the optical filter extracts light from the data waveguide and couples it to the photodetector (Fig. (1-7)). In ATAC, each hub has 63 filters that allow it to receive signals from all the other hubs. Further, the filters are tuned to extract around 1/64th of the input signal, thereby allowing the remaining information to be transmitted to other hubs.

5. Photodetectors: Germanium: For optical to electrical conversion of the data stream. Every hub of the ATAC architecture has photodetectors corresponding to 63 wavelengths that their filters are tuned to receive.

### 1.2.2 ATAC+

ATAC+ is an improved version of ATAC (Fig. (1-6)) that addresses the issues of power gating of lasers, energy-inefficient operation of *BNet* during unicast transmission, and energy-inefficient inter-cluster unicast routing through *ONet* [10]. The ATAC+ architectural improvements are:

1. Adaptive SWMR (Single Writer Multiple Reader) optical link to address the static laser concerns.

2. Point-to-point StarNet (Fig. (1-6)) electrical network to address the inefficiency of BNet

3. Distance based unicast routing protocal

From the photonic design perspective, ATAC+ calls for 2 major improvements: (a) On-chip lasers for rapid power gating (ability to switch the laser on and off depending on the requirement) and (b) Athermal ring resonators. This thesis focuses on the design of athermal ring resonators and the motivation behind this study becomes clear if its implication on the final architecture is understood.

### Need for athermal silicon microphotonics

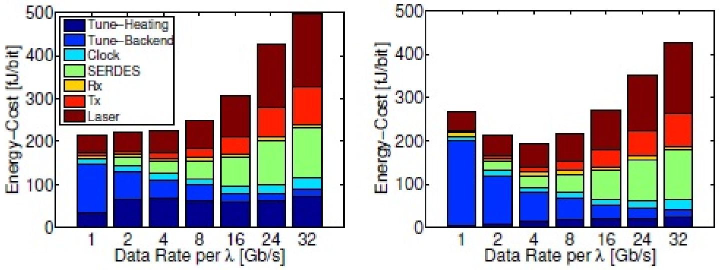

(a) 64 Gb/s (Min) (b) 256 Gb/s (Medium)

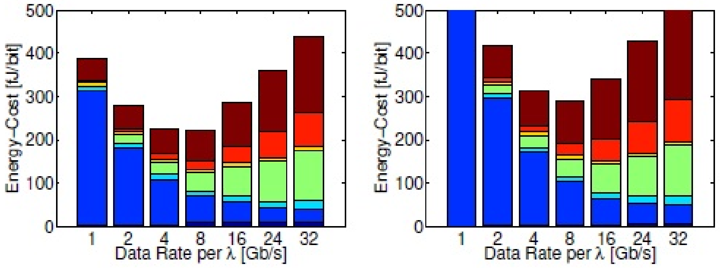

(c) 512 Gb/s (High) (d) 1024 Gb/s (Max)

Figure 1-8: In an ATAC environment, the ring tuning power dominates the energy consumption at low data rates (Reproduced from [11]).

Any temperature fluctuation arising from the on-chip electronics can alter the performance of silicon based photonic devices due to their high thermo-optic (TO) coefficient. This variation affects the filter response of silicon based ring resonators for WDM applications. Considering a Si based WDM architecture with 20 GHz channel spacing and typical temperature fluctuations between 25$^o$C-125$^o$C, the maximum allowable TO peak shift for a Si filter should be less than 1 pm/K, which is 2 orders of magnitude less than the experimentally observed TO shifts of silicon-on-insulator (SOI) filters. Active thermal compensation using thermo-electric coolers and heaters is power hungry and the number of I/O lines limits the integration density [12]. Further, in an ATAC environment, the thermal tuning energy constitutes a significant portion of non-data dependent (NDD) power [11] (Fig. (1-8)). For instance, at a data rate of 1 Gb/s per link, thermal tuning of back-end resonators constitutes 75% of the energy cost. ATAC+ considers four different architectural scenarios (Fig. (1-9(a))) and investigates the energy breakdown of all the processor components in each case.

The ideal energy efficiency (ATAC+(Ideal)) is achieved when low-loss optical waveguides, athermal rings and on-chip power gated lasers are employed (Fig. (1-9(b))). The normalized energy is around 50% more when the active tuning of rings is employed (ATAC+(RingTuned)). With Moore's law driving the need for higher energy efficient solutions, there is an increasing need for passive athermal design.

## 1.3 Thesis work

This thesis uses a polymer cladding to passively compensate the TO behavior of silicon based ring resonators for passive WDM filters. Chapters 2 and 3 introduces the governing electromagnetic wave theory of optical devices and the operating principle of ring resonators. Chapter 4 deals with the fabrication of ring resonators and the experimental characterization technique for the same. Chapter 5 discusses the passive athermal design principle and presents a working prototype of an athermal device. Chapter 6 focuses on the polymer material selection aspect of the athermal design and chapter 7 investigates the integration of the polymer clad devices in a CMOS multilayer architecture. Chapter 8 addresses the sensitivity of the devices to fabrication variations and presents an approach to overcome the same. Chapter 9 analyzes the system design of an optical add-drop filter and the advantages of an athermal design as a part of a WDM link. Chapter 10 summarizes the key findings and presents the future applications of athermal photonics.

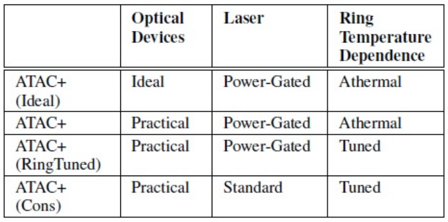

| | Optical Devices | Laser | Ring Temperature Dependence |
|---|---|---|---|
| ATAC+ (Ideal) | Ideal | Power-Gated | Athermal |
| ATAC+ | Practical | Power-Gated | Athermal |
| ATAC+ (RingTuned) | Practical | Power-Gated | Tuned |
| ATAC+ (Cons) | Practical | Standard | Tuned |

(a)

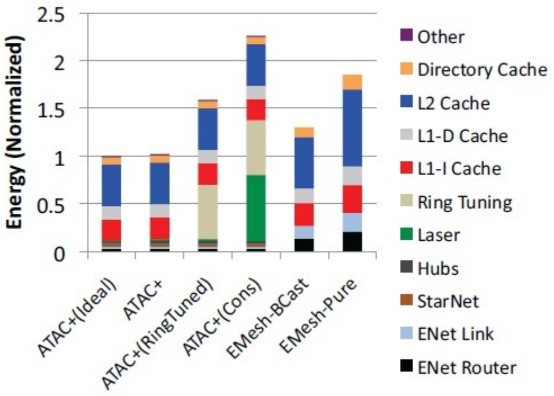

(b)

Figure 1-9: 1-9(a) Different possible scenarios of ATAC+ architecture (reproduced from [10]). 1-9(b) Energy consumption of various ATAC+ architectures normalized with respect to ATAC+(Ideal) (reproduced from [10]).

# Chapter 2

# Guided waves

The knowledge of electromagnetic wave propagation through a waveguide is necessary to understand the design and fabrication of an optical waveguide. This chapter explains the governing physics of light-matter interaction in a waveguide.

## 2.1 Maxwell's equations in a medium

The propagation of light in a medium satisfies Maxwell's equations:

$$\nabla \cdot \vec{D} = \rho \tag{2.1}$$

$$\nabla \cdot \vec{B} = 0 \tag{2.2}$$

$$\nabla \times \vec{E} = -\frac{\partial \vec{B}}{\partial t} \tag{2.3}$$

$$\nabla \times \vec{H} = \frac{\partial \vec{D}}{\partial t} + \vec{J} \tag{2.4}$$

where $\rho$ is the charge density, $\vec{J}$ is the current density, $\vec{E}$ is the electric field, $\vec{H}$ is the magnetic field, $\vec{D}$ is the electric flux density (electric displacement), $\vec{B}$ is the magnetic flux density and $t$ is the time. In optics, the medium under study is usually source free, i.e. $\rho = 0, \vec{J} = 0$. Further, the electrical and magnetic properties of a linear, isotropic, non-dispersive and homogenous medium are characterized by polarization density ($\vec{P}$) and magnetization density ($\vec{M}$), where $\vec{P} = \epsilon_o \chi_e \vec{E}$ and $\vec{M} = \mu_o \chi_m \vec{H}$. $\vec{D}$ and $\vec{B}$ can be expressed in terms of $\vec{E}$ and $\vec{H}$ for such a medium as follows:

$$\vec{D} = \epsilon_o \vec{E} + \vec{P} = \epsilon_o (1 + \chi_e) \vec{E} = \epsilon \vec{E} \tag{2.5}$$

$$\vec{B} = \mu_o \vec{H} + \vec{M} = \mu_o (1 + \chi_m) \vec{H} = \mu \vec{H} \tag{2.6}$$

where $\epsilon_o$ is the free space electric permittivity, $\chi_e$ is the electric susceptibility of the medium, $\mu_o$ is the free space magnetic permeability and $\chi_m$ is the magnetic suscpetibility of the medium. Using the vector identity, $\nabla \times (\nabla \times \vec{A} = \nabla(\nabla \cdot \vec{A} - \nabla^2 \vec{A}$, the above relations can be simplified to give the Helmhotlz wave equation for $\vec{E}$ as:

$$\nabla^2 \vec{E} - \mu\epsilon \frac{\partial^2 \vec{E}}{\partial t^2} = 0 \tag{2.7}$$

A similar relation can be written for $\vec{H}$.

The refractive index ($n$) of a medium can thus be defined as:

$$n = \sqrt{\frac{\epsilon\mu}{\epsilon_o \mu_o}} \tag{2.8}$$

For non-magnetic materials, where $\mu = \mu_o$, the expression for refractive index can be simplified as

$$n = \sqrt{\frac{\epsilon}{\epsilon_o}} = \sqrt{1 + \chi} \tag{2.9}$$

Physically, the refractive index is a measure of polarizability of a medium in the presence of electric and magnetic fields and is a function of wavelength/frequency ($n(\lambda)$). It reflects the speed of light (c) in a medium ($c = c_o/n$, $c_o$ is speed of light in vacuum).

## 2.2 Monochromatic electromagnetic waves

All components of the electric and magnetic fields of a monochromatic electromagnetic wave are harmonic functions of time with a given frequency $\nu$ and a corresponding angular frequency $\omega = 2\pi\nu$ such that, $\vec{E} = \vec{E}(\vec{r})\exp(i\omega t)$ and $\vec{H} = \vec{H}(\vec{r})\exp(i\omega t)$ ($\vec{r}$ is the position vector). Inserting the time harmonic relation in Eq.(2.7) gives

$$\nabla^2\vec{E} - \omega^2\mu\epsilon\vec{E} = 0 \tag{2.10}$$

A plane wave solution that satisfies Eq. (2.10) is obtained by defining $\vec{E}(\vec{r})$ and $\vec{H}(\vec{r})$ in terms of a propagation wavevector, $\vec{k}$.

$$\vec{E}(\vec{r}) = \vec{E_o}\exp(\pm i\vec{k}\cdot\vec{r}) \tag{2.11}$$

$$\vec{H}(\vec{r}) = \vec{H_o}\exp(\pm i\vec{k}\cdot\vec{r}) \tag{2.12}$$

where $\vec{H_o}$, $\vec{E_o}$ are constant vectors while $-$ and $+$ in the exponential terms reflect the forward and backward propagating wave solutions.

The magnitude of the wavevector $\vec{k}$ equals $2\pi/\lambda$ and a dispersion relation between $\vec{k}$ and $\omega$ can be arrived at using Eqs. (2.10) and (2.11).

$$k^2 = \omega^2\mu\epsilon \tag{2.13}$$

The magnitude of $\vec{k}$ in an optical medium is related to the free space propagation vector ($\vec{k_o}$) as $k = nk_o$ resulting in similar relations for the wavelength ($\lambda = \lambda_o/n$) and the speed ($c = c_o/n$). Further, for Maxwell's equations (Eq. (2.10)) to be satisfied, $\vec{E_o}$ and $\vec{H_o}$ should satisfy the following relations:

$$\vec{k}\times\vec{H_o} = -\omega\epsilon\vec{E_o} \tag{2.14}$$

$$\vec{k}\times\vec{E_o} = \omega\mu\vec{H_o} \tag{2.15}$$

It follows that $\vec{E_o}$, $\vec{H_o}$ and $\vec{k}$ are mutually orthogonal. Since $\vec{E_o}$ and $\vec{H_o}$ lie in a plane normal to the propagation vector $\vec{k}$, the wave is called a transverse electromagnetic (TEM) wave. The ratio between the amplitudes of $\vec{E_o}$ ($E_o$) and $\vec{H_o}$ ($H_o$) is called the impedance of the medium ($\eta$)

$$\eta = \frac{E_o}{H_o} = \sqrt{\frac{\mu}{\epsilon}} \tag{2.16}$$

Finally, the flow of the elctromagnetic power is given by a complex Poynting vector ($\vec{S} = \frac{1}{2}\vec{E} \times \vec{H}^*$) and is parallel to $\vec{k}$. It can be shown that the time averaged intensity, $I$, of the wave is:

$$I = \frac{|E_o|^2}{2\eta} \tag{2.17}$$

## 2.3 Phase and Group velocity

As pointed out earlier, the refractive index of a medium determines the phase velocity ($v_p$) of a plane wave in a given medium

$$v_p = \frac{\omega}{k} = \frac{c_o}{n} \tag{2.18}$$

However, for a dispersive medium, where the refractive index is a function of the frequency/wavelength ($n = n(\omega) = n(\lambda)$), the propagation velocity varies with the frequency of the light wave. So it is useful to define a group index $n_g = n - \lambda\frac{dn}{d\lambda}$, which determines the velocity of a "wave packet". The group velocity ($v_g$) reflects the rate of information travel / data transfer in a waveguide and can be shown to be:

$$v_g = \frac{d\omega}{dk} = \frac{c}{n - \lambda\frac{dn}{d\lambda}} = \frac{c}{n_g} \tag{2.19}$$

## 2.4 Polarization

The polarization of light at a given position is the time evolution of the electric-field vector, $\vec{E}(\vec{r}, t)$. For monochromatic light, the two orthogonal components of the complex amplitude vector, $\vec{E}(\vec{r})$, vary sinusoidally with time, such that the end-point of $\vec{E}(\vec{r})$ traces an ellipse. The plane waves where the wavefronts are given by parallel transverse planes (Fig. (2-1)) can be defined by a single polarization ellipse (elliptical polarization). Linear polarization and circular polarization are special cases of elliptical polarization where the ellipse degenerates into a line and a circle respectively. (4-1)).

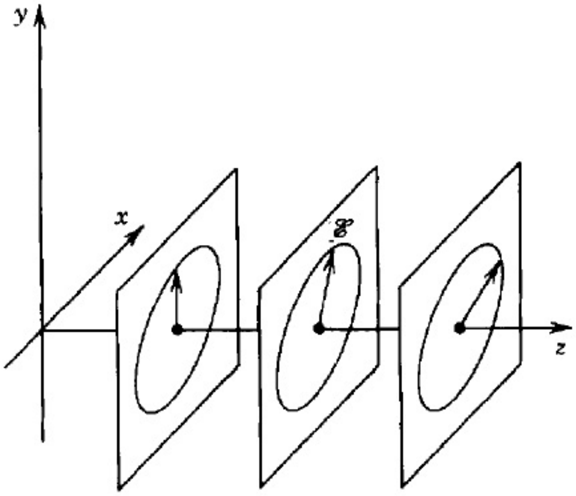

Figure 2-1: Polarization ellipse of a plane wave travelling in the z direction [13]

The *Poincaré* sphere [14] is a convenient geometrical representation of the polarization transformations through an optical device. Every point on the surface of the sphere (Fig. (2-2)) corresponds to a polarization state. The equator corresponds to linear polarization and the poles represent circular polarizations.

This thesis focuses on channel waveguides with rectangular cross-sections that do not support circular polarization. As a result, the study is restricted to linear polarizations with either horizontal electric field (transverse-electric, TE) or vertical electric field (transverse-magnetic, TM) states. With reference to a channel waveguide, the TE-mode refers to the polarization state where electric field is parallel to

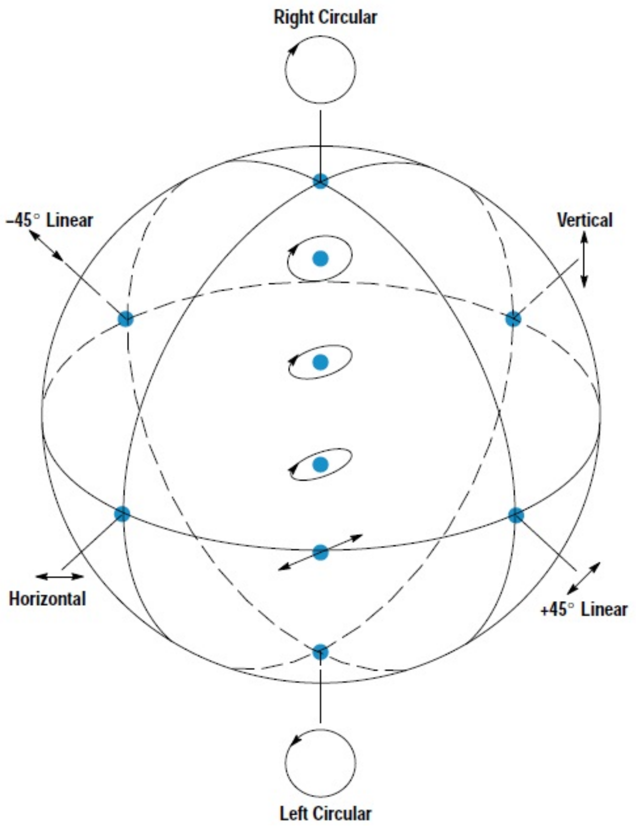

Figure 2-2: Any arbitrary polarization state can be represented as a point on the surface of the *Poincaré* sphere and a change in the polarization can be representated as a continuous path on the surface of the sphere [14].

the core/substrate interface, while TM-mode refers to the polarization state where electric field is perpendicular to the core/substrate interface. It is important to point out that the convention is a simplistic representation of modes in a channel waveguide as it cannot support a strictly (100%) TE or TM polarization, but instead supports a majority of one and balance of other (so TE mode in this thesis has about 95% TE component and 5% TM component).

## 2.5 Boundary conditions

The optical physics of waveguides requires a good understanding of the behavior of electromagnetic waves when it encounters a medium with a different refractive index. The reflection and transmission of the light waves at an interface between materials of differing refractive indices, is governed by the conservation of wave vectors and boundary conditions for E and H. D and B are conserved perpendicular to an interface between materials, 1 and 2:

$$\epsilon_1 E_{1\perp} = \epsilon_2 E_{2\perp} \qquad \mu_1 H_{1\perp} = \mu_2 H_{2\perp} \tag{2.20}$$

On the other hand, E and H are conserved parallel to the interface:

$$E_{1||} = E_{2||} \qquad H_{1||} = H_{2||} \tag{2.21}$$

Finally, the conservation of wave vectors can be used to derive Snell's law (Eq. (2.22)) that governs the light propogation from medium 1 (with index $n_1$) to medium 2 (with index $n_2$).

$$n_1 \sin(\theta_1) = n_2 \sin(\theta_2) \tag{2.22}$$

where $\theta_1$ and $\theta_2$ are angles between the interface normal and the propogation wave vectors in 1 and 2.

The total internal reflection occurs when $n_1 > n_2$ (Eq. (2.22)) resulting in waveguiding in higher index material. There exists a critical angle $\theta_c = \sin^{-1}(\frac{n_2}{n_1})$ beyond which all the light gets reflected inside the higher index material as can be derived from Eq. (2.22).

## 2.6 Dielectric waveguides

This thesis focuses on dielectric waveguides that have a higher index core surrounded by lower index cladding material. Light is guided inside the higher index core region by total internal reflection and there are 4 common dielectric waveguide configurations:

1. Slab waveguide: A thin film of higher index core is sandwiched between two other cladding films of lower indices (Fig. (2-3)).

2. Channel/Strip waveguide: A strip of higher index core on top of a lower index

cladding (Fig. (2-4(a))).

3. Strip-loaded waveguide: Strip of higher index material placed on a slab of lower index material to provide lateral optical confinement in the lower index slab layer (Fig. (2-4(b))).
4. Rib/Ridge waveguide: High index contrast layer is partially etched to create two sidewall interfaces to provide lateral confinement (Fig. (2-4(c))).

This thesis focuses on channel waveguides (Fig. (2-4(a))) for all the fabrication and measurements. Unlike metallic waveguides, the boundary conditions for dielectric waveguides do not restrict the light inside the core; hence a fraction of power is evanescently guided in the cladding region as well. This is better understood by studying the wave propagation in the simplest dielectric geometry : Slab waveguides.

### 2.6.1 Slab waveguides

The slab configuration corresponds to a waveguiding structure where the light is confined only in 1 direction. Light propagation inside a waveguide is conveniently described using the concept of "waveguide modes". A waveguide mode at a given wavelength is the stable shape with which the wave propagates. The mode shape is a function of wavelength and is completely determined by the waveguide cross-section and the refractive index profile of the waveguide.

Consider a symmetric slab cross-section (thickness: 2d) where the index of the top and bottom cladding are same ($n_{cl}$) for a given core index ($n_c$) (Fig.(2-3)). The waveguide modes can be solved starting from the wave equation for a non-uniform refractive index:

$$(\nabla^2 - \frac{1}{n^2 c_o^2}\frac{\partial^2}{\partial t^2})\vec{E} = 0 \tag{2.23}$$

Assuming TE mode of propagation where the E-field is parallel to the substrate, only the y component of the E-field exists and the solutions can be written as:

$$E_y = U(x)\exp(-i(\beta z - \omega t)) \tag{2.24}$$

Then the Helmholtz equation gives the solutions for the various eigenmodes of the waveguides whose eigenvalues define the corresponding propagation constants, $\beta_m$.

$$[\frac{d^2}{dx^2} + k^2 - \beta^2]U(x) = 0 \tag{2.25}$$

where $U(x)$ is the optical mode profile (complex amplitude), $k^2 = k_o^2 n^2$ is the cross-sectional index profile, $\beta = n_{eff} k_o$ is the propagation contant and the waveguide mode is defined by the E-field along the z direction (propagation direction), $E(x, z) = U(x)\exp(i\beta z)$.

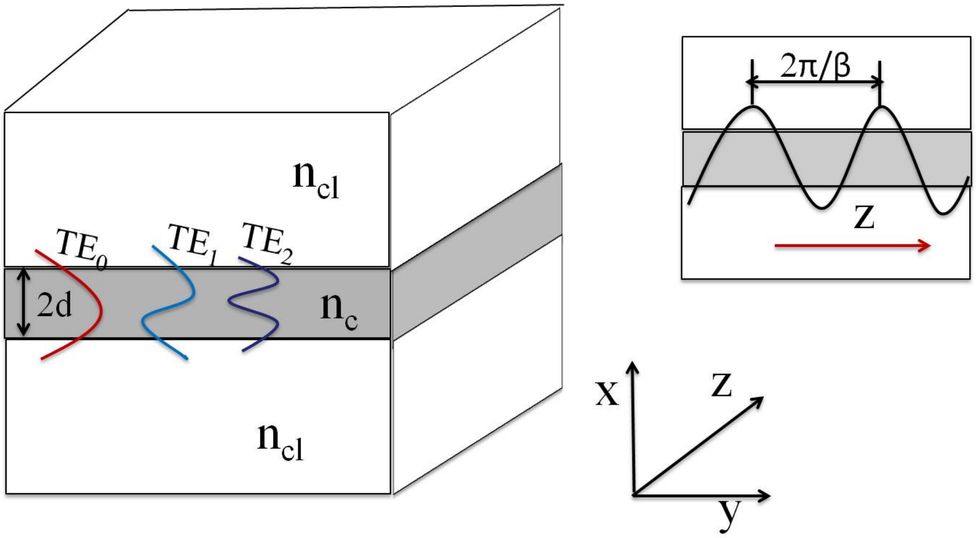

Figure 2-3: Cross-section of a slab waveguide showing the first 3 TE modes.

All possible TE mode solutions can be derived from Eq.(2.25) after invoking the boundary conditions at the core/cladding interfaces. Electric field distribution of the m$^{th}$ TE mode ($TE_m$) is given by Eq. (2.26) and exhibit behavior similar to "standing waves" (Fig. (2-3)).

$$\vec{E}_m(x, z) = U_m(x)\exp(i\beta_m z) \tag{2.26}$$

where $\beta_m$ corresponds to propagation constant of the $TE_m$ mode. Higher order modes have smaller $\beta$ and larger number of nodes ($U = 0$) (Fig. (2-3)). A larger waveguide dimension and higher index contrast can support a larger number of modes. A similar set of solutions can be derived for TM mode of propagation which has $E_x$ and $H_y$

components of EM wave.

The speed of propagation of the mode depends on its effective index ($n_{eff}$) and is given by $c/n_{eff}$, where $n_{eff} = \beta/k_o = \frac{\beta\lambda_o}{2\pi}$. Thus $n_{eff}$ varies depending on the order of the mode and decreases as the order of the mode increases. In other words, higher order modes propagate faster than lower order modes inside a waveguide. Furthermore, it can be shown that the effective index of any mode should lie between the refractive index of the core and the cladding, i.e. $n_{cl} < n_{eff} < n_c$. This is because the $n_{eff}$ of a given mode is just a weighted average of the index of the core and the cladding where the power distribution in each region acts as the weighting factor. The weighting factor can be related to the confinement factor ($\Gamma_{core}$) of the core, which is the fraction of optical power in the core to the total propagation power.

### 2.6.2 2D confined waveguides

The aforementioned analysis for slab geometry waveguides can be extended to waveguides that confine light in 2 directions. The popular 2D confined waveguide geometries are: Channel, Strip-loaded and Rib/Ridge cross-sections (Fig. (2-4)). The region guiding the majority of the mode is the difference between the 3 2D confined geometries. While, most of the light resides in the rectangular cross-section for the channel waveguide, the slab (grey shade) of a lower index (compared to core but higher compared to the lower cladding) is light guiding region for strip-loaded geometry. Rib/Ridge waveguide on the other hand is similar to strip loaded waveguide but both the slab and the rectangular cross-sections have the same refractive index.

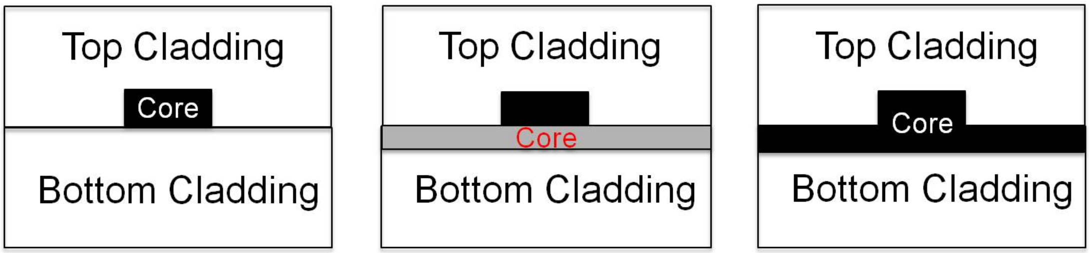

(a) Channel waveguide (b) Strip-loaded waveguide (c) Ridge waveguide

Figure 2-4: Various 2D confined planar waveguide geometries

### 2.6.3 Effective index method

As mentioned before, the analysis for slab waveguides can be extended to solve for effective indices for other waveguide geometries (Fig. (2-4)). The effective index method is an approach which deconvolutes the waveguide structures to various slab structures (Figs. (2-5),(2-6)). Mathematically, it is equivalent to the separation of variables approach to solve the 2D Helmholtz equation for $U(x, y)$ where $U(x, y) \approx U'(x)U"(y)$.

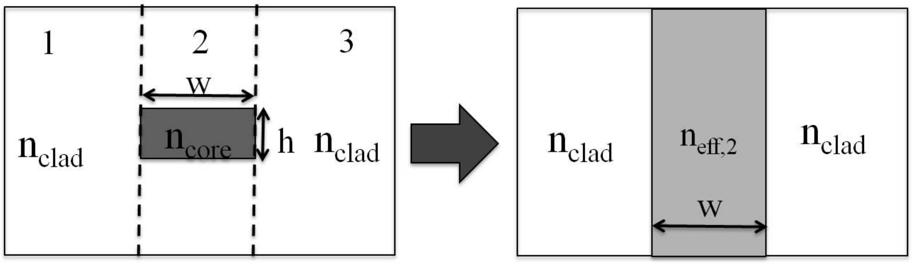

Figure 2-5: Effective index method to solve for modes of a channel waveguide.

Thus, the modes for channel waveguides can be solved by treating region 2 in Fig. (2-5) as a slab waveguide with a thickness of "h". Region 2 can then be treated as a core with an index of $n_{eff,2}$. The modes of the channel waveguide can then be arrived at by solving the new slab waveguide structure with thickness "w" and index $n_{eff,2}$ (Fig. (2-5)). This method is reasonably accurate only when $w >> h$ for the channel waveguide.

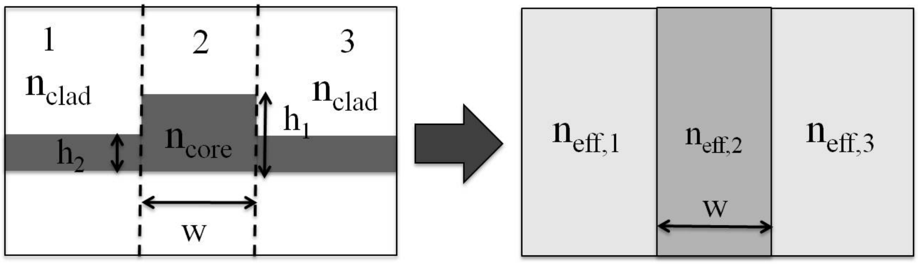

Figure 2-6: Effective index method to solve for modes of a ridge waveguide.

A similar method can be used for ridge waveguides that can be divided into 3 different slab regions with thicknesses "$h_1$" and "$h_2$" respectively. Regions 1 and 3 form the new cladding regions with an index of $n_{eff,1} = n_{eff,3}$ and region 2 forms the core (index=$n_{eff,2}$) for the new slab structure with thickness "$w$" (Fig. (2-6)).

The effective index method works well for low-index contrast waveguide, but is inaccurate for high-index-contrast, single mode, channel waveguides that are more relevant for integration applications. Hence, electromagnetic simulation softwares that employ different numerical techniques (finite element method, finite different time domain technique, film mode matching) are used for such applications. Commercial software packages like RSoft's FemSIM, Photon Design's FIMMWAVE and Apollo Photonic suite are widely used for mode calculations of photonic structures with arbitrary index distribution. This thesis uses FIMMWAVE [15] for mode calculations and design of a-Si waveguides with polymer top cladding.

### 2.6.4 Mode solving using FIMMWAVE

FIMMWAVE is a program developed by Photon Design for modelling various 2D and 3D waveguide structures. It provides the following mode solving techniques to choose from: Film-mode matching (FMM) solver, Finite difference method (FDM) solver and Finite element method (FEM) solver. Due to its speed and accuracy compared to the other numerical techniques, the FMM technique has been used in this thesis and will be the primary solver for all the FIMMWAVE simulations reported in this thesis.

#### FMM solver

The FMM solver is a semi-analytical, fully vectorial waveguide solver based on the film mode matching method as described by Subdo [16–18]. In this method, a waveguide cross-section is considered as a sandwich of thin slices numbered $m = 1, 2, 3...M$. Each slice is further considered as a combination of various film layers numbered $n = 1, 2, 3..N$. Thus layers and slices are perpendicular to each other (Fig .(2-7)). The FMM method involves finding TE and TM modes of each sliced cross-section (scalar modes in case of weak waveguiding) and collecting all the modes with the same propagation vector,$k_z$. The field amplitudes are then adjusted at each slice interface to match the field distribution (to obey Maxwell's law). Only certain values of $k_z$ gives non-zero mode amplitudes with matching field distributions at the slice interfaces. Each such value of $k_z$ corresponds to a mode solution of the mode. Detailed derivations of the corresponding numerical method are presented elsewhere [16–18] and are not covered in this section.

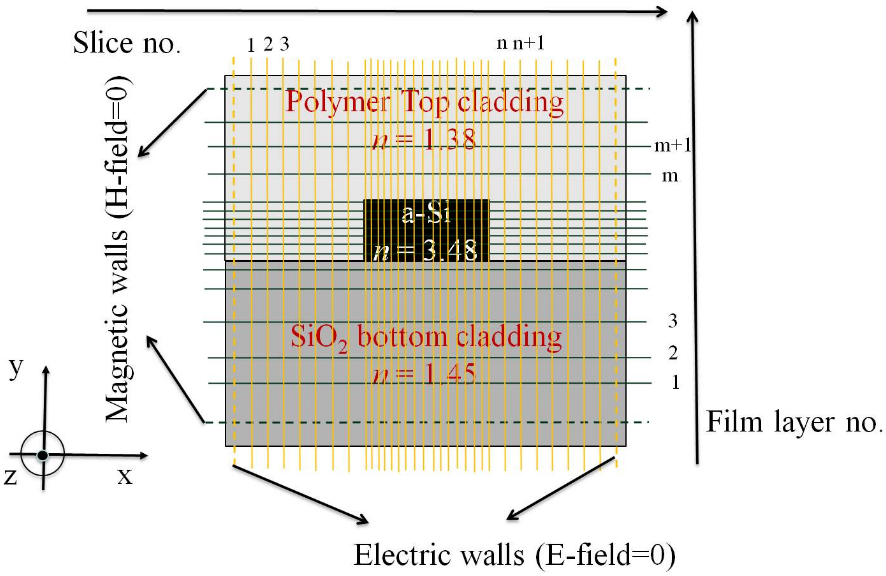

Figure 2-7: The FMM algorithm breaks down a dielectric cross-section into slices and layers. Example is shown for an a-Si core waveguide with a polymer over-cladding and $SiO_2$ under-cladding.

The FMM solver of the FIMMWAVE thus creates the mentioned number (user controlled) of 1D modes (higher number corresponds to greated accuracy) of each sliced cross-section. The user controls the size of the cross-section and smaller the cross-section (greater number of slices), greater will be the accuracy. Once the 1D modes are created, the FMM solver algorithm of FIMMWAVE arrives at the mode solutions through the following stages:

1. Generating matrices of overlap integrals between the 1D modes of the $n^{th}$ slice and the 1D modes of the $(n+1)^{th}$ slice.

2. Finding a set of coefficients of the 1D modes that will give field profile obeying Maxwell's equation. Given the boundary conditions at the left hand side (lhs)

and a guess propagation constant ($\beta$), a solution can be "propagated" from the lhs to rhs using the overlap matrices. Values of $\beta$ are scanned over a range of values until the boundary conditions are met at rhs.

An amorphous Si (a-Si, $n$ : 3.48)) waveguide with 600 nm × 200 nm (width× height) cross-section with a polymer top cladding ($n$ : 1.38) and SiO$_2$ under-cladding ($n$ : 1.45) supports 3 modes at $\lambda = 1550$ nm. This includes the fundamental TE mode ($n_{eff} = 2.49$), the fundamental TM mode ($n_{eff} = 1.66$) and the first order TE mode ($n_{eff} = 1.59$) in decreasing order of $n_{eff}$ (Figs. (2-8,2-9,2-10)).

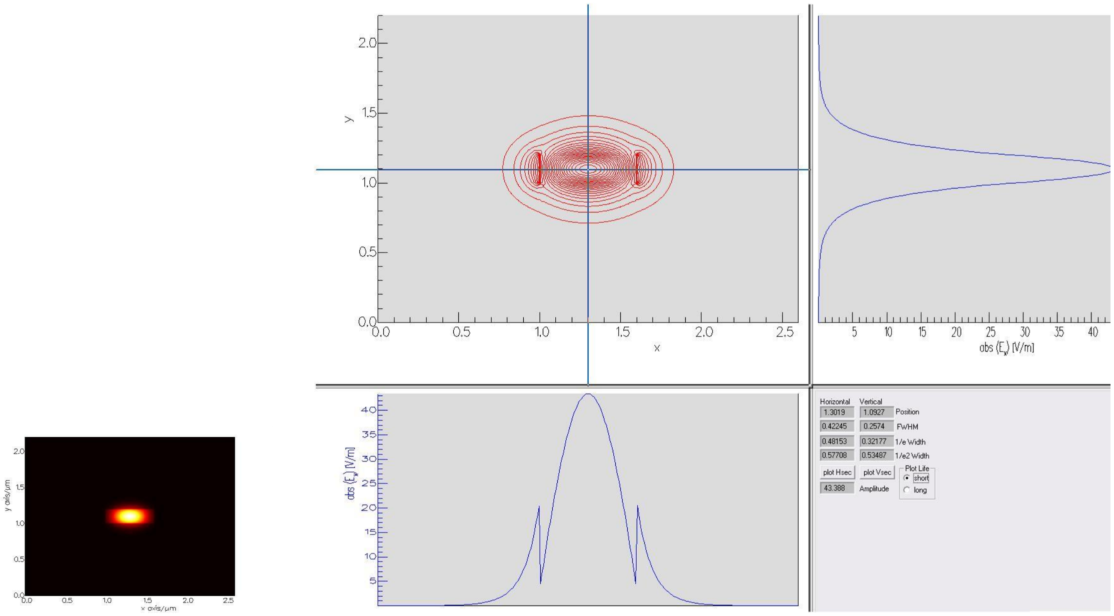

| Horizontal | Vertical | |
|---|---|---|
| 1.3019 | 1.0927 | Position |
| 0.42245 | 0.2574 | FWHM |
| 0.48153 | 0.32177 | 1/e Width |
| 0.57708 | 0.53487 | 1/e2 Width |

43.388 Amplitude

(a) (b)

Figure 2-8: 2-8(a) The intensity of fundamental TE mode for a 600 nm × 200 nm a-Si core waveguide, with the polymer over-cladding and the SiO$_2$ bottom cladding (Fig. (2-7)) 2-8(b) The absolute value of the $x$ component of the electric field distribution in the mode (abs($E_x$))

As mentioned in section 2.4, while the TE mode has $E_x$ as the major component of electric field, the TM mode has $E_y$ as the major E-field component. So, the discontinuity for $E_x$ is seen across the core sidewalls for the fundamental TE mode (Fig. (2-8(b))). On the other hand, the discontinuity of $E_y$ occurs for the TM mode across the core/cladding film interface (Fig. (2-9(b))).

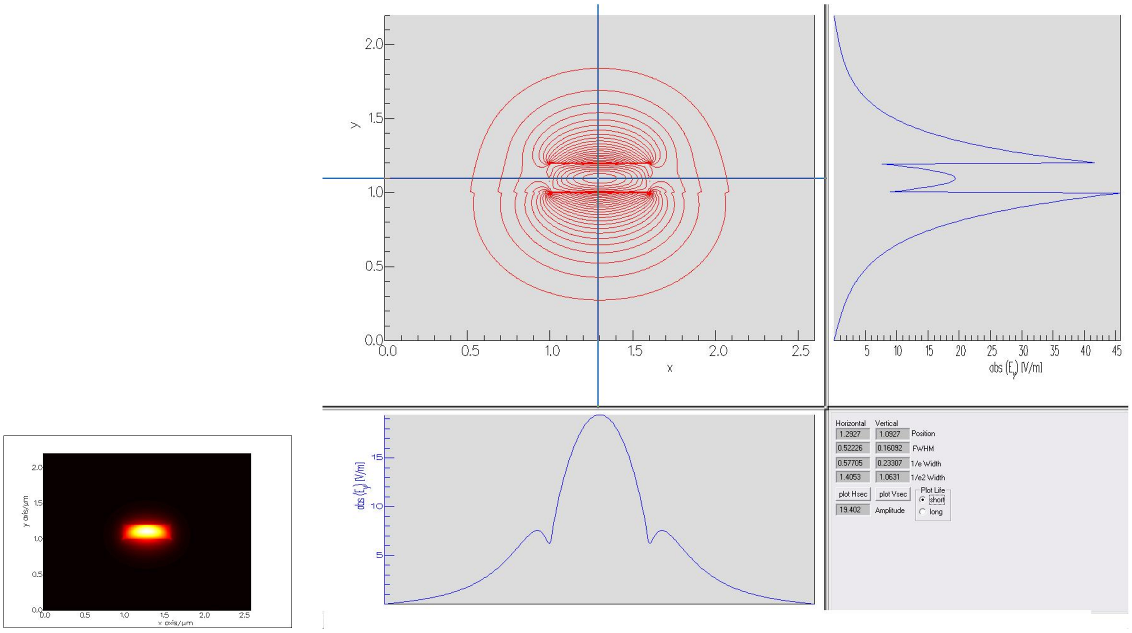

| Horizontal | Vertical | |
|---|---|---|
| 1.2927 | 1.0927 | Position |
| 0.52226 | 0.16092 | FWHM |
| 0.57705 | 0.23307 | 1/e Width |
| 1.4053 | 1.0631 | 1/e2 Width |
| 19.402 | | Amplitude |

Plot Life: ● short ○ long

(a) (b)

Figure 2-9: 2-9(a) The intensity of fundamental TM mode for a 600 nm × 200 nm a-Si core waveguide, with the polymer over-cladding and the $SiO_2$ bottom cladding (Fig. (2-7)) 2-9(b) The absolute value of the $y$ component of the electric field distribution in the mode (abs($E_y$))

Further, higher order modes correspond to E-field nodes ($E_x = 0$ for TE or $E_y = 0$ for TM) within the core (Fig. (2-10)).

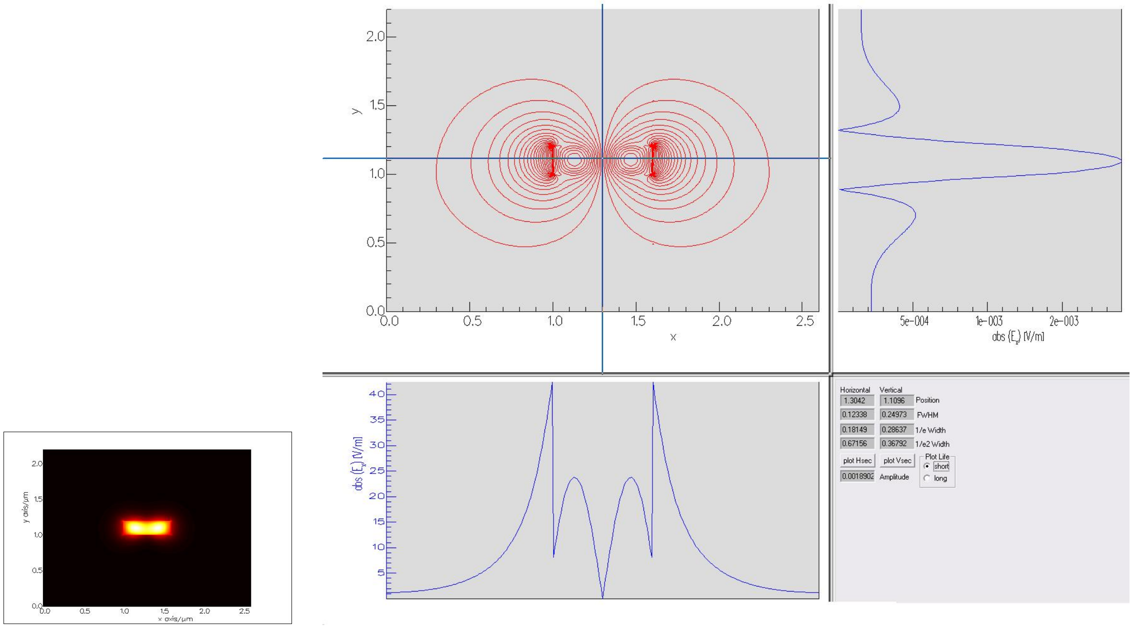

| Horizontal | Vertical | |
|---|---|---|
| 1.3042 | 1.1096 | Position |
| 0.12338 | 0.24973 | FWHM |
| 0.18149 | 0.28637 | 1/e Width |
| 0.67156 | 0.36792 | 1/e2 Width |
| 0.0018902 | | Amplitude |

(a) (b)

Figure 2-10: 2-10(a) The intensity of 1st order TE mode for a 600 nm × 200 nm a-Si core waveguide, with the polymer over-cladding and the $SiO_2$ bottom cladding (Fig. (2-7)) 2-10(b) The absolute value of the $x$ component of the electric field distribution in the mode (abs($E_x$))

## 2.7 Slot waveguides

Boundary conditions are responsible for the difference between the behavior of TE and TM modes. The discontinuity of the electric field at the core/cladding interface has been leveraged to confine light in a low index region for slot waveguides (Fig. (2-11)). Slot geometry [19–22] is of wide interest when there is a need for light emission, modulation or plasmonic waveguiding in low-index materials.

Slot waveguides consist of atleast one narrow lower-index region sandwiched between two higher-index regions (Fig. (2-11(a))). The refractive index discontinuity at the sidewall results in a discontinuity in the transverse E-field at the sidewall interface due to the governing boundary conditions (Eq. 2.20). The E-field outside the

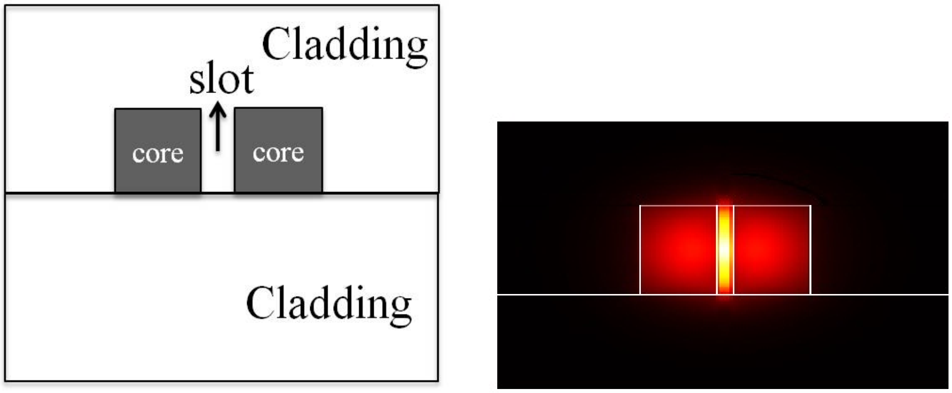

(a)

(b)

Figure 2-11: 2-11(a) Cross-section of a slot waveguide. 2-11(b) TE mode of a slot waveguide showing light confinement in the low-index cladding region

high-index region decays exponentially (evanescent tail). As two high-index regions move closer than the decay length of the evanscent tail, the optical field is strongly enhanced, resulting in high confinement in the lower-index region (Fig. (2-11(b))). The interaction between the evanescent tails of 2 higher-index regions is also responsible for coupling between two waveguides that is discussed in the next section.

## 2.8 Coupled waveguide systems

When 2 waveguides are close to each other such that their fields overlap, light can be guided in both waveguides and the effective index of such a coupled system is different from that of the individual waveguides. When light is launched only in one waveguide, it eventually gets transferred to the second waveguide in the coupled system before getting coupled back to the first waveguide. The power transfer between the 2 waveguides occurs through an evanescent tail which extends outside the core. An analogy can be drawn with “quantum tunneling” occuring between the 2 closely placed quantum wells (Fig. (2-12)).

In case of weak coupling, the “coupling mode theory” can be invoked, where the modes for the coupled waveguide system can be considered as a superposition of the modes of the individual waveguides. Considering the fundamental mode for both the waveguides, symmetric and anti-symmetric mode solutions (Fig. (2-12)) with

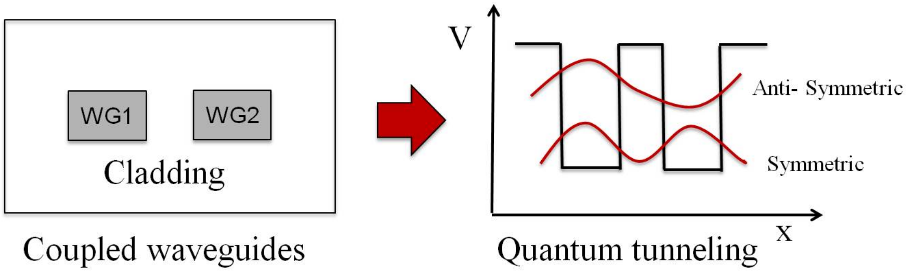

Figure 2-12: Coupled waveguides can be treated in a similar manner to the “quantum tunneling” effect while solving for modes of the entire system

different effective indices can be derived. If fundamental modes of equal amplitudes ($U_1 = U_2$) with same $n_{eff}$ are launched in both the waveguides, the coupled mode can be written as $(U_1+U_2)\cdot\exp[ikz\cdot(n_{eff}+\beta)]+(U_1-U_2)\cdot\exp[ikz\cdot(n_{eff}-\beta)]$, where $\beta$ is the coupling coefficient between the waveguides. When power is launched in only one waveguide, it gets transferred to the second waveguide over a characteristic “beat” length as the symmetric and anti-symmetric modes have different speeds (effective index). The beating length equals $\pi k/\beta$, and depends on the coupling coefficient $\beta$. $\beta$ depends on the separation between the two waveguides and can be calculated from the difference in the effective indices of even and odd modes. Alternatively, a perturbation theory method for weakly coupled waveguides can be used to calculate $\beta$ [23]. The interaction between the waveguides is very crucial for the operation of ring resonators that is covered in detail in the next chapter.

# Chapter 3

# Ring Resonators

Ring resonators serve as building blocks of very-large-scale-integrated (VLSI) photonic circuits [24]. They can be used for various applications in a photonic circuit including optical add/drop filters (OADF) for wavelength division multiplexing/demultiplexing (WDM) [25–27], phase-shifters for polarization conversion [28], optical cavity for wavelength tunable lasers [29–32], ultra-fast electro-optic modulation for optical switching [33, 34] and frequency comb generation in a mode-locked laser [35–37].

## 3.1 Operation principle

An optical waveguide in a closed loop structure constitutes a ring resonator. The shape of the closed loop can be a circle, ellipse or a racetrack. Any light circulating in such a ring builds up in intensity when the optical path length ($n_{eff} \times L$) equals an integral multiple of wavelength ($m\lambda_r$) as given by the resonance condition in Eq. (3.1).

$$n_{eff}L = m\lambda_r, \ \textit{where m is an integer and } \lambda_r \textit{ is the resonance wavelength} \tag{3.1}$$

The ring resonator still needs an external source of light to be coupled into the device. This is usually realized by evanescent light coupling from a “bus” (as it can carry multiple wavelengths) waveguide that is located close to the ring (Fig. (3-1)). Two popular configurations of the ring resonator device structure exist. The first is an all-pass configuration which corresponds to light/power transfer between a ring and one bus waveguide (Fig. (3-1(a)). The all-pass configuration is preferred for modulators, phase shifters, lasers and amplifiers. The "add-drop" configuration is the second preferred device structure that involves a ring coupled to two bus waveguides. The add-drop configuration is more suited for filtering applications in WDM where there is a need for routing a specific channel wavelength to the desired location.

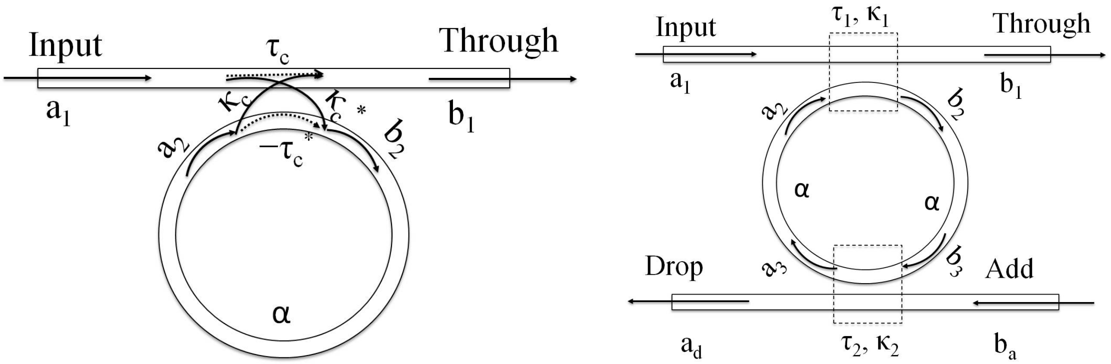

(a) (b)

Figure 3-1: 3-1(a) All-pass configuration corresponds to power transfer between a ring and one waveguide. 3-1(b) Add-drop configuration corresponds to power transfer between a ring and two waveguides.

### 3.1.1 All-pass configuration

It is useful to understand the operation of an all-pass filter before analyzing the add-drop configuration. The all-pass configuration takes advantage of the loss (or gain) of the resonator to manipulate the amplitude and phase of the bus waveguide output. Consider a light travelling along the bus with an amplitude "$a_1$". When it approaches the ring, part of the light evanescently couples to the ring while the remaining goes through the bus. The final transmitted amplitude "$b_1$" depends on the amount of light coupled to and from the ring, the transmission loss inside the ring and the phase difference associated with the coupling event. The coupling event associated with the device can be studied using a scattering matrix ($\mathbf{S}$=$s_{ij}$) that relates the input fields ($\mathbf{a} = [a_1, a_2]^t$) to output fields ($\mathbf{b} = [b_1, b_2]^t$) as follows

$$\mathbf{b} = \mathbf{S}\mathbf{a} \tag{3.2}$$

$\mathbf{S}$ can be shown to be symmetric with the form [38] shown in Eq. (3.3) after invoking power conservation and time-reversal.

$$\mathbf{S} = \begin{bmatrix} \tau_c & \kappa_c \\ -\kappa_c^* & \tau_c^* \end{bmatrix} \tag{3.3}$$

where $\tau_c$ and $\kappa_c$ are complex through-coupling and cross-coupling coefficients of the complex mode amplitudes defined by $\mathbf{b}$ and $\mathbf{a}$ (Fig. (3-1(a))). The complex nature of $\tau_c$ and $\kappa_c$ arises from the fact that every coupling event is associated with a phase change of the electric fields. More precisely, a phase shift of $\pi/2$ accompanies every coupling event as a result of crossing from low index material to high index material. Hence, the condition, $\tau_c = \tau$ where $\tau \in \mathbb{R}$ (where $\mathbb{R}$ is the set of real numbers), can be imposed without any loss of generality. Further, $\kappa \in \mathbb{R}$ can be defined such that $\kappa_c = \pm j\kappa$ to account for the phase change associated with the coupling equation. Then Eq. (3.3) can be rewritten as

$$\mathbf{S} = \begin{bmatrix} \tau & -j\kappa \\ -j\kappa & \tau \end{bmatrix} \tag{3.4}$$

where $\tau^2 + \kappa^2 = 1$ for lossless coupling. A relation between $a_2$ and $b_2$ can be derived after defining $\alpha$ as the amplitude transmission loss around the ring, $L$ as the circumference of the ring and $n_{eff}$ as the effective index of the waveguide:

$$a_2 = b_2 \exp(-\alpha L) \exp(j\frac{2\pi n_{eff} L}{\lambda}) \tag{3.5}$$

For simplicity, the input wave amplitude $a_1$ can be set to 1 and other field amplitudes can be normalized with respect to it. An equation relating $b_1$ to $\tau, \alpha, L, \lambda$ and $n_{eff}$

(Eq. (3.6) can be derived using the aforementioned lossless coupling condition and Eqs. (3.2),(3.4) and (3.5).

$$b_1 = \frac{\tau - \exp(-\alpha L)\exp(j\frac{2\pi n_{eff} L}{\lambda})}{1 - \tau\exp(-\alpha L)\exp(j\frac{2\pi n_{eff} L}{\lambda})} \tag{3.6}$$

At the resonance condition, given by Eq. (3.1), the above equation can be further simplified and the linear power ($|b_1|^2$) transmitted at the throughport can be written as

$$|b_1|^2 = \left|\frac{\tau - \exp(-\alpha L)}{1 - \tau\exp(-\alpha L)}\right|^2 \tag{3.7}$$

It is evident that the transmission through the bus waveguide equals zero (Eq. (3.7)) when the through-transmission coupling coefficient equals the round trip transmission loss inside the ring. Physically, it can be understood by realizing that a phase change of $\pi/2$ accompanying every coupling event results in a total phase change of $\pi$ when the light is coupled from the ring back to the bus waveguide. Thus, the orignal light travelling from the input port and the light coupled from the ring interfere destructively at the through port due to the phase difference of $\pi$ between them. Hence, it is possible to completely transfer all the power from the bus waveguide to the ring at resonance if the coupling coefficients are designed carefully by choosing the appropriate coupling gap and coupling length. Three coupling regimes can be identified based on the relative magnitudes of $\tau$ and $A = \exp(-\alpha L)$ (Note that high round-trip loss of the ring results in high damping rate and low $A$):

1. Under-coupled regime ($1/\tau < 1/A$): Under-coupling refers to a condition where the coupling rate ($\propto 1/\tau$) between the ring and the bus is less than the damping rate ($\propto 1/A$) inside the ring. In this case, the amplitude of the field coupled from the ring to the bus is less than the field amplitude coming from the input port. The transmitted field in the through-port is in phase ($b_1 : +ve$) with the light from the input-port but reduced by the power amplitude of the light coupled from the ring. Such a condition occurs when the transmission loss inside the resonator is too high which could be due to a small bending radius or

a large sidewall roughness. Alternatively, it can also result due to a large gap between the bus and the ring that has a low cross-coupling coefficient ($\kappa$). The ultimate limit of this condition occurs when there is an infinite loss in the ring or an infinite gap between the bus and the ring and is equivalent to the absence of the ring (similar to off-resonance behavior).

2. Critically coupled regime ($1/\tau = 1/A$): Critical coupling occurs when the coupling rate between the ring and the bus is equal to the damping rate inside the ring. In this case, the amplitude of the field coupled from the ring is equal to the amplitude of the input field resulting in perfect destructive interference in the transmitted field at the through-port. The transmitted power at the through-port is zero (Eq. (3.7)) suggesting a complete power transfer from the bus to the ring and a high extinction ratio (resonance depth). Changing the loss behavior of the ring can shift the device away from the critical condition resulting in a smaller extinction ration. Such a device can, thus, function as a "notch filter" where the extinction ratio of the device can be tuned by changing the round-trip loss of the ring. However, designing for critical coupling requires pre-existing knowledge of the losses inside the ring and a careful selection of the gap between the ring and the bus. So, any variation due to fabrication tolerance can move the behavior away from critical coupling.

3. Over-coupled regime ($1/\tau > 1/A$): Over-coupling results when the coupling rate ($\propto 1/\tau$) between the ring and the bus is more than the damping rate ($\propto 1/A$) inside the ring. So, the amplitude of the field coupled from the ring to the bus is more than the input field amplitude. Hence, the transmitted field at the through-port is out-of-phase ($b_1 : -ve$) with the incoming field and has a power given by the the difference between the coupled field power from the ring and the input field power. This occurs in a design where there is small gap between the ring and bus resulting in a large cross-coupling coefficient ($\kappa$). Alternatively, it can also result in cases where the transmission loss in the ring is very small due to improved processing techniques. A limiting case of the

> over-coupled regime occurs when the loss inside the ring approaches zero. In this case, $b_1$ approaches -1 at resonance, indicating a phase shift of $\pi$ of the incoming wave with no change in the amplitude. This behavior of the all-pass configuration is leveraged for its application as a “phase shifter/phase filter”.

Transmission of an all-pass filter will reveal “dips” corresponding to the ring’s resonances (Fig. (3-2(a))) and the extinction ratio (resonance depth) varies depending on the coupling regime (Fig. (3-2(b))).

### 3.1.2 Add-drop configuration

The above analysis can be extended for an add-drop configuration (Fig. (3-1(b))) by accounting for coupling between ring and 2 waveguides. Considering, $a_1 = 1$ and $b_a = 0$, the expression for transmission, $b_1$ (Eq. (3.8), at the through-port remains similar with the coupling loss component ($\tau_2$) accounted for in the round-trip loss of the ring.

$$b_1 = \frac{\tau_1 - \tau_2 \exp(-\alpha L) \exp(j \frac{2\pi n_{eff} L}{\lambda})}{1 - \tau_1 \tau_2 \exp(-\alpha L) \exp(j \frac{2\pi n_{eff} L}{\lambda})} \tag{3.8}$$

Further, it can be shown that the amplitude of light at the drop port ($a_d$) can be varied based on the coupling coefficients at the input side ($\tau_1, \kappa_1$) and the drop side ($\tau_1, \kappa_1$) of the ring (Eq. 3.9).

$$a_d = \frac{-\kappa_1 \kappa_2 \exp(-\frac{\alpha L}{2}) \exp(j \frac{\pi n_{eff} L}{\lambda})}{1 - \tau_1 \tau_2 \exp(-\alpha L) \exp(j \frac{2\pi n_{eff} L}{\lambda})} \tag{3.9}$$

At resonance,a complete transfer of power from the input to the drop port occurs in case of a symmetric lossless coupling ($\kappa_1 = \kappa_2$), provided the round-trip loss of the ring is negligible, i.e. $A = \exp(-\alpha L) \approx 1$ (Fig. (3-3)).

The above analysis is independent of the nature of coupling region. So, the results for both all-pass and add-drop configurations hold true for lateral and vertical couplings between the bus and the ring (Fig. (3-4)).

## 3.2 Figures of merit of a resonator

1. Quality factor (Q factor): The Q factor of a resonator is a measure of the photon lifetime ($\tau_{ph}$) inside the cavity and reflects the spectral width (sharpness) of the resonant peaks. Mathematically, it can be expressed as the ratio of maximum energy inside the cavity and dissipated energy per cycle. For a given resonant (angular) frequency, $\omega_r = 2\pi c/\lambda_r$, and characterstic lifetime of the resonator ($\tau_{ph} = 1/c\alpha$), the expression for the Q factor can be written as:

   $$Q\ factor = \omega_r \tau_{ph} \approx \frac{\lambda_r}{\Delta\lambda_{FWHM}} \tag{3.10}$$

   where $\Delta\lambda_{FWHM}$ is the spectral full width at half maximum (FWHM) of the resonance. The photon lifetime inside the cavity is determined by the instrinsic optical loss ($\alpha_{in}$) inside the cavity which could be a combination of material absorption, sidewall scattering, bending and substrate leakage. Higher the loss, greater is the damping rate ($\propto 1/\tau_{ph}$) and smaller will be the $\tau_{ph}$. The intrinsic Q factor can be written in terms of $\alpha_{in}$ and group index ($n_g$) as:

   $$Q_{in} = \frac{2\pi n_g}{\alpha_{in}\lambda_r} where\ n_g = n_{eff} - \lambda_r \frac{\partial n_{eff}}{\partial \lambda} \tag{3.11}$$

   However, the coupling loss ($\alpha_{coupling}$) from the bus to the ring acts as an extra source of damping that affects the total Q factor ($Q_{tot}$) of the device. The $Q_{tot}$ depends on the intrinsic cavity Q factor ($Q_{in}$) and the extrinsic Q factor associated with the coupling loss ($Q_{ex}$) (Eq. 3.12).

   $$\frac{1}{Q_{tot}} = \frac{1}{Q_{in}} + \frac{1}{Q_{ex}} \tag{3.12}$$

   An expression for $Q_{tot}$ can derived from Eqs. 3.11 and 3.12

   $$Q_{tot} = \frac{2\pi n_g}{(\alpha_{in} + \alpha_{coupling})\lambda_r} \tag{3.13}$$

Rings with high Q factor (around $10^5 - 10^7$) are ideal candidates for sensing applications due to their sharp peak response. For DWDM applications, the Q factor limits the minimum spacing between 2 channels. For a 20 GHz ($\approx 0.8nm$) channel spacing WDM architecture, the minimum desired Q is around 2000. On the other hand, for modulation applications, it is desirable to have a small photon lifetime (low Q $\approx$ 100) for fast switching capabilities.

2. Free spectral range (FSR): FSR is the spacing between two consecutive resonant peaks of a resonator and is a function of $\lambda_r$, circumference of the resonator ($L$) and $n_g$ (Eq. 3.14). For WDM applications, the FSR limits the channel count performance of the architecture. It is desirable to squeeze all the channels within 1 FSR of a ring so that a given ring does not filter more than one wavelength. Small rings have a large FSR (Eq. 3.14) and are desirable for high bandwidth applications involving 32/64 channels. However, the bending radius of such rings are limited by the bending loss that increases with decreasing radius. The associated Q factor of the ring limits the channel spacing and the channel count.

$$FSR = \frac{\lambda_r^2}{n_g L} \tag{3.14}$$

3. Resonant field enhancement factor of the cavity ($G$): Field enhancement in the resonant cavity is predominantly determined by the cavity finesse ($F$) which in turn depends on the losses inside the ring. Finesse can be expressed as the ratio of the FSR and the spectral FWHM (Eq. 3.15).

$$F = \frac{FSR}{\Delta\lambda_{FWHM}} = \frac{2\pi}{\alpha L} \tag{3.15}$$

If $I_o$ is the input energy flux from the bus, $T$ is the power transmission coefficient at the coupling region and $I$ is the circulating energy flux inside the resonator, the resonant field enhancement factor ($G$) can be shown to be:

$$G = \frac{I}{I_o} = \frac{1-T}{\alpha L} = \frac{2\pi}{F}(1-T) \tag{3.16}$$

Rings with high $G$ are preferred for non-linear applications like frequency comb generation, electro-optic modulators where there is a need for high power buildup inside the cavity.

## 3.3 Simulation of ring resonators: FDTD solutions by LUMERICAL

Designing ring resonators involves optimizing the gap between the bus and the ring for critical coupling. This thesis uses the 3D FDTD simulations package offered by LUMERICAL [39] to understand the transmission properties of add and drop channels as the gaps between the bus waveguides and the ring are changed.

The software uses finite-difference-time-domain (FDTD) technique for solving Maxwell's equations in a complex geometry. The frequency solutions can be arrived through Fourier transforms of the time domain solutions. FDTD solutions starts from the time dependent form of Maxwell's equations (Section 2.1). For instance, the Maxwell's equation of a TM mode propagation ($H_x$, $H_y$ and $E_z$ are the independent components) in the z direction can be reduced to:

$$\frac{\partial D_z}{\partial t} = \frac{\partial H_y}{\partial x} - \frac{\partial H_x}{\partial y} \tag{3.17}$$

$$D_z(\omega) = \epsilon_o \epsilon_r(\omega) E_z(\omega) \tag{3.18}$$

$$\frac{\partial H_x}{\partial t} = -\frac{1}{\mu_o}\frac{\partial E_z}{\partial y} \tag{3.19}$$

$$\frac{\partial H_y}{\partial t} = \frac{1}{\mu_o}\frac{\partial E_z}{\partial x} \tag{3.20}$$

where all the symbols represent the same properties described in Section 2.1. Electromagnetic fields can then be solved as a function of time from the above equations.

The solver uses a simulation mesh, similar to FIMMWAVE (Fig. (2-7)), and solves for field solutions at every mesh point. FDTD solutions adopts a non-uniform mesh size, where the mesh dimensions are smaller inside the high index material and larger in the low index material, to maintain a constant number of mesh points per wavelength (as it scales as $\lambda/n$). Consequently, the smaller mesh results in a longer simulation time and larger memory requirements. The FDTD simulation of a silicon add-drop filter with a polymer over-cladding and a $SiO_2$ under-cladding requires defining the material properties and geometry in all the 3 dimensions (Fig. (3-5)). Then an appropriate mode is chosen for launching in the add waveguide (mode source) and the transmission at the drop waveguide can be read out by the power monitor placed appropriately. Gaps between the ring and the waveguides can then be optimized to maximize the drop transmission. The power output in the drop transmission is shown to be $-ve$ because the propagation is in the $-x$ direction (Fig. (3-6)).

## 3.4 Higher-order filters

The order of a ring filter is described by its response away from resonance. The intensity at the drop response (Eq. 3.9) of a single ring in an add-drop configuration (Fig. (3-1(b))) exhibits a Lorentzian behavior near resonance. Higher-order filters, on the other hand exhibit a different roll-off behavior compared to the single-ring configuration. A single-ring has a roll-off of 20 dB/decade, and is referred to as a first-order filter because the drop-port amplitude evolves as $1/i\omega$. First-order filters are not sufficiently discriminating for applications in dense wavelength division multiplexing (DWDM). Higher-order filters [40–43], on the other hand, have a sharper roll-off, flatter passbands and higher out-of-band signal rejection. An analogy can be drawn from an LC electronic filter circuit, where rings can be treated as a reactive element. Cascading the reactive elements in a serial (Fig. (3-7(a))) or parallel (Fig. (3-7(b))) fashion, can result in steeper filter response away from the resonance.

The scattering matrix analysis explained in Section (3.1.1) can be extended for the analysis of higher order filters [44] after accounting for the coupling between indvidual rings in addition to the coupling to the buses. In the serially coupled $3^{rd}$ order filter (Fig. (3-7(a))), the resonators are coupled directly to each other. On the other hand, parallel cascaded system (Fig. (3-7(b))) consists of a bus mediated coupling between the rings. In the latter case, the filter response depends on the length of the bus waveguide between the rings.

Mathematically, the response ($H(s)$) of the filters can be written as [45]

$$H(s) = \frac{P_1(s)}{P_2(s)} \tag{3.21}$$

where $P_1(s)$ and $P_2(s)$ are polynomials in $s$, and the filter response is evaluated near the resonant frequency ($\omega_o$) such that $sT << 1$, where $s = i(\omega - \omega_o)$ and $T$ is the round trip time and equals $Ln_{eff}/c$. For instance, the drop port response (Eq. (3.9)) of a first-order filter derived in section 3.1.2, can easily rewritten as:

$$a_d = \frac{-\kappa_1\kappa_2 \exp(-\frac{\alpha L}{2})(1+s)}{(1-\tau_1\tau_2\exp(-\alpha L)) - s\tau_1\tau_2\exp(-\alpha L)} \tag{3.22}$$

The zeros of $P_1$ are called zeros of the filter, while zeros of $P_2$ are called the poles of the filter. Assuming, $P_1$ and $P_2$ do not have common zeros, the order of the filter is determined by the order of $P_2$. For a first-order filter, $P_2$ is also first order and has the form of $(s - p)$ as seen in Eq. (3.22). Similarly, for an $n^{th}$-order filter, $P_2$ has a form given by $\prod_n (s_n - p_n)^n$, where the poles $p_n$ can be degenerate. The asymptotic behavior given by $s^{-n}$ of an $n^{th}$-order filter is responsible for its sharper roll-off compared to a $1^{st}$ order filter. Further, a flatter top band is achieved due to multiple interference effects between multiple filters in a higher-order filter. Also, it is possible to increase the FSR of a higher-order filter compared to a single filter by choosing the radius of individual rings carefully.

In this thesis, we primarily focus on the behavior of first-order, all-pass a-Si ring resonators and the next chapter explains the associated fabrication and transmission measurement techniques.

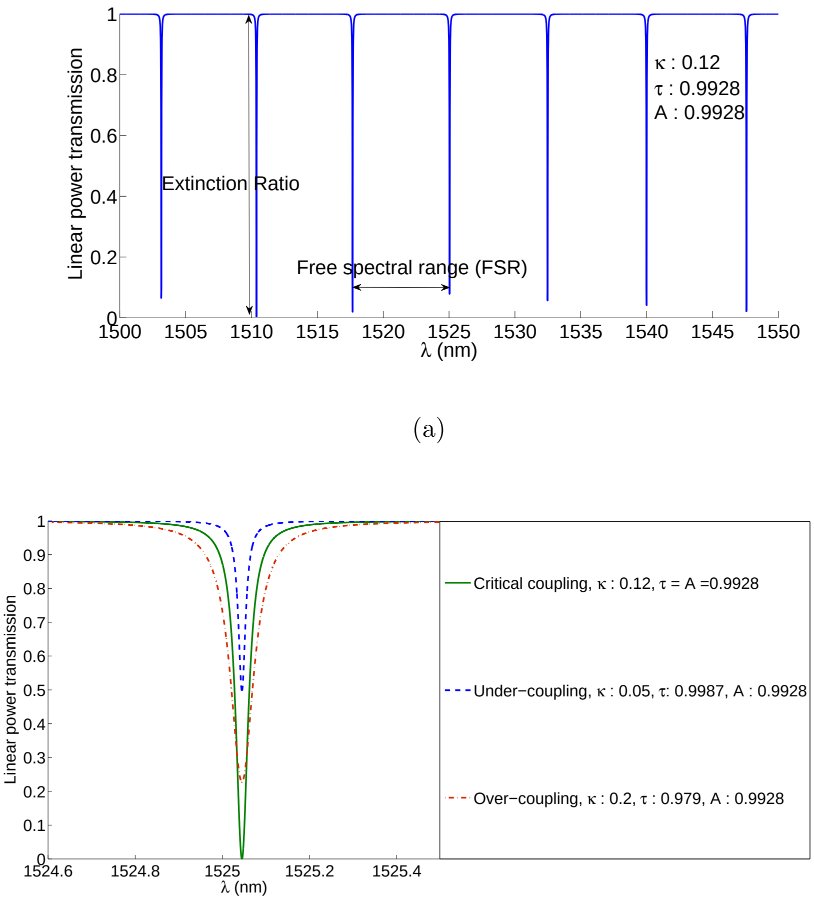

(a)

(b)

Figure 3-2: 3-2(a) Simulated transmission spectrum of a ring with 20 $\mu$m radius ($n_{eff} = 2.5$) in an all-pass configuration. The through-coupling ($\tau = 0.9928$) and cross-coupling coefficients ($\kappa = 0.12$) are chosen to critically couple the light, with $\lambda = 1525\ nm$, from the bus to the ring, which has a round trip loss of 5 dB/cm ($A = 0.9928$). 3-2(b) The variation of the power transmission at resonance depends on the coupling regime of operation. Zero power transmission occurs at critical coupling for a given ring loss.

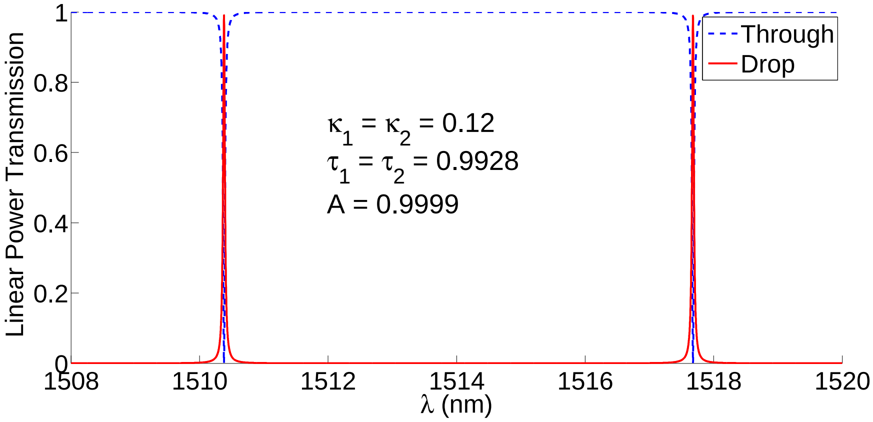

Figure 3-3: Simulated transmission spectrum of a 20 $\mu$m radius ring resonantor ($n_{eff} = 2.5$) in an add-drop configuration. There is symmetric coupling between the ring and both the waveguides ($\tau_1 = \tau_2 = 0.9928$, $\kappa_1 = \kappa_2 = 0.12$). The round trip loss is assumed to be around 0.05 dB/cm ($A = 0.9999$) to demonstrate the complete transfer of power from the input-port to the drop-port

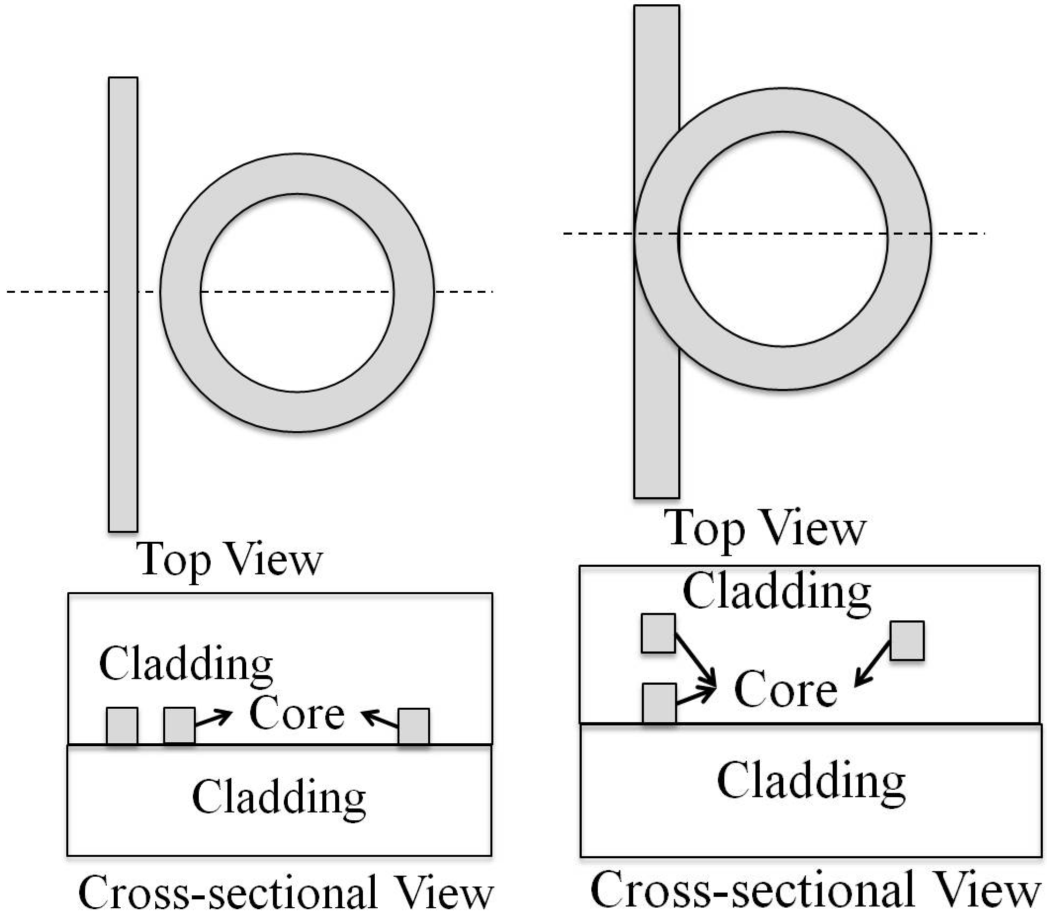

(a) (b)

Figure 3-4: 3-4(a) Schematic of a laterally coupled ring resonator 3-4(b) Schematic of a vertically coupled ring resonator.

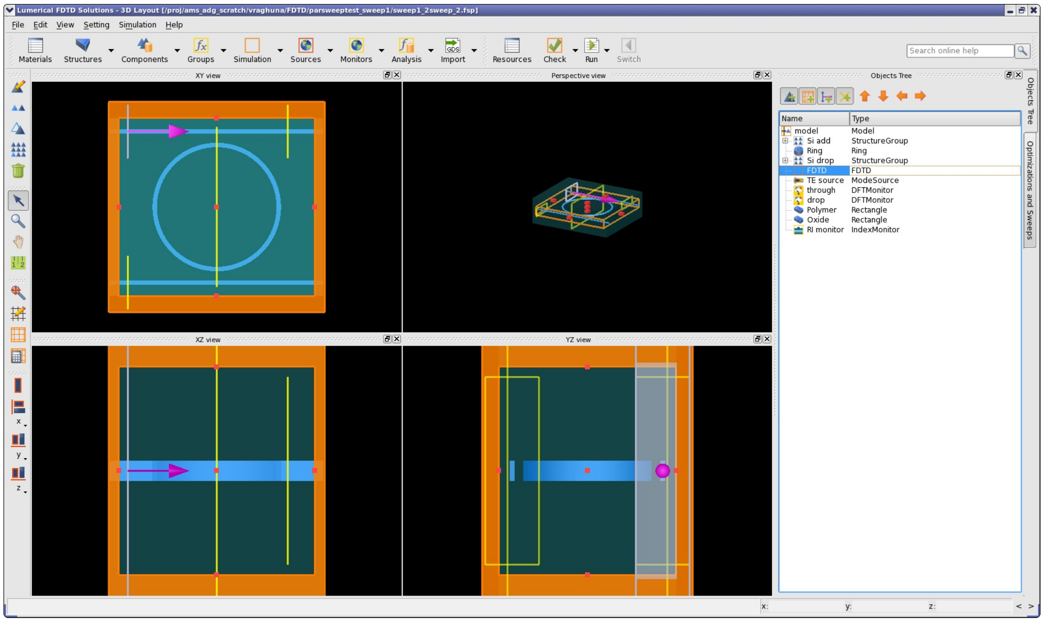

Lumerical FDTD Solutions - 3D Layout [/proj/ams_adg_scratch/vraghuna/FDTD/parsweeptest_sweep1/sweep1_2sweep_2.fsp]

| Name | Type |
|---|---|
| model | Model |
| Si add | StructureGroup |
| Ring | Ring |
| Si drop | StructureGroup |
| FDTD | FDTD |
| TE source | ModeSource |
| through | DFTMonitor |
| drop | DFTMonitor |
| Polymer | Rectangle |
| Oxide | Rectangle |
| RI monitor | IndexMonitor |

Figure 3-5: Layout of FDTD solutions package (purached from LUMERICAL) for simulating the transmission of Si based add-drop filter.

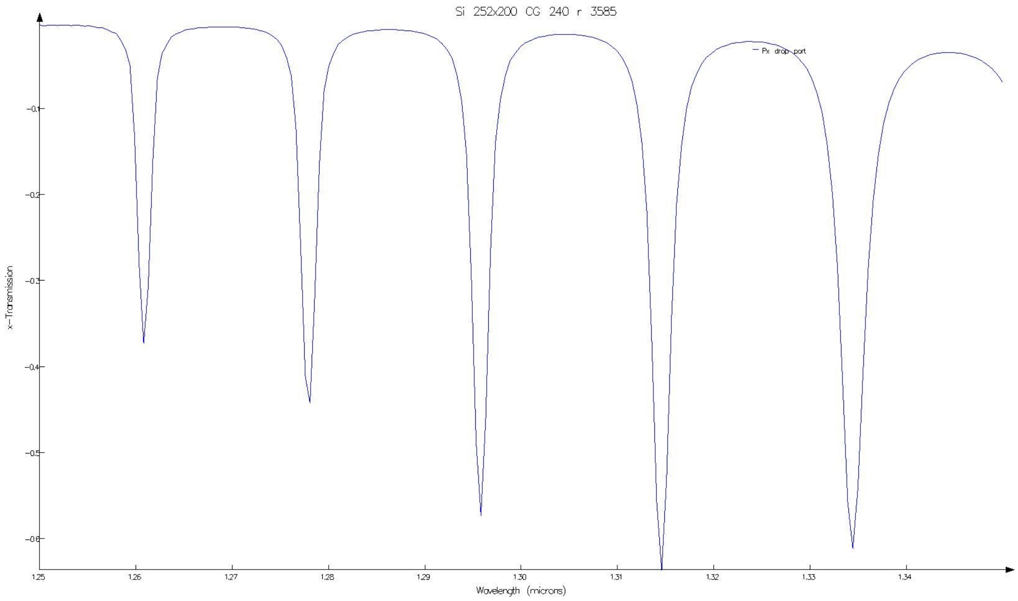

Figure 3-6: Lumerical simulation of the drop transmission of a Si waveguide (cross-section:252 nm × 220 nm, $n$ : 3.48) with a polymer over-cladding ($n$ : 1.38), and a $SiO_2$ under-cladding ($n$ : 1.45). The radius of the ring is 3.6 $\mu$m and the coupling gaps between the ring and the buses are 240 nm.

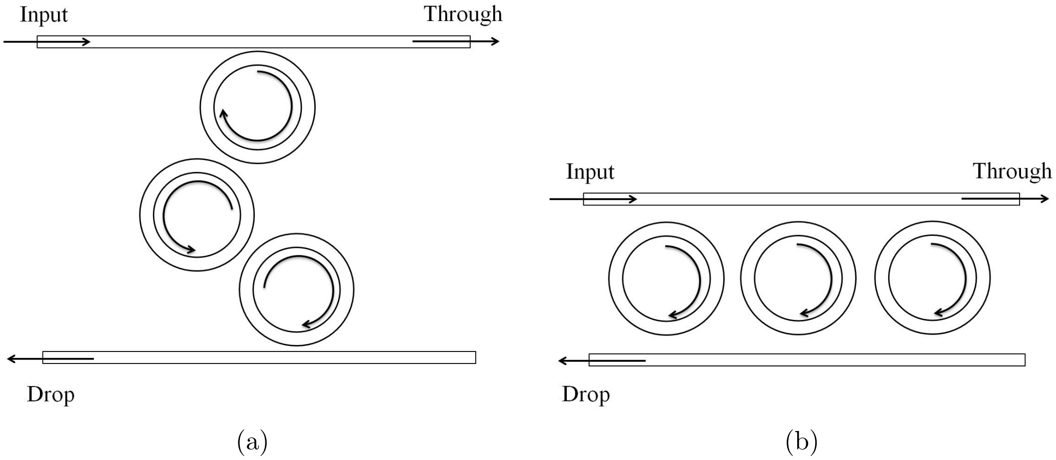

(a) (b)

Figure 3-7: 3-7(a) Schematic of a $3^{rd}$ order ring filter where the rings are directly coupled to each other.3-7(b) Schematic of a parallely cascaded ring filter where the rings are coupled via the bus.

# Chapter 4

# Fabrication and characterization of ring resonators

## 4.1 Fabrication of amorphous silicon rings

Athermal amorphous silicon (a-Si) ring resonators, in this study, are processed by a standard pattern transfer technique using photolithography (Fig. (4-1)).

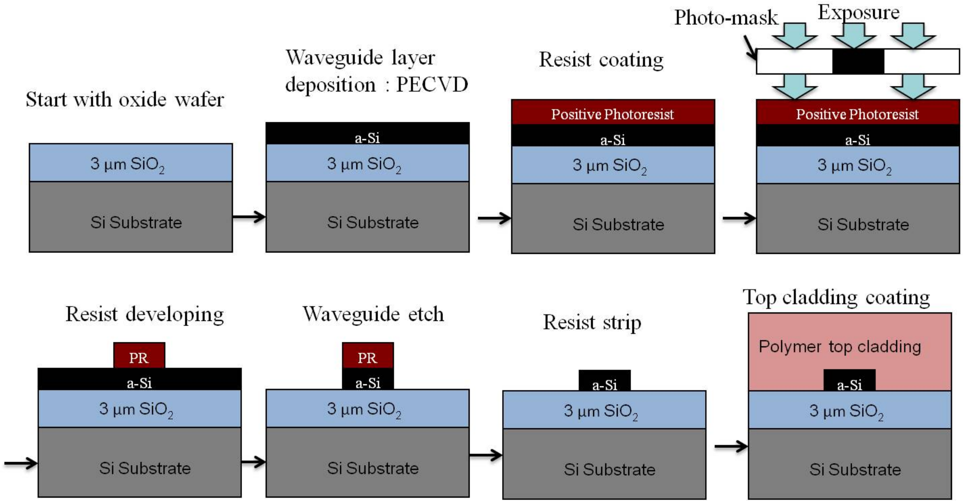

Figure 4-1: Process flow for the fabrication of athermal an a-Si ring resonator

The device deposition is carried out on a Si wafer with a 3 $\mu$m thermal oxide ($SiO_2$) that serves as an under-cladding for an a-Si core. The $SiO_2$ layer is also called the buried oxide (BOX) layer and serves to optically isolate the high index contrast (HIC) waveguide core from the Si substrate. The minimum BOX thickness is determined by the size of the mode inside the HIC waveguide and is chosen to minimize the optical leakage of the mode to the substrate. A standard highly confined SOI waveguide (500 nm × 220 nm) might not require more than 1 $\mu$m thick BOX. However, the need for mode expansion in the polymer cladding for athermal operation called for a thicker 3 $\mu$m BOX layer in this study. The fabrication of optical waveguides requires the optimization at every step of the process flow to minimize the optical loss of the resonators.

1. Plasma enhanced chemical vapor deposition of a-Si: Plasma enhanced chemical vapor deposition (PECVD) is carried out at 200$^o$C using Silane ($SiH_4$, 60 sccm) and Argon (Ar, 300 sccm) to deposit a-Si. The optical absorption associated with a-Si limits its application as a waveguide material. The a-Si is associated with short-range atomic order and can have structural defects arising from distorted bond angles, dangling bonds and altered atomic bonding coordination that alters the density of states near the bandgap. The long-range disorder results in band tails extending into the band-gap [46]. Further, the presence of dangling bonds results in mid-gap states that can act as absorption centers for sub-bandgap light and are the main source of IR absorption in a-Si (Fig. (4-2)).

   The material absorption of a-Si can be reduced significantly by passivating the dangling bonds through hydrogenation of the a-Si film [47]. Hydrogenated a-Si (a-Si:H) is thus preferred for low loss, passive waveguide applications. This thesis uses PECVD as the preferred deposition technique for a-Si:H where imperfect dissociation of $SiH_4$ precursors results in hydrogen incorporation in the film. The deposition power is a key parameter that can be controlled to optimize the hydrogen content of the film. Lower deposition power reduces the kinetic energy used for $SiH_4$ dissociation, thereby, increasing the H content and decreasing the material absorption loss [48]. The deposition power is chosen to be 50 W.

2. Photoresist coating: A positive photoresist that dissolves in a developer post-

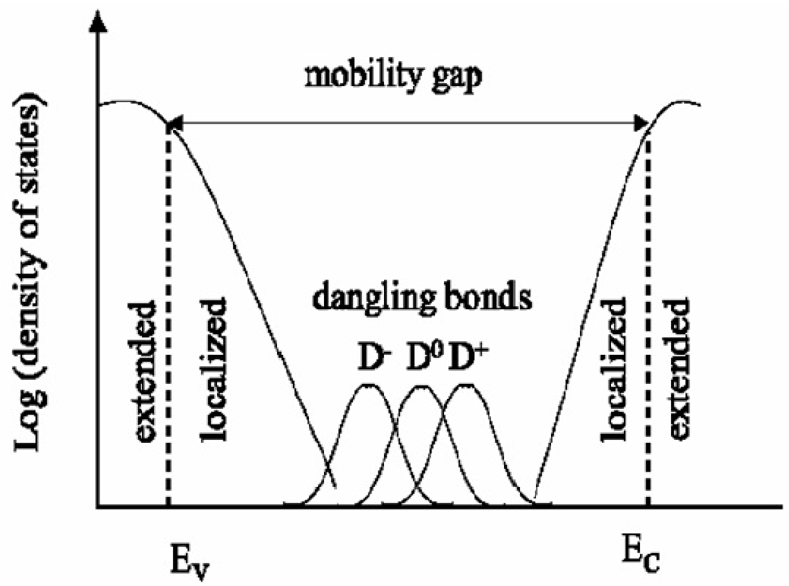

Figure 4-2: Band diagram of amorphous silicon reveals the band tails extending into the band-gap. Mid-gap states associated with dangling bonds are the main source of material absorption of a-Si in near IR regime($\lambda = 1.55\ \mu m$).

exposure is coated on the a-Si film. A positive photoresit is preferred over a negative photoresist because the negative resists swell and are also not preferred for small features. A photo-resist used for i-line stepper usually has 3 components: (a) an inactive resin that resists etching and ion implantation, (b) a photoactive compound (PAC), like diazonaphthoquinones, that inhibits dissolution unless exposed to light and (c) a photoacid generator (PAG) that acts as a chemical amplifier or a catalyst. MEGAPOSIT SPR-700 series from Rohm and Haas is used as the photo-resist and a good adhesion between the photo-resist and a-Si film is ensured by using hexamethyldisiloxane (HMDS, $O[Si(CH_3)_3]_2$) as the adhesion promoter. So, HMDS is first coated on a-Si followed by a HMDS bake at 130$^o$C. This is followed by a 1 $\mu$m thick photoresist coating and pre-exposure bake at 95$^o$C for 60 seconds. The exposure dose during lithography is determined by the thickness of photo-resist. The thickness of the resist is a function of spin speed, viscosity and spin time.

3. Photolithography: An i-line stepper with a wavelength of 365 nm and variable numerical aperture (NA: 0.6-0.66) is used for photolithography. The resolu-

tion ($R$) of lithography, is proportional to the ratio of wavelength over NA ($R = k_1 \frac{\lambda}{NA}$), and is around 550 - 600 nm. $k_1$ is dependent on the resist properties and $NA$ depends on the index ($n$) of the medium. The resolution of the lithography can be improved by adopting a shorter wavelength source (Extreme UV lithography, e-beam lithography, X-ray lithography) or increasing the index of the medium (water or oil immersion lithography). The exposure time during lithography should be sufficient to activate all the PACs to degrade the cross-linking making the resist easier to remove. Shorter exposure time will result in under-exposure of photoresist. The exposure time is optimized at 160 ms for the a-Si waveguides under study.

4. Photoresist development: After exposure, the exposed regions of the positive photoresist get dissolved during the developing cycle. A post exposure bake (PEB) is carried out before the developing process. PEB, at 115$^o$C, eliminates the standing wave pattern generated in the resist during the lithography exposure. Absence of PEB can result in an unwanted sidewall roughness leading to high optical loss. The developer, MEGAPOST LDD-26W, is sprayed for 37 seconds at 400 rpm. A post develop bake is then carried out at 130$^o$C for 60 seconds.

   The continuous spray developing recipe results in scum and roughness in the developed photoresist. The scum results due to greater dissolution of the photoresist in the bulk region compared to the substrate/photoresist interface. As a result, the scum gets transferred with the device to the etch step and an additional step is desired to remove the photoresist scum.

5. Dry/Plasma etching: The first step of dry etching involves removing the photoresist scum (descum) using $O_2$ plasma (flow rate: 30 sccm, Pressure: 150 mTorr, time: 5 seconds, Power: 100 W). The $O_2$ plasma used during the descum results in the formation of a thin oxide layer. This oxide layer is etched using a 10 second $CF_4$ etch (flow rate: 30 sccm, Pressure: 100 mTorr, Power: 400 W).

   Dry etching of a-Si is then carried out using a $Cl_2$/HBr plasma chemistry. The etching time needs to be optimized to minimize optical loss of the waveguide. Under-etching can result in a trapezoidal cross-sections leading to TE/TM mode conversion. Over-etching, on the other hand, can under-cut through $SiO_2$ under-cladding and form air voids at the core/bottom-cladding interface. In this study, the etch step is carried out at high power (350 W) using both $Cl_2$/HBr chemistry for 50 seconds ($Cl_2$: 20 sccm, HBr: 20 sccm, Pressure: 200 mTorr). An over-etch step is also carried out at lower power (75 W) for 10 seconds using only HBr chemistry (40 sccm, 100 mTorr).

6. Photo-resist strip using asher.

7. Top cladding deposition: A hyperlinked fluorinated polymer (EP) is spin-coated at Enablence Inc. The EP polymer clad is UV cured by exposing it for 20 minutes to 5 mW/cm$^2$ (6000 mJ/cm$^2$) from a short arc mercury lamp. The samples are further baked at 150$^o$C in vacuum for 4 hours to enhance cross-linking in the cured polymer. The hydrogen bonds between silanol groups of $SiO_2$ and carboxyl groups of the polymer ensures good adhesion. This prevents polymer delamination from the wafer that is largely $SiO_2$ (under-cladding) with patterns of a-Si. It is useful to point out that the EP has a special primer to adhere to $SiO_2$. So, had the majority of substrate been Si, a special primer specific to Si will have to be added to the polymer to ensure good adhesion. Alternatively, a thin layer of oxide can also be coated on Si.

## 4.2 Transmission measurement of racetrack rings

The transmission measurement system (Fig. (4-3)) uses an input fiber to butt couple the light into the waveguide and uses another output fiber that collects the transmitted light from the waveguide into an optical vector analyzer (OVA). The system uses a Newport auto-align station and a LUNA OVA system that is integrated with an external tunable HP laser source. Later, a new LUNA OVA system with an internally integrated laser source was used, ruling out the need for an external laser source.

The auto-align station has 2 stages, each with 4 degrees of freedom, to precisely control the motion of input and output fibers around the device under test (DUT). Firstly, the input fiber is aligned by placing it closer to the input waveguide facet and using a lens (on the ouput stage) to focus the transmitted light onto an IR camera that is connected to a monitor. A bright spot on the monitor indicates light waveguiding in the device and reflecting a good alignment between the fiber and the input facet of the waveguide. The output fiber (which is connected to an IR detector) is later aligned by measuring the detected power. A surge in measured power reflects a good coupling between the output facet of the waveguide and the fiber. After the coarse alignment, further optimization of the alignment is carried out by a software program that maximizes the output power by independently moving both the fibers in X,Y and Z directions with a precision of ±50 nm.

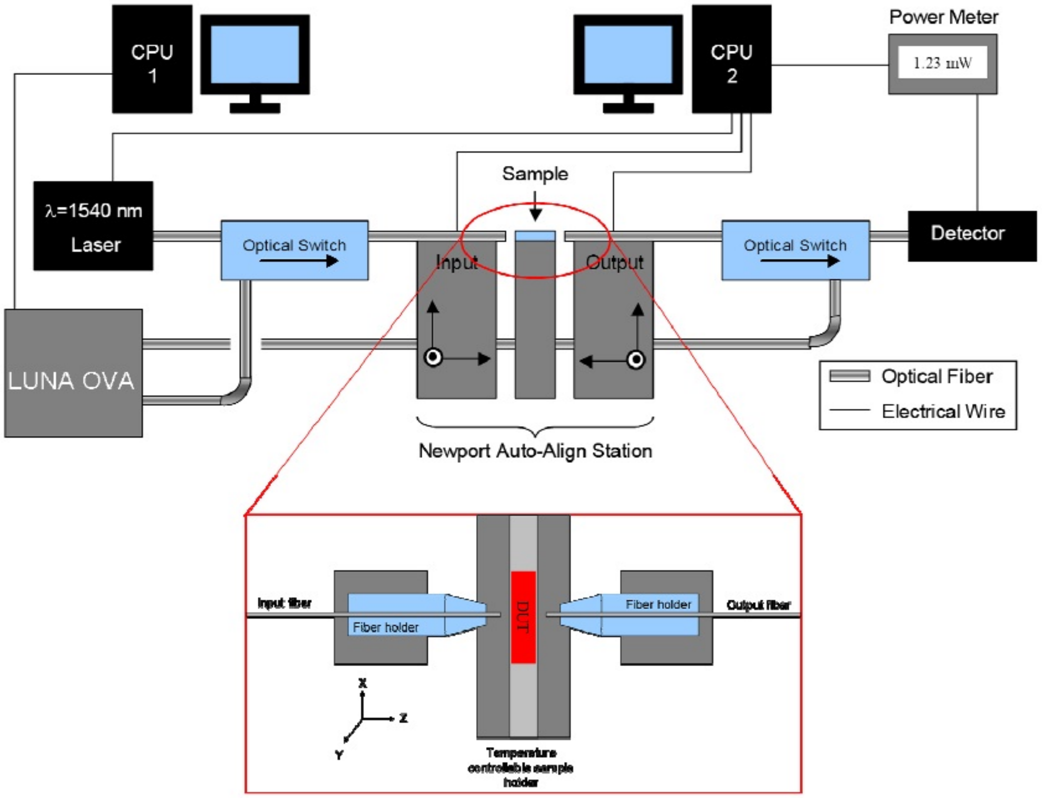

Figure 4-3: Schematic of transmission measurement system used for characterizing ring resonators (courtesy of Dr. Daniel K. Sparacin).

The LUNA OVA system measures all the 4 elements of the Jones Matrix [49], which relates input polarizations (TE and TM components) of an optical system to the output polarization. The Jones matrix is thus a complex transfer matrix that can be written as:

$$\mathbf{J}(\omega) = \begin{bmatrix} a(\omega) & b(\omega) \\ c(\omega) & d(\omega) \end{bmatrix} \tag{4.1}$$

where $a, b, c$ and $d$ are scalar functions and $\omega$ is the angular frequency of the light. Measuring all the elements of Jones matrix enables the LUNA OVA to measure insertion loss, polarization dependent loss, group delay, chromatic dispersion, optical phase and polarization mode dispersion as a function of wavelength (Fig. (4-4)). In this study, the transmission spectrum of a ring resonator corresponds to measured insertion loss (IL) of a given polarization (TE/TM), which is given by

$$IL = -10\log(\frac{|a(\omega)|^2 + |b(\omega)|^2 + |c(\omega)|^2 + |d(\omega)|^2}{2}) \tag{4.2}$$

The basics of ring resonator including its fabrication and measurement techniques covered in this and the preceding chapters is a good starting point for the next chapter which focuses on the most important aspect of this thesis: athermal design of ring resonators.

Type of Measurement: Transmission
Center Wavelength (nm): 1550.00
Wavelength Range (nm): 2.54
Scan Range (nm): 1548.69 - 1551.31
DUT Length Find Method: Broadband
Find Length of DUT (m): 3.000
☐ Continuous Mode
☐ Enable Averaging # 4
Filter Resolution BW (pm): 0.00
Matrix for Res BWs Below: A
TD Window Res BW (pm): 18.48
Convolved Res BW (pm): 18.48
Sync X-Axes To: Top
☑ Matrix A
☐ Matrix B
☐ Matrix C

Figure 4-4: Transmission spectrum of a 300 nm × 220 nm SOI ring (radius: 20 $\mu$m) with polymer over-cladding measured using the LUNA OVA system.

# Chapter 5

# Athermal operation of ring resonators

## 5.1 Thermo-optic effect

The thermo-optic (TO) coefficient of a material is a measure of the temperature dependence of its refractive index and is given by $\frac{dn}{dT}$. The refractive index of any material reflects its polarization per unit volume and can be expressed as a function of the electronic susceptibility ($\chi_e$)and the lattice susceptibility ($\chi_l$) (Eq.(5.1)).

$$n^2 = \epsilon(\omega) = 1 + 4\pi(\chi_e + \chi_l) \tag{5.1}$$

Various models [50–53] of TO coefficients of semiconductors involve expressing their refractive index based on a simple oscillator model before differentiating it with temperature. One such model by Ghosh [50] relates $\chi_e$ to oscillator strength ($F_s$), plasma frequency ($\omega_p$) and optical band gap ($\omega_g$) according to Eq.(5.2).

$$4\pi\chi_e = F_s \frac{\omega_p^2}{\omega_g^2 - \omega^2} \tag{5.2}$$

Identifying that the temperature dependence of $\chi_l$ and $F_s$ are negligible and that $\omega_p^2$ is inversely proportional to volume, the expression for TO coefficient can be derived from Eq.(5.1) as Eq.(5.3).

$$2n\frac{dn}{dT} = F_s[-3\alpha\frac{\omega_p^2}{\omega_g^2 - \omega^2} - \frac{\omega_p^2}{(\omega_g^2 - \omega^2)^2}\frac{d}{dT}(\omega_g^2)] \tag{5.3}$$

Now, the temperature dependence of $\omega_g$ arises mainly due to the increased excitonic transitions as temperature increases. Hence,it is possible to define two kinds of energy gaps based on their temperature dependence, isoentropic band gap ($E_{in}$) and excitonic band gap ($E_{eg}$). While the temperature independent $E_{in}$ determines the dispersion of $2n\frac{dn}{dT}$, the temperature dependent $E_{eg}$ determines the magnitude of TO coefficient. An expression (Eq.(5.4)) relating the TO coefficient,$E_{in}$,$E_{eg}$ and $\alpha$ has been derived in [50]. For semiconductors, the contribution from the first term is negligible due to low values of $\alpha$ ($\approx 10^{-6}/^oC$ ) as compared to $\frac{dE_{eg}}{dT}$ which is approximately $10^{-4}eV/^oC$. Hence, the decrease of $E_{eg}$ with an increase in temperature due to an increase in excitonic transitions results in a positive TO coefficient of many dielectrics. The only exception to this behavior is exhibited by $TiO_2$ with its negative TO coefficient [54, 55]. However, the reason behind the anomolous behavior of $TiO_2$ is not clear and requires further investigation.

$$2n\frac{dn}{dT} = K^2[-3\alpha R_\lambda - \frac{1}{E_{eg}}\frac{dE_{eg}}{dT}R_\lambda^2] \tag{5.4}$$

where K is a constant related to the low frequency index $n_o$ in the IR region as $K^2 = n_o^2 - 1$ and $R_\lambda$ is the normalized dispersive wavelength given by $R_\lambda = \lambda^2/(\lambda^2 - \lambda_{ig}^2)$.

On the other hand, for organic materials like polymers,the refractive index is related to their packing density (free volume), polarizability (molar refraction) and the difference between their maximum absorption wavelength and the used optical wavelength [56]. The Lorenz-Lorenz equation (Eq.(5.5)) is used to describe the relation between refractive index ($n$), molar refraction ($R$) and molar volume ($V$) of a polymer [57].

$$\frac{n^2 - 1}{n^2 + 2} = \frac{R}{V} \tag{5.5}$$

The TO coefficient of polymers can be derived from Eq.(5.5) as follows:

$$2n\frac{dn}{dT} = \frac{3}{(1-x)^2}\frac{dx}{dT}, where\ x = \frac{R}{V} \tag{5.6}$$

$$\frac{dx}{dT} = \frac{1}{V}\frac{dR}{dT} - x\alpha_V,\ where\ \alpha_V\ is\ the\ volume\ expansion\ coefficient \tag{5.7}$$

For polymers, it is the second term in Eq.(5.7) involving the volume expansion coefficient that dominates the TO coefficient giving it a negative sign. Hence from Eqs. (5.5), (5.6), and (5.7), a relation (Eq.(5.8)) between the TO coefficient, $n$ and $\alpha_V$ can be derived [58].

$$\frac{dn}{dT} = -\frac{(n^2-1)(n^2+2)}{6n}\alpha_V \tag{5.8}$$

In an electronic-photonic architechture,local temperature fluctuations due to on-chip electronics result in TO peak shifts of silicon based optical filters. Active thermal compensation by heaters and thermo-electric coolers are the legacy solution for low-density integration. In fact, the silicon CMOS layered architecture was recently shown to be ideal for embedded thermo-optic phase shifters for tuning complex filters [12]. However, the required electrical power and the number of I/O lines ultimately limit integration density thereby motivating the need for a passive athermal design.

## 5.2 Passive athermal design

For an assymetric channel waveguide system with different top and bottom cladding, the effective TO coefficient ($\frac{dn_{eff}}{dT}(\lambda)$) can be expressed as a function (Eq.(5.9))of the TO coefficient of the core ($\frac{dn_c}{dT}(\lambda)$), the top cladding ($\frac{dn_{tcl}}{dT}(\lambda)$) and the bottom cladding ($\frac{dn_{bcl}}{dT}(\lambda)$) weighed by their respective confinement factors ($\Gamma_c(\lambda), \Gamma_{tcl}(\lambda)$, and

$\Gamma_{bcl}(\lambda)$)

$$\frac{dn_{eff}}{dT}(\lambda) = \Gamma_c(\lambda)\frac{dn_c}{dT}(\lambda) + \Gamma_{tcl}(\lambda)\frac{dn_{tcl}}{dT}(\lambda) + \Gamma_{bcl}(\lambda)\frac{dn_{bcl}}{dT}(\lambda) \tag{5.9}$$

Eq.(5.9) is a first order approximation of the refractive index variation with temperature where the variation of $\Gamma$ with temperature and the second order variation of the refractive index of the core and cladding are ignored. Also the effect of the thermal expansion coefficient of the substrate on the waveguide geometry is negligible. Finally, the wavelength dispersion of TO coefficient, across the C band, of the core and the cladding is neglected due to the very low dispersion of optical materials considered in this thesis. Now, the confinement factor ($\Gamma$) in Eq.(5.9) is a measure of the electromagnetic power in a given region as defined by Robinson et.al. [59] and is a function of the operating wavelength. Note that $\Gamma$ can be expressed as a product of a term related to the group velocity and confinement of the electric fieled density (Eq.5.10). Hence, the value of $\Gamma$ can be greater than 1 if the group index ($n_g$) is greater than the bulk index and the spatial confinement of electric field density ($\gamma$) is close to 1.

$$\Gamma_{c/tcl/bcl} = \frac{n_g}{n_{c/tcl/bcl}} \frac{\int\int_{c/tcl/bcl} \epsilon \left|E\right|^2 dxdy}{\int\int_{\infty} \epsilon \left|E\right|^2 dxdy} \equiv \frac{n_g}{n_{c/tcl/bcl}} \gamma_{c/tcl/bcl} \tag{5.10}$$

The athermal operation of a waveguide system is defined by the null condition of $\frac{dn_{eff}}{dT}$, which from Eq.(5.9) can be reached only if the cladding has a negative thermo-optic coefficient. Motivated by this theory, polymer cladding has been used for passive athermal compensation of silicon waveguides [19, 60–70]. Alternatively, other design schemes involving interference based devices have been employed for passive thermal compensation [71,72]. However, this thesis employs a polymer cladding based solution where the design rule involves squeezing a portion of the mode into the polymer to compensate for the positive TO effects from the core(Fig.(5-1)). This calls for a clear understanding of the governing parameters to design a working prototype.

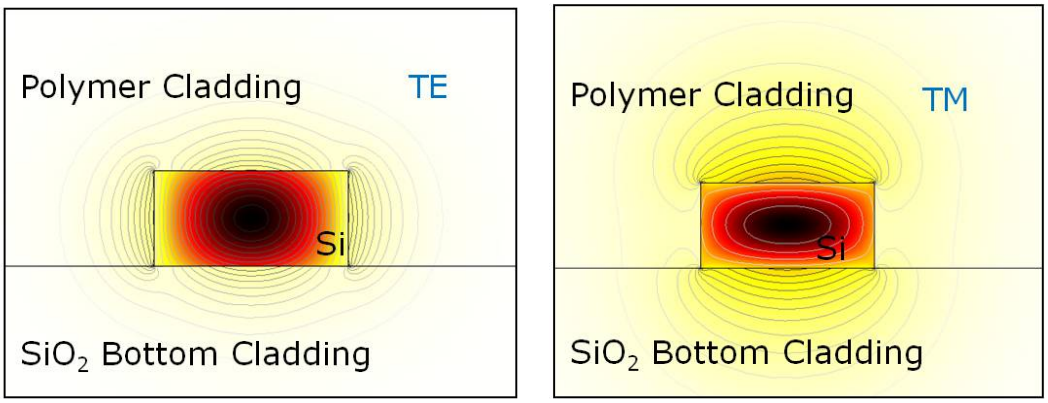

(a) Athermal TE prototype (b) Athermal TM prototype

Figure 5-1: Passive athermal design rule involves expanding the mode into the polymer cladding with negative TO to compensate for the positive TO effects of the Si core

## 5.3 Athermal prototype design

The governing parameters for the passive athermal design can be inferred from Eq.(5.9) as follows:

1. TO coefficient of the core ($\frac{dn_c}{dT}$) : fixed by the core material choice.
2. TO coefficient of the cladding ($\frac{dn_{cl}}{dT}$): fixed by the polymer cladding choice.
3. Confinement factors ($\Gamma_c(\lambda), \Gamma_{cl}(\lambda)$): Depends on the waveguide cross-section, index contrast and the wavelength of operation.

We focus on the application of athermal add-drop filters in the back end of line (BEOL) interconnect stack where the thermal budget constraints the deposition temperature to less than 400$^o$C. We choose amorphous Si (a-Si) as the core choice as its deposition temperature (350$^o$C) satisfies the thermal budget constraint. The high TO coefficient of a-Si (Table 5.1)requires a polymer with an equally high magnitude of the TO coefficient. A proprietary hyperlinked fluorinated acrylate based polymer (EP) provided by Enablence Inc. is used as the polymer over-cladding (Table 5.1). A 3 $\mu$m thick SiO$_2$ is used as the under-cladding and its effect on the effective TO is negligible due to its low TO coefficient (Table 5.1).

| **Materials Type** | **Si** | **amorphous-Si** | **$SiO_2$** | **$Si_3N_4$** | **EP** |
|---|---|---|---|---|---|
| **Index at 1.55$\mu$m** | 3.5 | 3.48 | 1.46 | 2.05 | 1.38 |
| **dn/dT** ($\times 10^{-4} K^{-1}$) | 1.8 | 2.3 | 0.1 | 0.4 | -2.65 |

Table 5.1: Refractive index and TO coefficients of optical materials used in this thesis

Two different a-Si cross-sections (700 nm × 206 nm and 700 nm × 216 nm) corresponding to the single TM mode of operation are chosen for prototype demonstration. The devices are a-Si racetrack rings (Fig.(5-2)) with varying coupling lengths (10 $\mu$m, 50 $\mu$m, 100 $\mu$m and 150 $\mu$m) and coupling gaps (500 nm, 550 nm, 600 nm and 650 nm). Also one set of devices are cladded with CVD oxide to be used as a reference, while the other set of devices are spun with hyperlinked fluoropolymer (EP).

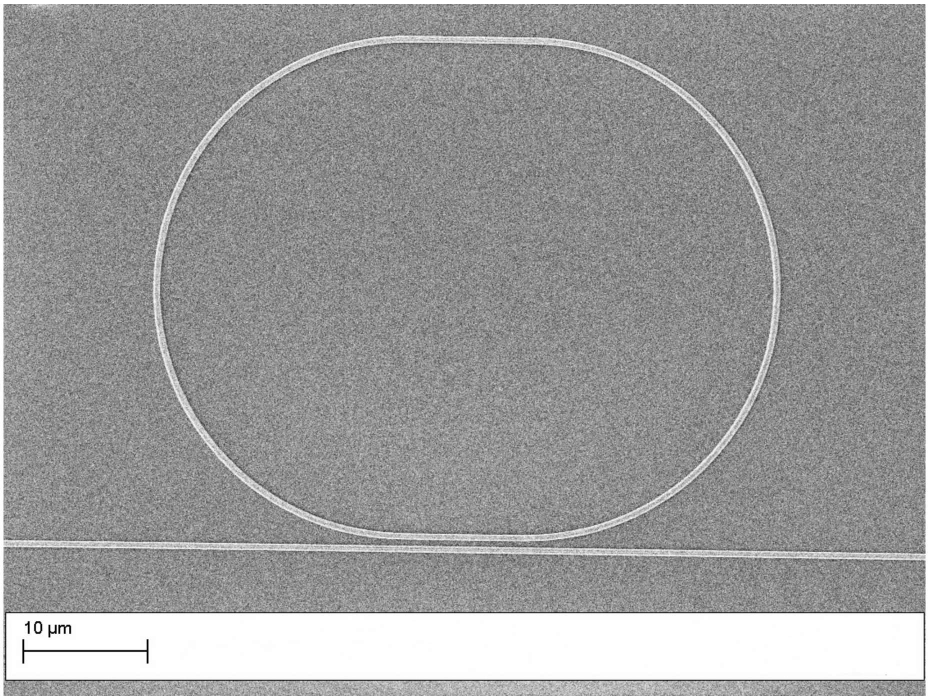

Figure 5-2: SEM image of the top view of an unclad a-Si racetrack ring

Any variation in the operating temperature of such a ring changes the resonant wavelength ($\lambda_r$) by a magnitude determined by the effective TO of the ring (Eq.(5.11))

$$\frac{1}{\lambda_r}\frac{d\lambda_r}{dT} = \frac{1}{n_g}\frac{dn_{eff}}{dT} \tag{5.11}$$

## 5.4 Athermal prototype performance

The TM transmission spectra measured around 1550 nm at various temperatures shows significant TO compensation with the EP cladding as compared to the oxide cladded devices (Fig.(5-3(a))). The TO peak shift at 1524 nm is reduced by 2 orders of magnitude from 63 pm/K for an oxide cladded ring (700 nm × 216 nm) to 0.5 pm/K for an EP cladded ring (700 nm × 206 nm) thereby exhibiting complete TO compensation (Fig.(5-3(b))). The glass transition temperature of EP lies below room temperature and hence outside the operating range of our interest ($25^o$C-$125^o$C). Hence,the higher order variations due to the polymer glass transition can be ignored in these measurements.

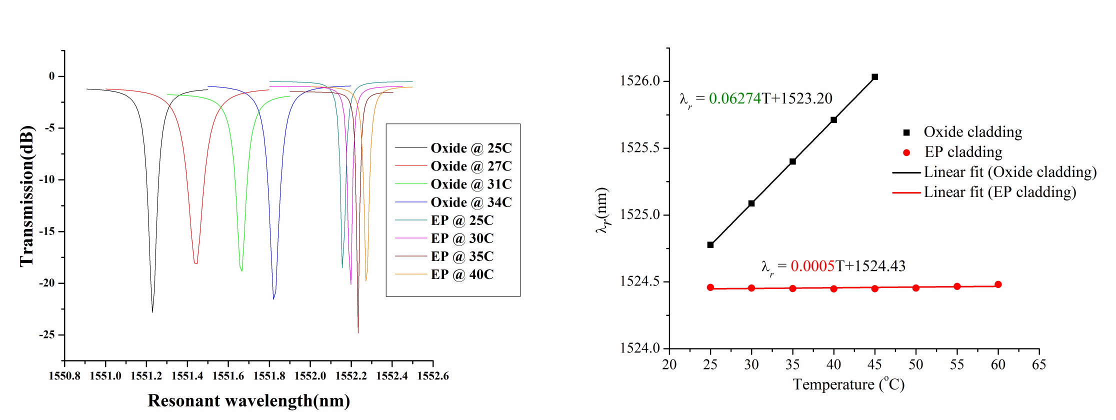

(a) (b)

Figure 5-3: 5-3(a) The transmission spectra showing the resonance peak shift with temperature for both oxide clad and polymer clad devices. We compare a-Si rings of the same cross-section (700nm×216nm) and different top claddings (oxide and polymer). In the case of an oxide clad ring, the positive TO coefficient of both core and cladding result in a positive peak shift of 63 pm/K. There is significant TO compensation for the polymer clad ring and the peak shift is reduced to 7 pm/K for this waveguide design.5-3(b) Plot of resonance variation with temperature around 1524 nm shows complete thermal compensation for a polymer cladded ring (0.5 pm/K) with a cross-section of 700 nm× 206 nm. On the other hand,the oxide cladded ring with a cross-section of 700 nm× 216 nm shows a TO peak shift of 64 pm/K around the same wavelength

### 5.4.1 Wavelength dependency

According to Eq.(5.9), $\frac{dn_{eff}}{dT}$ varies depending on the operating wavelength. This arises because of the waveguide dispersion where the confinement factor ($\Gamma(\lambda)$) decreases with increasing wavelength due to a longer evanescent tail.This dependence proves even more crucial for waveguides of dimensions 700 nm$\times$ 216 nm. This is because the wavelength of interest is in the near IR regime (1450 nm - 1550 nm) and has a magnitude in the core ($\lambda/n_{core}$)that is comparable to the core dimension. The model thus predicts a lower TO peak shift at longer wavelengths. In other words, as the propagating wavelength increases at a constant waveguide dimension, the effective TO contribution from the cladding increases. The experimentally measured TO values of the prototypes, over a wide wavelength range, are consistent with the proposed model(Fig.(5-4)). The consistency between the experimental results and simulated (FIMMWAVE simulations) behavior can be clearly seen(Fig.(5-4)).

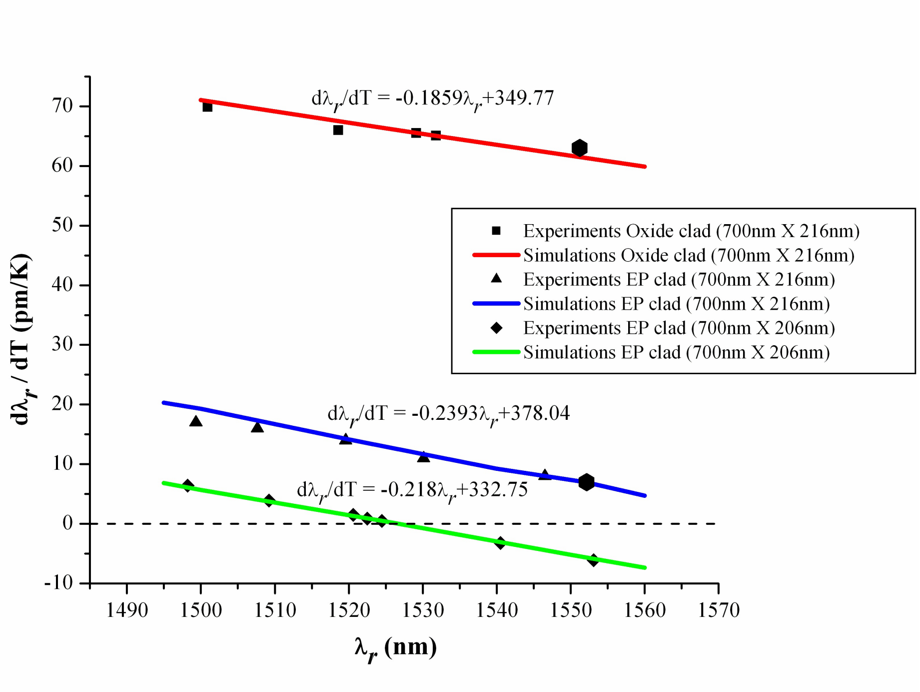

Figure 5-4: Experimental results showing the TO peak shift variation with the wavelength for TM mode propagation. The slope reflects the associated waveguide dispersion. The wavelength at the dashed-line crossover point is an unique condition for athermal behavior. The hexagonal bold data points correspond to the spectral data shown in Fig.(5-3(a))

The measurements for each resonant wavelength were carried out between 25$^o$C-60$^o$C and every data point is a linear regression of 8 data points taken at every 5$^o$C interval. For large resonance shifts (TDWS$\geq$10pm/K), R$^2$ $\geq$0.99, and for near athermal performance (TDWS$\leq$1pm/K), R$^2$ $\geq$0.94 due to the reduced linear correlation arising from the residual second order terms discussed below. The magnitude of the slope (Fig.(5-4)) depends on the waveguide cross-section and the TO coefficient contrast between the core and the cladding as can be inferred from Eq.(5.9). Hence for a given cross-section, the slope will be larger for the EP polymer cladding as the contribution from the second term in Eq.(5.9) becomes significant. Further, for a TM mode,$\Gamma(\lambda)$ varies significantly with changes in the height of the waveguide. This is verified by obseving a lower TO peak shift for a thinner 700 nm× 206 nm waveguide when compared to a thicker 700 nm× 216 nm for a given $\lambda$ (Fig.(5-4)).

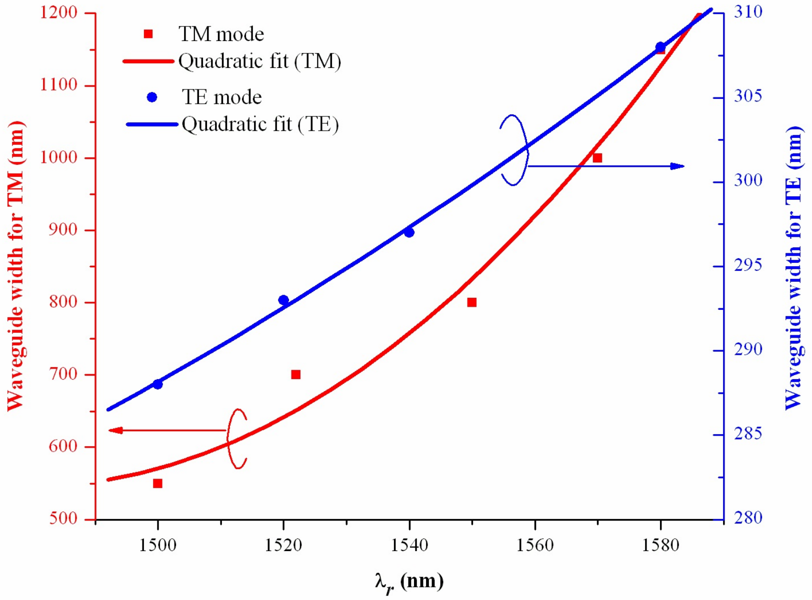

Figure 5-5: Variation of athermal waveguide width with wavelength for TE and TM modes. These simulation results are for a a-Si waveguide of 206 nm height with an SiO$_2$ underclad and EP polymer over-cladding. The desired waveguide width for athermal operation increases with wavelength to keep the confinement factor constant.

The observed wavelength dependent TO peak shift implies that athermal operation can be achieved at only one wavelength for a given waveguide dimension. This dependence imposes an additional design constraint that requires different desired waveguide dimensions for different resonant wavelengths to achieve athermal operation. Consequently, for a single WDM implementation, the mask design should incorporate varying waveguide widths when the height of the waveguide (layer thickness) is fixed. Fig.(5-5) plots the range of the wavelength dependent variation in waveguide dimensions for athermal operation of both TE and TM modes. The simulation assumes an a-Si ring with an oxide under-cladding and EP polymer over-cladding. The height of the a-Si waveguide is fixed at 206 nm and the athermal width corresponding to a TO peak shift $\leq 0.5$ pm/K is calculated for various wavelengths. The desired width varies from 550 nm (at 1500 nm) to 1150 nm (at 1580 nm) as the wavelength increases for the TM mode of operation. Such a large variation in waveguide width can be correlated to the small dependence of the confinement factor of a TM mode on the width in comparison to the height variation. Conversely, one can expect to achieve athermal operation of a TE mode over a smaller range of widths for a given range of wavelengths. The stronger dependence of $\Gamma$ of a TE mode on the width of the waveguide can be clearly seen in Fig.(5-5).

### 5.4.2 Mode dependent athermal design

The passive design rule states that athermal operation is achieved universally for a particular confinement factor resulting from a selected core-polymer cladding system. This confinement factor is however reached at different waveguide dimensions for TE and TM modes. For example, the reduction of the confinement factor is more effectively achieved by reducing the waveguide width for a TE mode and by reducing its height for a TM mode. FIMMWAVE simulations were used to estimate the range of width variations required for athermal operation in TE and TM modes for an a-Si core (Fig.(5-5)). Experimental verification was done using SOI as the core choice. Silicon ($n : 3.5, TO : 1.86\times10^{-4}$) rings of various widths (290 nm, 300 nm and 320 nm) were fabricated in an all-pass configuration (Fig.(5-6(a))) using e-beam lithography on an SOI wafer with a 3$\mu$m SiO$_2$ ($n : 1.45, TO : 1 \times 10^{-5}$) buffer acting as an under-cladding [73, 74]. For the TM mode of operation, wider waveguides (500 nm, 550 nm and 600 nm) with racetrack configurations (Fig. (5-6(b)) with a 20 $\mu$m coupling length were chosen to enhance the coupling between the bus and the ring. The rings were then cladded with a hyperlinked fluoropolymer, EP ($n : 1.38, TO : -2.65\times10^{-4}$), at Enablence Inc. The polymer clad was further UV cured using a short arc mercury lamp and baked at 150$^o$C in vacuum for 4 hours to enhance the cross-linking.

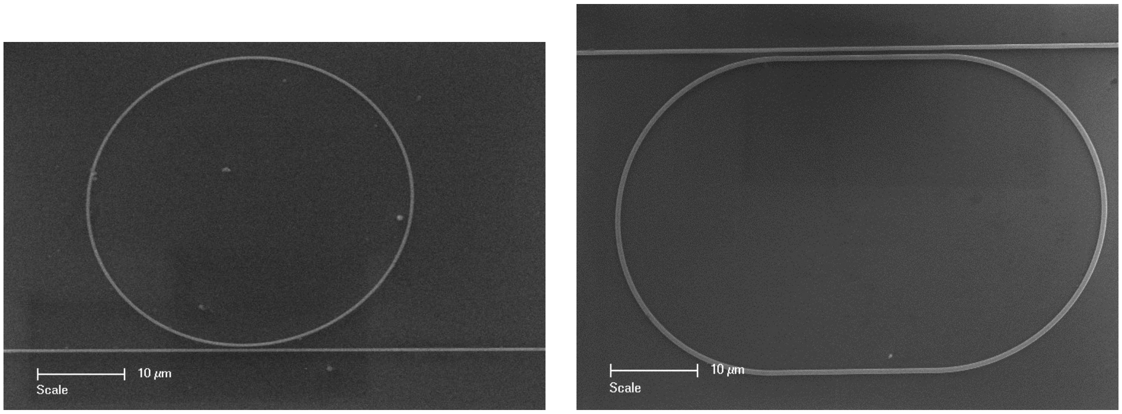

(a) (b)

Figure 5-6: 5-6(a) Top view of an unclad SOI ring, with a waveguide width of 320 nm and radius of 20 $\mu$m, which has been designed for athermal operation under TE mode. 5-6(b) Athermal operation under TM mode requires wider ring waveguide width. The racetrack configuration corresponds to a 500 nm wide bus waveguide coupled to a ring waveguide (width: 600 nm, radius: 20 $\mu$m) over a 20 $\mu$m coupling length

Transmission measurements of the rings between 20$^o$C-40$^o$C reveal the TO behavior. The 320 nm wide waveguide exhibits athermal performance around 1566 nm for TE mode of operation (Fig. (5-7)). As predicted, the narrower waveguides (290 nm and 300 nm) exhibit negative TO peak shifts due to over-compensation from the polymer cladding. Similarly, the wider waveguides (500 nm, 550 nm and 600 nm) designed for athermal operation for TM mode exhibit negative TO peak shifts with the magnitude decreasing with increasing widths. The TM mode of a 600 nm wide waveguide exhibits a TO peak shift of -2.5 pm/K at 1532 nm (Fig. (5-7)).

The TO peak shift increases with the waveguide width for a given wavelength due to increased confinement. Similarly, increasing the wavelength for a given width

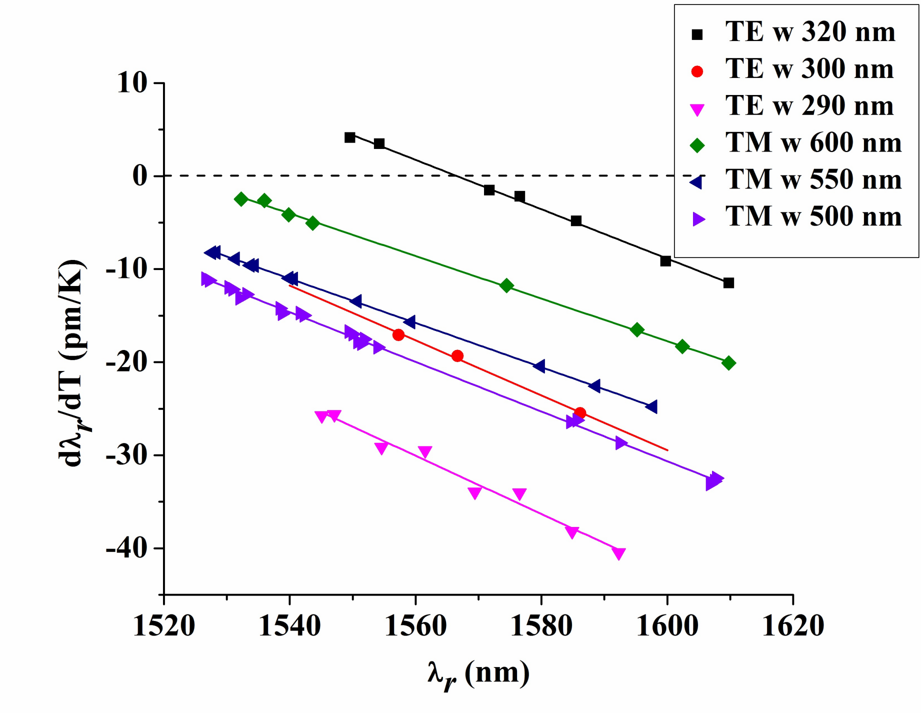

Figure 5-7: TO performance of EP cladded SOI TE and TM waveguides with different dimensions and their dependency with wavelength.

decreases the confinement resulting in lower TO peak shift. An empirical relation (Eq. (5.12)) between the TO peak shift (pm/K), wavelength (nm) and width (nm) can be derived for both TE and TM modes from the TO plots (Fig. (5-7)). There exists a unique waveguide width for a given wavelength where the TO peak shift vanishes resulting in an athermal behavior. At a wavelength of 1550 nm, the athermal channel cross-sections corresponding to TE (316 nm × 220 nm) and TM modes (658 nm × 220 nm) can be deduced from Eq. (5.12).

$$TE: \frac{d\lambda_r}{dT} = 0.2078444\lambda_r + 3.3019555w - 0.0014789\lambda_r w - 640.905778 \tag{5.12a}$$

$$TM: \frac{d\lambda_r}{dT} = -1.0083999\lambda_r - 1.9056333w + 0.0012997\lambda_r w + 1491.37999 \tag{5.12b}$$

### 5.4.3 Residual second order effects

Residual second order terms become significant at very small resonance shifts ($\leq$2 pm/K) when the first order terms vanish according to according to Eq.(5.9). It is a reasonable assumption that the resonant wavelength shifts linearly with temperature, and it is largely governed by Eq.(5.9) and Eq.(5.11). Such linear relations hold true for relatively large peak shifts($\geq$ 10pm/K). However at extremely small wavelength shifts, the second order contributions arising from the variation of $\Gamma$ with temperature and the second order contributions from the refractive index become significant and cannot be neglected. In theory, with an increase in temperature, the refractive index of the core increases and that of the polymer cladding decreases, thereby increasing the $\Gamma$ resulting in a larger peak shift. Thus the refractive index variation including the second order term can be written as follows:

$$\begin{aligned} dn_{eff}(n_c, n_{cl}) = {} & [\Gamma_c \frac{\partial n_c}{\partial T} + \Gamma_{cl} \frac{\partial n_{cl}}{\partial T}]dT \\ & + \frac{1}{2}[\Gamma_c \frac{\partial^2 n_c}{\partial T^2} + \Gamma_{cl} \frac{\partial^2 n_{cl}}{\partial T^2} + \frac{\partial \Gamma_c}{\partial n_c}(\frac{\partial n_c}{\partial T})^2 + \frac{\partial \Gamma_{cl}}{\partial n_{cl}}(\frac{\partial n_{cl}}{\partial T})^2 \\ & + \frac{\partial \Gamma_c}{\partial n_{cl}} \frac{\partial n_c}{\partial T} \frac{\partial n_{cl}}{\partial T} + \frac{\partial \Gamma_{cl}}{\partial n_c} \frac{\partial n_c}{\partial T} \frac{\partial n_{cl}}{\partial T}]dT^2 \end{aligned} \tag{5.13}$$

where $\Gamma_c$ and $\Gamma_{cl}$ are the confinement factors of the core and the cladding (only the polymer top cladding is considered) respectively. The second order terms can be categorized into two types of contributions:

1. the term $\frac{1}{2}[\Gamma_c \frac{\partial^2 n_c}{\partial T^2} + \Gamma_{cl} \frac{\partial^2 n_{cl}}{\partial T^2}]$ corresponds to the second order TO coefficients of the core and cladding materials;
2. the term $\frac{1}{2}[\frac{\partial \Gamma_c}{\partial n_c}(\frac{\partial n_c}{\partial T})^2 + \frac{\partial \Gamma_{cl}}{\partial n_{cl}}(\frac{\partial n_{cl}}{\partial T})^2 + \frac{\partial \Gamma_c}{\partial n_{cl}} \frac{\partial n_c}{\partial T} \frac{\partial n_{cl}}{\partial T} + \frac{\partial \Gamma_{cl}}{\partial n_c} \frac{\partial n_c}{\partial T} \frac{\partial n_{cl}}{\partial T}]$represents the TDWS due to the variation of confinement factors at different temperatures.

The experimental variation of resonant wavelength with temperature for a 700 nm×206 nm a-Si ring resonator with an EP cladding confirms the predicted second order behavior (Fig.(5-8)).

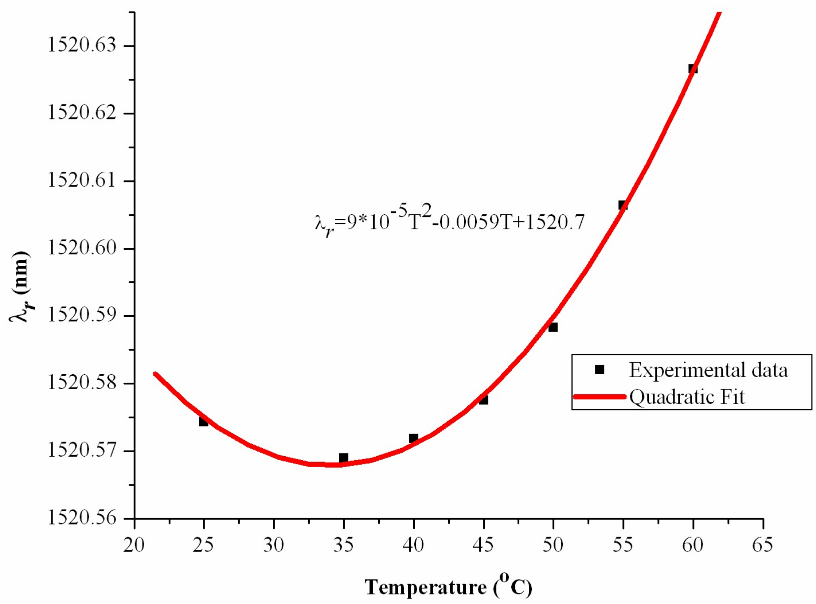

Figure 5-8: The measured second order variation of resonant wavelength of an a-Si ring (cross-section: 700 nm × 206 nm) with an EP top cladding.The residual second order effects become important when the first order terms vanish at low peak shifts. The quadratic term has contributions from the temperature dependence of the confinement factor and from the second order material coefficients.

FIMMWAVE simulations can be used to estimate the dependence of $\Gamma$ on temperature.The experimental residual quadratic term ($9 \times 10^{-5} \pm 1 \times 10^{-5}$ nmK$^{-2}$) is of the same order of magnitude predicted in the FIMMWAVE simulation ($2 \times 10^{-5} \pm 1 \times 10^{-6}$ nmK$^{-2}$). The higher value of the experimental second order term suggests a significant contribution from the second order material coefficients,$\frac{\partial^2 n_c}{\partial T^2}$ and $\frac{\partial^2 n_{cl}}{\partial T^2}$, that were neglected in the simulations (first 2 second order terms in Eq. (5.13)). The second order material TO coefficient is just a reflection of the anhormonicity of the refractive index of a material. In other words, the dependence of the index of a material with temperature is not strictly linear and has a residual quadratic term that becomes significant when dealing with extremely small effective index changes. The first 2 second order terms of Eq. (5.13) can be calculated based on the experimentally observed quadratic term. A value of $4 \times 10^{-7} \pm 1 \times 10^{-7}$ K$^{-2}$for the second order material coefficient of the waveguide system (in other words, second order effective material

TO coefficient) is inferred. This is a reasonable value for the polymer clad system given that the reported second-order TO of a-Si is around $1.43 \times 10^{-6}\mathrm{K}^{-2}$ [75].

## 5.5 Concluding remarks

This chapter explains the physics of the TO effect and reports the design criteria and the performance of a-Si ring resonators for passive athermal WDM applications. The waveguide design rules address i) positive-negative TO composite structures with polymer top cladding, ii) resonant wavelength dependent geometry to achieve constant confinement factor ($\Gamma$), and iii) observation of small residual second order effects. The chapter develops exact design requirements for a TO peak shift of 0 pm/K and presents a prototype with a TO stability of 0.5 pm/K.

In this chapter, the polymer material, provided by Enablence Inc, has been treated as a "black box" with a given refractive index and a TO coefficient that are not necessarily optimized for athermal application. The next chapter focuses on the polymer material choice. Specifically, the possibility of tailoring the optical properties by changing the extent of cross-linking in a polymer is explored.

# Chapter 6

# Polymer design for high performance athermal photonic circuits

## 6.1 Polymers in optics

A wide gamut of properties like tunable refractive index (1.3-1.6), low optical loss, high flexibility, high toughness, ease of processibility and integration over inorganic components make polymers attractive candidates for different components of an optical circuit.Polymer based optical waveguides for broadband communications have been proposed and studied extensively [56,76]. Furthermore, high electro-optic (EO) and TO coefficients of polymers have been utilized for polymer based EO modulators [77–80], EO switches [81], TO switches [82,83], and athermal Si filters [84].

Various polymers like poly(methylmethacrylate) (PMMA) with an aliphatic backbone, polycarbonate (PC) with ester backbone, polyurethane (PU) with amino-ester backbone, polystyrene (PS) with aromatic chain and epoxy resin have been conventionally used for optical applications. Their differing backbone structures result in a wide gamut of optical properties (refractive index and material loss), thermal stability and mechanical robustness (Table 6.1).The TO coefficients in Table 6.1 have been calculated using Eq. (5.8) and the reported thermal expansion coefficients [85]. However, the conventional polymers do not satisfy all the requirements of an optical device in terms of high thermal stability ($T_g$>250$^o$C), low loss (<0.1 dB/cm at 1550 nm), low birefringence, high photo-sensitivity and low polarization dependent loss (PDL).

| **Material** | $n$ | **TO coeff ($K^{-1}$)** | **$T_g$($^o$C)** | **Loss (dB/cm)** |
|---|---|---|---|---|
| PMMA | 1.49 | $-1.4\times10^{-4}$ | 105 | 0.2(@ 850 nm) |
| PS | 1.59 | $-1.7\times10^{-4}$ | 100 | |
| PU | 1.58 | | 145 | |
| PC | 1.56 | $-1.42\times10^{-4}$ | | 0.8(@ 633 nm and 1064 nm) |
| Epoxy Resin | 1.58 | | | 0.3(@ 633 nm),0.8(@1064 nm) |

Table 6.1: Properties of conventional optical polymers [56]

More recently, novel polymers targeting specific optical functionalities have been developed by companies like DuPont, DOW, Corning, NTT etc. Deuterated and halogenated polyacrylates have low stress-optic coefficients and low material loss [56]. They are attractive for optical devices that desire low scattering loss, low birefringence and ease of fabrication. Further, their sensitivity to UV radiation makes it suitable to tune their refractive index between 1.3-1.6 by changing the cross-linking. Fluorinated polyimides are another class of novel polymers that have been developed for high thermal stability (>300$^o$C) and excellent dielectric and mechanical properties. However, they do suffer from high optical losses due to the formation of scattering centers and charge-transfer complexes during the ordering processes that occur during their deposition. Further, the aromatic ordering in polyimides result in a large birefringence and PDL. Perfluorocyclobutyl (PFCB) aryl ether polymers, developed by DOW, overcome the processing limitations of spin-coated polymers where the thickness and planarity of the film is determined by its solubility in the solvent. PFCB synthesized through thermal cyclopolymerization possesses high thermal stability ($T_g$: 120-350$^o$C), low optical loss (<0.25 dB/cm at 1550 nm), precisely tunable refractive index (1.449-1.508 at 1550 nm), low birefringence, low moisture absorption, high TO coefficient and high optical stability. Fluorinated dendrimers form another class of polymers that can be employed as surfactants due to their hydrophobicity, lipophobicity, chemical resistance, low cohesive force, low viscosity and high solubility. However, they do suffer from tedious synthetic schemes. Finally, non-linear centro-symmetric alignment of non-linear optic (NLO) chromophores have been leveraged to realize EO polymers by doping or covalently bonding the chromophores in poled polymers (dendritic family for instance).

## 6.2 Polymer requirements for athermal design

The optical parameters governing the polymer choice for athermal silicon add-drop filters in BEOL interconnect stack can be listed as follows:

1. Refractive index: The refractive index of any polymer ranges between 1.3-1.6. Passive athermal design rule requires low confinement in the core as the mode needs to expand into the polymer cladding. For a given core choice, confinement goes down with decreasing index contrast between the core and the cladding. Hence, the desired polymer should have an index that falls in the higher end of the spectrum (closer to 1.5-1.6).

2. TO coefficient: The chosen polymer should have a TO coefficient magnitude that is comparable to that of the core choice. The TO coefficients of the polymer family range from $-1 \times 10^{-4}\ K^{-1}$ to $-4 \times 10^{-4}\ K^{-1}$. This is an order of magnitude higher than that of $Si_3N_4$ and $SiO_2$, but comparable to those of silicon and amorphous silicon (Table 5.1). In other words, for a given polymer choice, athermal operation can be reached at a much higher confinement for a $Si_3N_4$ core as compared to Si and a-Si core choices.

3. Optical loss: The need for low power consumption requires a low optical loss at the major telecommunications wavelength (1310 nm and 1550 nm). There are several sources of optical losses including absorption, scattering, bending, polarization dependence,reflections, radiations and fiber coupling. However, while considering polymer material selection, absorption loss is the main source of loss that needs to be investigated. Electronic absorptions fall in the UV

regime and are unlikely to have any signifcant contributions in the telecommunications window. Absorptions due to molecular vibrational overtones are the dominant source of polymer material loss in the 1300-1600 nm range. In particular, C-H and O-H overtones are highly absorptive (keeping the fundamental vibration of C-H aliphatic bond as a reference) in the wavelengnths of interest (Table 6.2). C-F overtones, on the other hand, exhibit a lower absorption due to the higher overtone order in the telecommunications range. Hence, hydrogen removal through fluorination (or halogenation) brings down the loss of optical polymers significantly. For athermal applications, we desire a fluorinated polymer whose material loss can be as low as 0.1 dB/cm [76] at the key communication wavelengths.

| **Bond** | **Overtone order** | **Wavelength (nm)** | **Relative Intensity** |
|---|---|---|---|
| C-H | 1 | 3390 | 1 |
| C-H | 2 | 1729 | $7.2\times10^{-2}$ |
| C-H | 3 | 1176 | $6.8\times10^{-3}$ |
| C-D | 3 | 1541 | $1.6\times10^{-3}$ |
| C-D | 4 | 1174 | $1.3\times10^{-4}$ |
| C-F | 5 | 1626 | $6.4\times10^{-6}$ |
| C-F | 6 | 1361 | $1.9\times10^{-7}$ |
| C-F | 7 | 1171 | $6.4\times10^{-9}$ |
| C=O | 3 | 1836 | $1.2\times10^{-2}$ |
| C=O | 4 | 1382 | $4.3\times10^{-4}$ |
| C=O | 5 | 1113 | $1.8\times10^{-5}$ |
| O-H | 2 | 1438 | $7.2\times10^{-2}$ |

Table 6.2: Wavelengths and intensities of important vibrational overtones [56]

4. Glass transition temperature ($T_g$): The operating range of the add-drop filter under consideration is between 25$^o$C-125$^o$C. So, the chosen polymer must have its $T_g$ outside the operating range. This is because the $T_g$ is a second-order transition which is accompanied by a step increase in the volume expansion coefficient of the polymer. The discrete increase in the volume expansion coefficient translates as an increase in the TO coefficient (Eq.(5.8)) thereby changing the effective TO response of the silicon add-drop filter.

5. Degradation temperature ($T_{degradation}$): Degradation or decomposition temperature of a polymer refers to bond scission at high temperatures. This decomposition occurs at a lower temperature in the presence of oxygen, due to the oxidation of C-H bonds and $CO_2$ evolution. Integration of athermal add-drop filters in the BEOL interconnect stack requires that the chosen polymer is compatible with the CMOS BEOL process flow [86]. This means that the polymer should be stable atleast until 400°C which is the temperature associated with the metallization and annealing processes in the BEOL flow.

6. Processability: The key factors that have to be accounted for include strong adhesion on the substrate, highly conformal coating, good thickness control, low moisture absorption, high resistance to photo-oxidation and ease of patternability. Also, it is important to consider the ability of muti-layer stacking on polymer cladded devices when dealing with the athermal add-drop filter integration in the BEOL interconnect stack. This requires an associated stability to plasma and UV exposure in addition to the aforementioned factors.

It is important to realize that a given polymer might not have all the desired optical properties stated above due to their contrasting requirements. For instance, a large TO coefficient requires that the polymer has a large volume expansion coefficient that is related to a relatively low bond stiffness and a large bond vibration. This can translate into a low degradation temperature of the polymer thereby not meeting the desired thermal stability till 400°C. So for simplictiy, this chapter focuses on the optimization of 2 key optical properties, namely, the refractive index and the TO cofficient. In the next chapter, we address other factors like processability and thermal stability of polymer and integration of polymer cladded devices in a multi-layer stack. We choose a fluorinated acrylate based polymer for our investigation due to their low optical loss [56] and the encouraging results we had seen with a polymer from the same family provided to us by Enablence (EP). We choose initiated chemical vapor deposition (iCVD) as the desired deposition technique due to conformal coating, good thickness control and ease of tailoring the cross-linking associated with the process. In particular, two silicon-polymer composite structures, poly(perfluorodecyl acrylate) (pPFDA) and poly(perfluorodecyl acrylate-co-divinyl benzene) p(PFDA-*co*-DVB), are analyzed as candidates for thermal compensation.

## 6.3 Initiated chemical vapor deposition

Initiated chemical vapor deposition (iCVD) is a solvent free, low energy and one-step method to deposit polymers [87–89]. This deposition method involves the vapor-phase delivery of an initiator and a monomer into a vacuum chamber (Pressure: 0.1-1 Torr), where the initiator is thermally activated using filament wires heated between 200$^o$C - 400$^o$C (Fig. (6-1)). This is followed by diffusion and adsorption of the initiator radicals and the monomer on the substrate that is maintained at a lower temperature (15$^o$C - 40$^o$C). Polymerization of the monomer occurs on the substrate surface via classical free radical polymerization at rates as high as 375 nm/min [88].

The controlling parameters typically include the monomer choice, saturated vapor pressure of the monomer ($P_{sat}$), the monomer gas pressure ($P_M$),and the substrate temperature ($T_{substrate}$) [88]. For instance, a monomer with a longer pendant alkyl chain has a lower $P_{sat}$ for a given $T_{substrate}$. So, heavier the monomer, less of it resides in the vapor phase at equilibirum. In other words, for a given $P_M$, greater amount of heavier monomer gets adsorbed on the substrate. The ratio of $P_M/P_{sat}$ can be used as a good indicator of adsorbed monomer concentration on the surface as governed by the Brunauer-Emmett-Teller (BET) equation [90]. In fact, at low $P_M/P_{sat}$ , there is a linear relationship governing the monomer concentration to $P_M/P_{sat}$ (Henry's law limit) [91, 92]. An equation relating the total adsorbed volume ($V_{ad}$) to monolayer adsorbed volume ($V_{ml}$), $P_M/P_{sat}$ , the heat of desorption ($\Delta H_{des}$) and the heat of

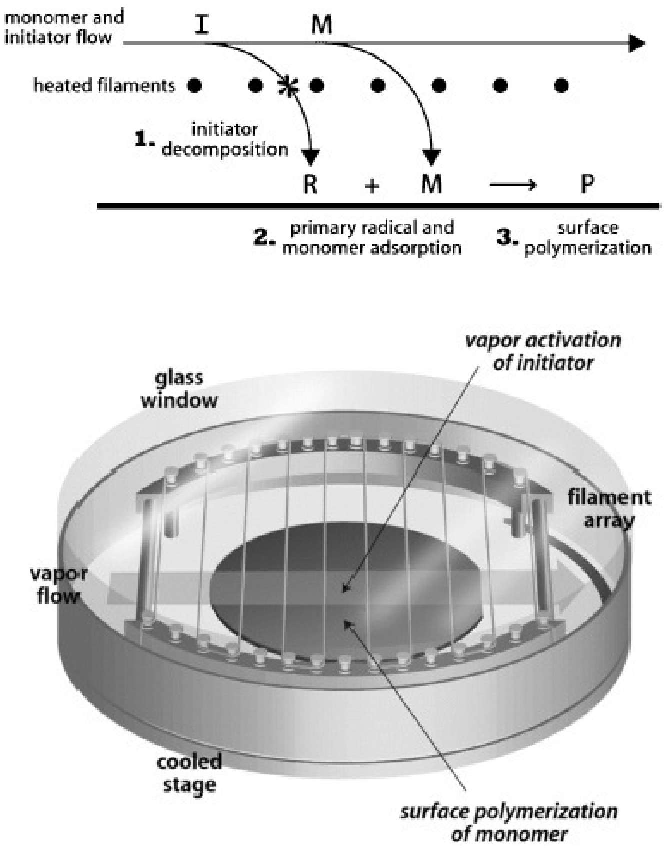

Figure 6-1: Reaction mechanism of iCVD polymerization and the reactor setup [88].

vaporization ($\Delta H_{vap}$) can be derived as follows [88, 93]:

$$\begin{aligned} V_{ad} &= \frac{V_{ml}c(P_M/P_{sat})}{(1-P_M/P_{sat})[1-(1-c)(P_M/P_{sat})]} \\ c &\approx \exp[(\Delta H_{des} - \Delta H_{vap})/(RT)] \\ [M] &\propto V_{ad}|_{P_M/P_{sat}\to 0} = V_{ml}c(P_M/P_{sat}) \\ P_{sat} &= A\ \exp[-\Delta H_{vap}/(RT)] \end{aligned} \tag{6.1}$$

where [M] is the monomer surface concentration. Lau and Gleason have shown [88] that the iCVD deposition rate varies quadratically with [M] thereby arriving at an Arrhenius dependence between the rate and the substrate temperature (Eq. (6.2)). Hence, the iCVD kinetics is adsorption limited where the rate increases with increasing monomer surface concentration that can be achieved by either decreasing the $T_{substrate}$ or increasing the $P_M/P_{sat}$. Further, the effect of filament temperature on the reaction kinetics is minimal though an increased filament temperature is reported to increase the iCVD rate.

$$rate \propto [M]^2 \propto \exp[2\Delta H_{des}/(RT)] \tag{6.2}$$

### 6.3.1 Experimental details

Two polymer choices, 1) Poly(1H,1H,2H,2H-perfluorodecylacrylate) (pPFDA, $CH_2{=}CHCOOCH_2CH_2(CF_2)_7\text{-}CF_3$) and 2) co-polymer of PFDA and DVB (p(PFDA-*co*-DVB) are deposited on blank Si wafers using the iCVD technique with t-butyl peroxide (TBPO) as the initiator. Different flow rates of DVB (0.15 sccm, 0.3 sccm and 0.6 sccm) are used for a given flow rate of PFDA (0.3 sccm), TBPO (0.3 sccm) and Argon (3 sccm) to study the addition of DVB on the polymer composition. Differing flow rates ($F_M$) of a given monomer results in a different $P_M$ since $P_M = (F_M/F_{Total})P$ (where $F_{Total} = F_M + F_{Initiator} + F_{Argon}$ and $P = 1.0\ Torr$). Hence, the differing flow rates of DVB translate as differing DVB compositions (Eq. (6.1))in the film resulting in different extents of cross-linking. Given the same thin film thickness in the samples, FTIR spectrum (Fig. (6-2) reveals a significant reduction in the C-F (1149, 1203, 1232 $cm^{-1}$) and the C=O (1738 $cm^{-1}$) [87] bond densities in the co-polymer (p(PFDA-*co*-DVB)) compared to the homo-polymer (pPFDA) as a consequence of the incorporation of DVB.

The thermal degradation of the acrylate family is mainly due to the C=O bond dissociation and occurs around 250$^o$C - 300$^o$C [94–96]. However, in section 7, we show that at low temperatures, the high density plasma chemical vapor deposition of dielectrics can be carried out to hermetically seal such a polymer and make it compatible for multi-layer stacking. Also, Ma et. al [56] have discussed the processability and various patterning techniques of halogenated acrylates in detail thereby encouraging the adoption of this class of polymers for our study. Recently, the iCVD based patterning technique of pPFDA on curved substrates has also been explored [97]. It

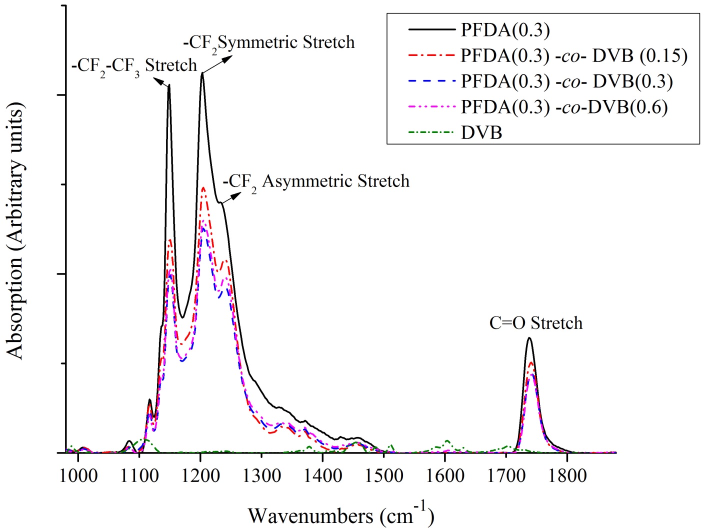

Figure 6-2: Characteristic FTIR bands of pPFDA correspond to -$CF_2$-$CF_3$ end group at 1149 $cm^{-1}$, symmetric stretching of -$CF_2$ moiety at 1203 $cm^{-1}$, asymmetric stretching of -$CF_2$ moiety at 1232 $cm^{-1}$, and C=O stretching at 1738 $cm^{-1}$. The addition of DVB as a cross- linker brings down the intensity of these characteristic bands in the copolymer.

is important to note that the patterning associated edge roughness doesn't affect the loss performance of the device as the polymer is used as an over-cladding where its edge does not interact with the optical mode.

## 6.4 Co-polymer performance: Refractive index and TO properties

The addition of DVB affects the optical properties of the polymer in two ways. Firstly, the addition of an aromatic group improves the packing density thereby increasing the refractive index. Secondly, the decrease in C-F bond density has an associated increase in "$x$" (Eq. (5.6)) and a corresponding increase in $n$. This is supported by the index measurements at 633 nm where n(pPFDA): 1.33, n(pDVB): 1.57 and n(p(PFDA-*co*-DVB)): 1.38.

The TO coefficients of the polymers can be measured by using them as a top cladding for an amorphous Si (a-Si) racetrack resonator. The transmission spectrum of the resonator at various temperatures reveals the resonance peak shift with temperature which can be related to the effective TO coefficient of the device (Eq. (5.11)). The TO coefficient of the polymer can be deduced from the effective TO coefficient of the device as the TO coefficients of the a-Si core ($2.3\times10^{-4}\ K^{-1}$) and the $SiO_2$ under-cladding ($1\times10^{-5}\ K^{-1}$) are known.

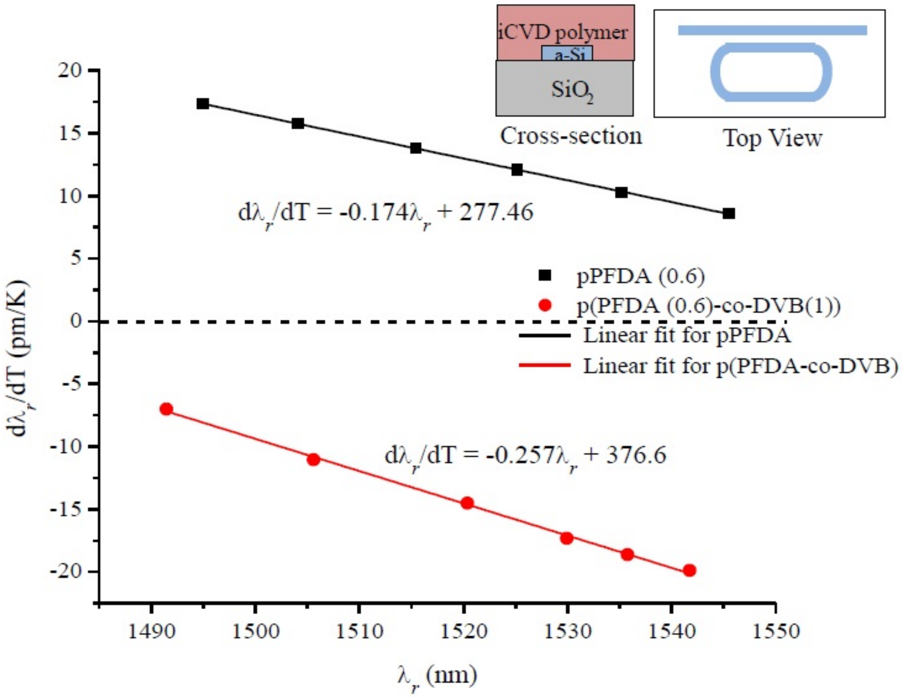

Figure 6-3: The resonance peak shift with temperature is positive for the pPFDA top cladding while negative for the p(PFDA-*co*-DVB) top cladding suggesting that the TO magnitude of copolymer ($-3.1\times10^{-4}\ K^{-1}$) is higher than that of pPFDA ($-2.1\times10^{-4}\ K^{-1}$). The inset shows the schematic of a-Si resonator whose TM transmission is measured at various temperatures for 2 different iCVD polymer top cladding choices: pPFDA ($F_{PFDA}$: 0.6 sccm) and p(PFDA-*co*-DVB) ($F_{PFDA}$: 0.6 sccm, $F_{DVB}$: 1 sccm).

The TM transmission resonances corresponding to racetrack resonators (coupling length: 100 $\mu$m, coupling gap: 600 nm, ring radius: 20 $\mu$m) with a-Si core (550 nm × 205 nm), 3 $\mu$m $SiO_2$ under-cladding and 2 $\mu$m iCVD polymers (Fig. (6-3inset)) are measured between 25$^o$C-70$^o$C. The TO peak shift for PFDA ($F_{PFDA}$: 0.6 sccm) cladded devices is positive compared to that of the co-polymer ($F_{PFDA}$: 0.6 sccm, $F_{DVB}$: 1 sccm) cladded rings suggesting a significant increase in the magnitude of the

TO coefficient due to DVB addition (Fig. (6-3)). FIMMWAVE simulations suggest that PFDA has a TO coefficient of -2.1×$10^{-4}$ $K^{-1}$ while the co-polymer has a TO coefficient of -3.1×$10^{-4}$ $K^{-1}$. The increase of the TO coefficient by 1.48$x$ due to the addition of DVB can be understood from Eq. (5.8). The index increases by 1.04x on DVB addition which translates to a 1.17$x$ increase in the index dependence factor of the TO coefficient in Eq. (5.8). The remaining increase in TO coefficient can be attributed to the increased $\alpha_V$ of the co-polymer due to the addition of DVB with higher $\alpha_V$ (8.6×$10^{-4}$ $K^{-1}$ [98] to an acrylate with lower $\alpha_V$(0.5 - 0.9×$10^{-4}$ $K^{-1}$ [99]). It can also be understood by the reduction of strong C-F bonds in the co-polymer increasing its $\alpha_V$.

So, the co-polymer design space allows independent variation of the $n$ and the TO through the careful choice of cross-linkers. In this case, reduction of the C-F bond changes the $n$ of the fluorinated acrylate while a high volume expansion coefficient of the cross-linker increases the TO coefficient of the co-polymer material.

## 6.5 Impact on athermal design space due to co-polymer material choice

For a given core choice, a polymer top cladding with a higher index and a higher TO magnitude is desired for athermal application as discussed in the above section (6.2). This is because a higher index would lower the index contrast thereby ensuring greater mode expansion into the cladding. Similarly, a higher TO magnitude of the cladding would mean passive thermal compensation for a larger core dimension. For instance, assuming an a-Si core ($n$: 3.48, TO: 2.3×$10^{-4}$ $K^{-1}$) and a $SiO_2$ under-cladding ($n$: 1.46, TO: 1×$10^{-5}$ $K^{-1}$), the bending loss performance of pPFDA ($n$: 1.33, TO: -2.1×$10^{-4}$ $K^{-1}$) and p(PFDA-*co*-DVB) ($n$: 1.38, TO: -3.1×$10^{-4}$ $K^{-1}$) cladded devices can be compared for athermal design for a TM mode choice. The pPFDA has a lower TO coefficient than p(PFDA-*co*-DVB). Hence, thermal compensation of a-Si core occurs at a much lower confinement factor for the homo-polymer cladding compared to the co-polymer cladding. FIMMWAVE simulations indicate that pPFDA cladded devices have an $n_{eff}$ of 1.6 for an athermal core dimension of 550 nm × 190 nm, while p(PFDA-*co*-DVB) cladded devices have an $n_{eff}$ of 1.78 for a core dimension of 550 nm × 212 nm. The higher $n_{eff}$ of a p(PFDA-*co*-DVB) clad device at athermal condition results in a tighter confinement for a given bending radius resulting in a higher bending Q (Fig. (6-4)). Hence, for a bending Q of $10^4$ (minimum desired bending Q for a good filter performance), FIMMWAVE simulations indicate that co-polymer clad device has a bending radius of 5 $\mu$m (Fig. (6-4)) and an FSR of 20 nm which is twice the FSR of the p(PFDA) clad device (10 nm for bending radius of 12.5 $\mu$m). In a Si WDM architecture with a given channel spacing, a 100% improvement in FSR and footprint (Fig. (6-4)) performance results in twice the number of channels thereby doubling the bandwidth capacity.

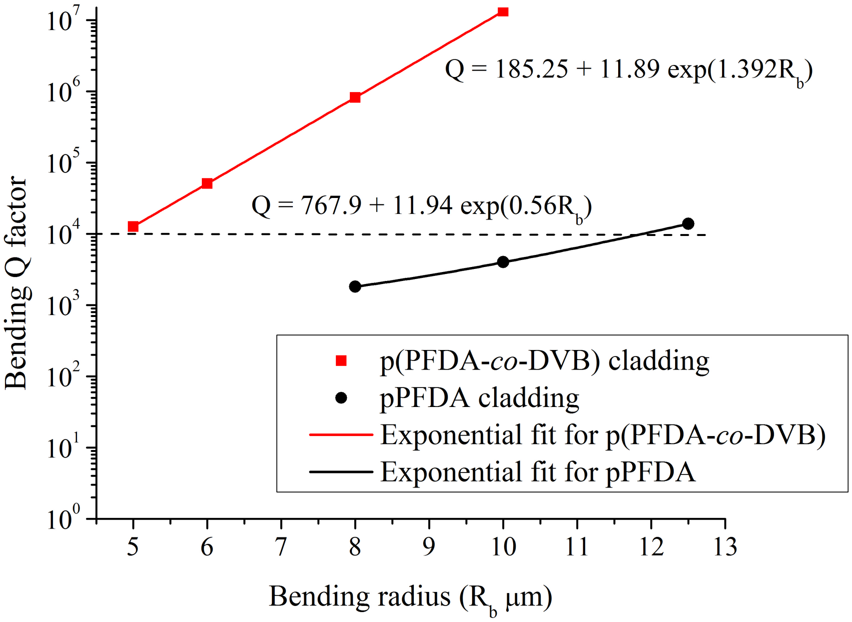

Figure 6-4: Bending loss performance of both the cladding choices are compared by plotting the simulated bending Q for various bending radii. For a bending Q of $10^4$, the co-polymer clad device has a bending radius of 5 $\mu$m while that of p(PFDA) clad device is 12.5 $\mu$m

## 6.6 iCVD vs. Spin on

Table 6.3 compares the key parameters that were discussed in section (6.2) for the iCVD polymer choice and the hyperlinked fluorinated spin on polymer provided by Enablence (EP).

| Parameters | Spin on | iCVD |
|---|---|---|
| Polymer material | EP | p(PFDA)/p(PFDA)-*co*-DVB |
| Refractive index ($n$) | 1.38 | 1.33 - 1.38 |
| TO coeff ($\times 10^{-4} K^{-1}$) | $-2.65$ | $-2.1$ - $-3.1$ |
| Optical loss (dB/cm) | < 0.5 | < 0.5 |
| $T_g (^oC)$ | < 20 | around 100 |
| $T_{degradation}$ in $N_2 (^oC)$ | 375 | 250-300 |
| Thickness control | difficult below 200 nm | Can deposit as low as 20 nm |
| Coating type | Non-conformal for high aspect ratio | Conformal |

Table 6.3: Comparing key optical parameters associated with the iCVD and the Spin on polymer

Until now, the working prototype of a passive athermal device (chapter 5) and the ability to independently tailor the relevant optical properties, $n$ and TO, of a co-polymer material (current chapter) have been established. With this toolkit, the next chapter focuses on integration of polymer cladded devices in the BEOL interconnect stack. This requires the hermetic sealing of polymer cladded devices to ensure robust performance and enable multi-layer stacking. Eventhough, the iCVD co-polymer provides a superior TO performance and has an inherent advantage of conformal coating and thickness control over EP, the higher degradation temperature of EP proves beneficial while considering dielectric deposition (which conventionally occurs around $350^oC$) on polymer cladding (Table (6.3)). Further, the absence of any glass transition in the EP above room temperature as opposed to the iCVD polymer, rules out any undesired variations in the TO coefficient while considering the temperatures associated with operating range of the filters ($25^o$C-$125^o$C) and the dielectric deposition. Hence, EP is chosen as the cladding choice while investigating the effects of hermetic sealing on the athermal devices in the next chapter.

# Chapter 7

# Hermetic sealing of polymer clad rings

Back-end compatibility requires multi-layer stacking including the deposition of patterned structures on top of the polymer cladding. This includes the stable operation of a polymer under following conditions:

1. UV exposure: The exposure to UV radiation from the plasma or lithography steps during device stacking can result in undesired photo-oxidation of the underlying polymer layer.

2. High temperature: The CMOS BEOL process flow involves metallization and annealing steps at temperatures between $400^o$C - $450^o$C [86] and the chosen polymer should be stable at such high temperatures.

3. Plasma exposure: The deposition of patterned structures requires the polymer to be stable to plasma exposure.

An a-Si racetrack ring resonator with EP over-cladding (Fig. (7-1)) deposited as explained in section 4 is used as the prototype to investigate the listed stability issues.

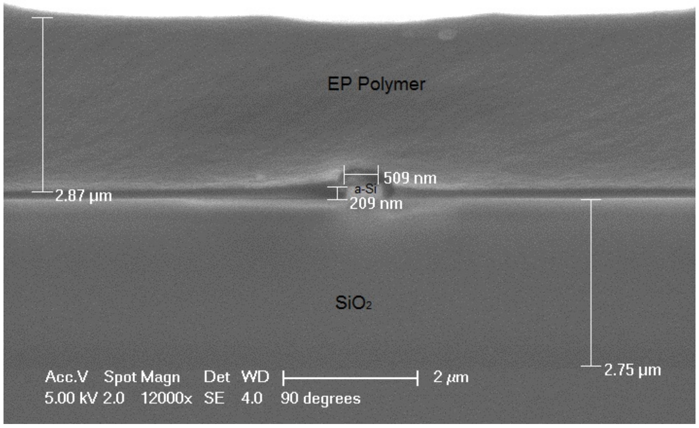

Figure 7-1: Cross-sectional SEM of the device shows 509 nm × 209 nm a-Si core with a 2.75 $\mu$m $SiO_2$ under-cladding and a 2.87 $\mu$m EP polymer over-clad.

## 7.1 UV stability

UV induced variation in the refractive index of a polymer always has an associated saturation behavior. So, the UV stability of a polymer can be ensured by pre-exposing it to UV levels beyond, which no measurable change in the polymer properties occurs. The EP polymer clad is UV cured by exposing it to a 5 mW/cm$^2$ (Energy dose: 6000 mJ/cm$^2$) from a short arc mercury lamp for 20 minutes. The samples are further baked at 150$^o$C under vacuum for 4 hours to enhance the cross-linking in the cured polymer. This process stabilizes the polymer for further UV exposure during lithography and plasma deposition steps. The FTIR spectra of the cured polymer film exposed to a 254 nm UV handheld lamp with a power flux of 2.2 mW/cm$^2$ showed no significant change in the bond chemistry of the polymer, thereby establishing its chemical stability (upto 7920 mJ/cm$^2$ of UV dose). The amorphous network-property correlation, that relates the bond chemistry to the refractive index, supports the stable optical performance of the polymer cladding under UV exposure. In other words, the TO performance of an athermal ring remains the same even after UV exposure. This is verified by exposing the athermal devices to 9.5 mJ/cm$^2$ of UV radiation (365-405 nm). The TO performance is measured by noting the transmission spectrum for every 5$^o$C of an athermal ring heated from 25$^o$C-70$^o$C.The observed scatter in the TO experimental values (around 1 pm/K) of an athermal ring exposed to UV radiation is within expected limits (±5 pm/K) due to the thickness variations (±6nm) associated with a-Si deposition (Fig. (7-2)).

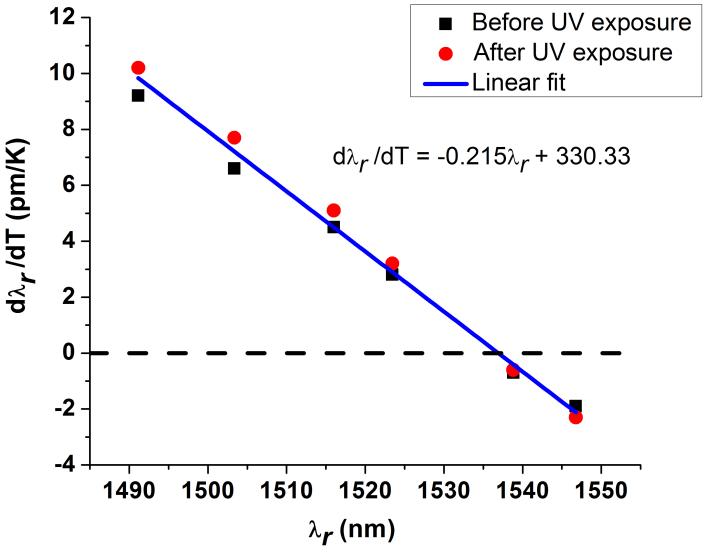

Figure 7-2: Experimental data suggests that UV exposure ($\lambda$: 365-405 nm, Dose : 9.5 mJ/cm$^2$) has minimal effect on the TO response of an athermal ring.

## 7.2 Thermal stability

The stable performance over the working temperature range, 25$^o$C - 125$^o$C, is ensured by baking the polymer clad device in vacuum at 150$^o$C for 4 hours. However, back-end CMOS compatibility of these athermal rings might require it to withstand temperatures as high as 400$^o$C associated with the copper metallization and the final forming gas annealing steps [86]. The Thermogravimetric analysis (TGA) of the polymer in a dry $N_2$ atmosphere shows the weight loss around 375$^o$C at a heating rate of 10$^o$C/min (Fig. (7-3)). However, the onset of decomposition may change with the heating rate. It is important to note that cooling to the operating temperature after the onset of decomposition can result in the loss of polymer functionalities for an athermal application. Further, there are no structural transitions in the polymer upto 300$^o$C. Hence, the multi-layer deposition processes on athermal rings carried out at less than 300$^o$C in a non-oxidizing atmosphere would ensure a safe processing condition that prevents any property changes of the polymer as long as equilibrium cooling of the polymer layer is ensured.

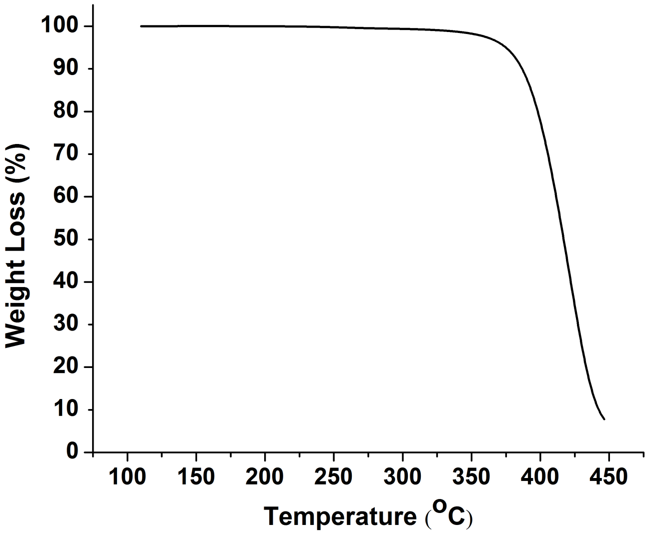

Figure 7-3: TGA measurement of the polymer sample in $N_2$ atmosphere reveals weight loss above 350$^o$C at a heating rate of 10$^o$C/min.

## 7.3 Plasma stability

The deposition of discrete devices on athermal rings demands stability to plasma exposure. However, the SEM and TO performance of rings (Fig. (7-4)) exposed to Argon plasma at 130$^o$C suggests etching of the polymer over-cladding. The change in the absolute TO peak shifts indicate the increase in the effective TO of the system after plasma exposure (Fig. (7-4(b))). The change in the slope value is indicative of the change in the TO contrast between the core and the cladding. In addition, different waveguide dispersion also reflects the fact that the confinement factor of the waveguide has changed after plasma exposure thereby changing its effective index. This motivates the need for a dielectric hermetic layer that prevents polymer degradation in the presence of plasma.

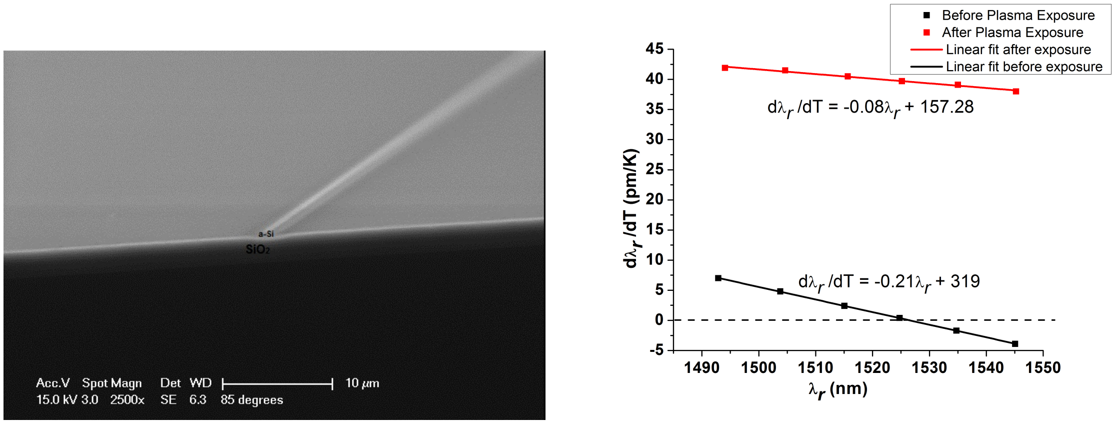

(a) (b)

Figure 7-4: (a) SEM image of the plasma exposed athermal device confirms the etching of polymer top cladding. (b) TO performance of the ring exposed to Argon plasma reveals increased TDWS values (around 40 pm/K) due to the absence of polymer.

## 7.4 High density plasma chemical vapor deposition of dielectric encapsulation

The incentive for encapsulating the polymer clad athermal rings with a thin layer of dielectric is two pronged: robust performance in an oxidizing atmosphere and to plasma exposure. Dielectrics act as oxygen diffusion barriers thereby preventing an unwanted oxidation of the underlying polymer. In addition they could act as possible etch stops during new device patterning on top of the athermal rings. However, the polymer decomposition constrains the dielectric deposition to temperatures less than 300°C in a non-oxidizing atmosphere. Conventional PECVD results in hydrogen incorporation at temperatures less than 300°C, thereby motivating the need for a low temperature deposition that might result in lesser hydrogen incorporation.

The low temperature deposition of dielectrics by plasma enhanced chemical vapor deposition calls for an enhancement of plasma excitation efficiency for precursor activation and a high current, low-energy ion assist. The high density plasma chem-

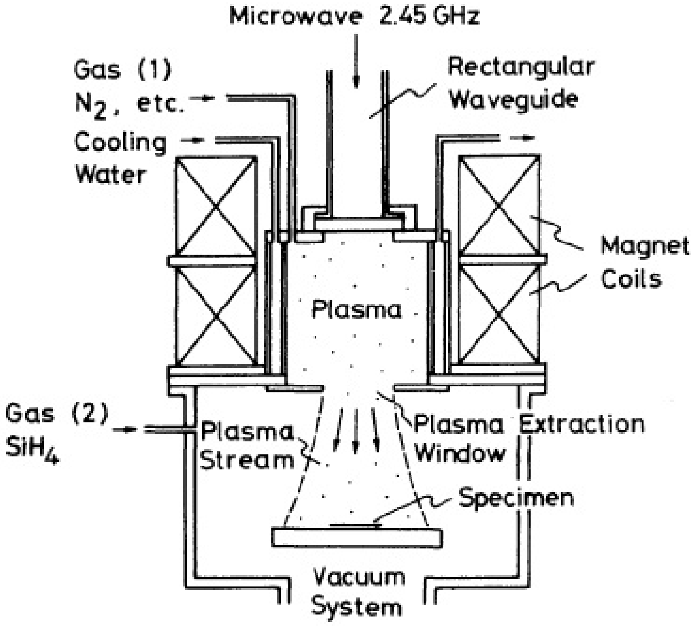

Figure 7-5: A schematic of ECR plasma deposition apparatus [100]

ical vapor deposition, using electron cyclotron resonance (ECR) as the high density plasma source, of high quality $SiN_x$ and $SiO_2$ films with low hydrogen content has been demonstrated at low temperatures [100–103]. In such a deposition technique (Fig. (7-5)), microwave power (frequency: 2.45 GHz) is introduced into the plasma chamber by a rectangular waveguide and through a window made of fused quartz plate. The plasma chamber dimensions in Fig. (7-5) correspond to the $TE_{113}$ resonance of the cavity. Magnetic coils are arranged around the periphery for ECR plasma excitation. The plasma is generated by coupling the movement of electrons in a static magnetic field with a microwave power source. The cyclotron frequency can be controlled by the magnetic coils. When the microwave frequency equals the electron cyclotron frequency, the resonance results in efficient absorption of microwave power by the electrons thereby resulting in the ionization of the precursor gas. Thus highly activated plasma can be generated at low gas pressures ($10^{-3}$-$10^{-5}$ Torr). The plasma extraction is done through a divergent magnetic field method where the intensity of the field is weakened gradually between the plasma and the specimen. High energy electrons in the ECR plasma are drawn towards the specimen due to the magnetic field gradient thereby bringing about a negative potential at the surface of the specimen (which is electrically isolated from the plasma chamber). Therefore, a static electric field is generated along the plasma stream which accelerates the positive ions towards the specimen and decelerates the electrons, thereby resulting in an effective ion transport and ion bombardment on the specimen.

The ECR plasma is an electrodeless, non-collisional plasma that does not require a high-voltage sheath with high ion energy. The process operates at low pressure, low electron and ion-energy with a high degree of ionization [104]. A separate power source is used to bias the wafer in order to control the ion bombardment on the surface. The decoupling of the plasma density and the ion energy ensures deposition of high density film at low temperatures, low power, and low ion energies. The ECR-PECVD combines PECVD deposition with bias sputtering resulting in the simultaneous sputter etching and the deposition on the wafer resulting in dense films with low -OH and -NH bond density [102]. Furthermore, the plasma damage to the wafer is low as the substrate is remote from the plasma.

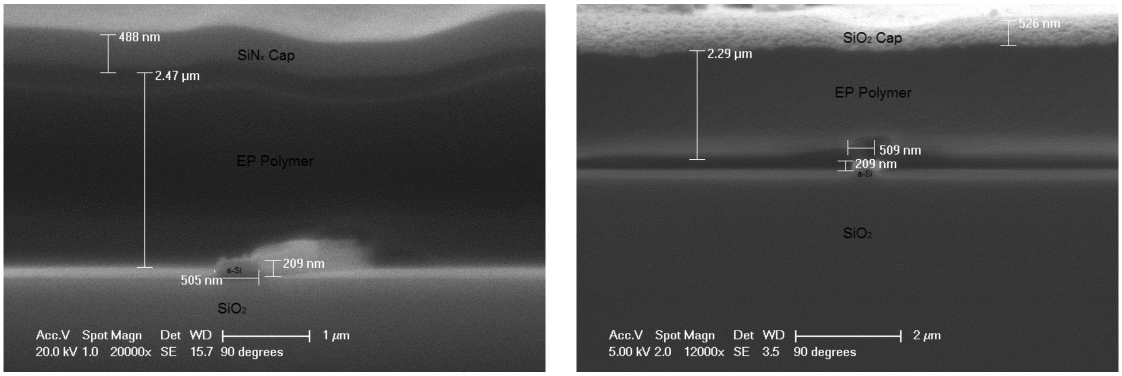

(a) (b)

Figure 7-6: (a) SEM confirms the successful deposition of dielectrics on the polymer cladding. Cross-sectional SEM of 505 nm×209 nm a-Si with 3 $\mu$m $SiO_2$ under-clad, 2.47 $\mu$m EP polymer over-clad encapsulated with a 488 nm $SiN_x$. (b) Cross-sectional SEM of 509 nm × 209 nm a-Si with 3 $\mu$m $SiO_2$ under-clad, 2.29 $\mu$m EP polymer over-clad encapsulated with a 526 nm $SiO_2$ cap.

Two choices of dielectrics, namely $SiN_x$ and $SiO_2$, are considered as possible encapsulates. 500 nm of both the dielectrics are successfully deposited on the polymer layer using the ECR-HDPCVD (Fig. (7-6)) technique using the conditions listed in Table (7.1). The deposition rate can be increased by increasing the microwave power [100]. The hydrogen content in the film can be reduced by optimizing the flow rate [101] or by increasing the ion flux that can etch away the hydrogen [102].

| **Deposition conditions** | **$SiO_2$** | **$SiN_x$** |
|---|---|---|
| Substrate temperature ($^o$C) | 130 | 130 |
| Ar flow rate(sccm) | 10 | 20 |
| $O_2$ flow rate (sccm) | 20 | - |
| $N_2$ flow rate (sccm) | - | 11.6 |
| 3% $SiH_4$/ Ar flow rate(sccm) | 100 | 110 |
| Pressure (mTorr) | 20 | 20 |
| Microwave Power (W) | 300 | 265 |
| Deposition rate (nm/min) | 20.1 | 16.6 |
| Refractive index | 1.47 | 1.95 |
| Stress (MPa) | $-2.3$ | 37 |
| Uniformity (4 inch wafer, 1 sigma) | 5% | 4.5% |

Table 7.1: HDPCVD conditions for $SiO_2$ and $SiN_x$ depositions on the polymer clad devices.

## 7.5 Performance of dielectric caps

It is important to ensure that the presence of dielectric caps does not affect the TO performance of the athermal rings. The optical mode is fully confined within the polymer cladding as its thickness is greater than 2 $\mu$m (Fig. (7-6)). The invariance of the polymer optical properties and the athermal performance is easily verified through the TO performance of the capped devices (Fig. (7-7)). The deposited a-Si films have a thickness uniformity around 3% which results in an uncertainty in its thickness value of around 6 nm. FIMMWAVE simulations indicate that a 1 nm change in the thickness of these rings could shift its TO peak shift by 1 pm/K, given the sensitivity of the TM mode response to the thickness variation. This results in a possible variation of 5 pm/K in the TO peak shift of a resonator for a given wavelength. The TO response of the encapsulated rings falls within this variable limit thereby making them suitable for multi-layer stacking.

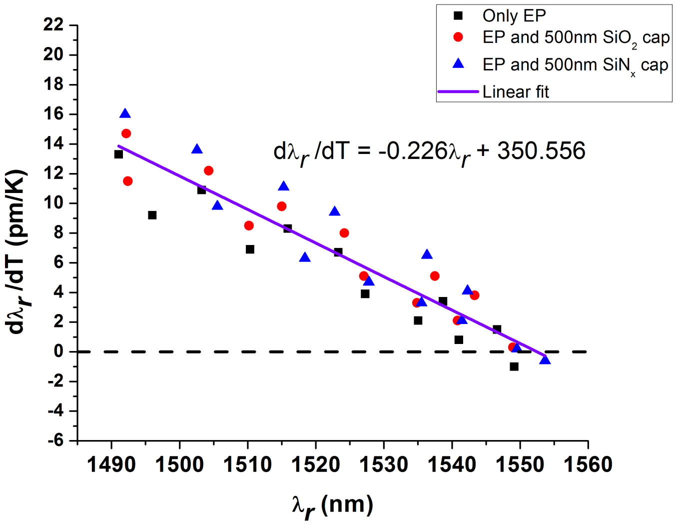

Figure 7-7: The TO performance does not change significantly after the dielectric ($SiO_2/SiN_x$) deposition on the polymer. The scatter in experimental TO peak shift values are within the expected variation (±5 pm/K) due to the 3% thickness non-uniformity during the deposition of 205 nm thick a-Si film.

Finally, the hermetic sealing improves the mechanical stability of the cladding layer. This is obviated by the improved Young's modulus of the polymer-dielectric bi-layer stack: 1. Polymer+$SiO_2$: 3.4 GPa, 2. Polymer+$SiN_x$: 4 GPa, as compared to that of the polymer (84.4 MPa).

## 7.6 Concluding remarks

This chapter has addressed a key aspect of the BEOL integration of polymer clad devices in an electronic-photonic architecture: multi-layer stacking. This calls for a stable operation of polymer under exposure to high operating temperatures (the BEOL annealing cycles around 400-450$^o$C), plasma (Argon is used for demonstration in this chapter) and UV radiation (BEOL lithography dose levels can be upto 50 mJ/cm$^2$). Eventhough, UV stability can be achieved by UV curing to the saturation levels (6000 mJ/cm$^2$ for EP) followed by annealing of the polymer, the plasma and chemical stability calls for the hermetic sealing of the polymer. Further, the degradation temperature of the polymer calls for a low temperature HDPCVD technique for dielectric deposition. This chapter demonstrates the successful deposition of dielectric encapsulation on the polymer clad devices. This enables multi-layer stacking, prevents polymer photo-oxidation and improves the mechanical properties of the bi-layer stack while retaining the athermal behavior.

The hermetically sealed, athermal rings still suffer from resonance variation associated with the fabrication tolerance (Fig. (7-7)). The ability to trim the resonance post-fabrication is covered in the next chapter.

# Chapter 8

# Post-Fabrication trimming of passive athermal rings

The previous chapter focused on the integration of a passive athermal a-Si device as part of a multi-layer stack. Another aspect of the process integration involves addressing the fabrication tolerance of these devices. A 1 nm increase in the thickness of a a-Si waveguide red-shifts the TM resonance peak by 1 nm and increases the TO peak shift by 1 pm/K. Hence, the shift in the filter response of an athermal ring due to fabrication variations needs to be tuned back to its desired value. Athermal resonators rule out the possibility of thermal tuning thereby requiring an alternative approach. The photo-sensitivity of $As_2S_3$ chalcogenide glasses has been exploited to counteract the fabrication tolerances and reconfigure the response of photonic waveguides [105–107].

In this chapter, we propose a multi-layer solution for a photo-trimmable athermal ring resonator. The prototype design rule requires the encapsulation of the a-Si core with a thin layer of $As_2S_3$ before the polymer top cladding deposition. In a Si based WDM system with a 20 GHz channel spacing, the maximum tolerable TO wavelength shift is around 1.3 pm/K over an operating range of $25^oC$-$125^oC$. In addition, the trimming range of a filter in such a system is desired to be less than 5 GHz to avoid loss of the neighboring channel. This chapter demonstrates a working prototype that satisfies both the aforementioned constrains.

## 8.1 Prototype of a photo-trimmable athermal silicon resonator

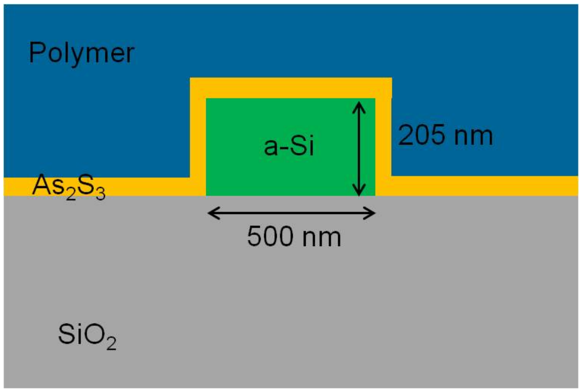

Figure 8-1: Cross-section of a photo-trimmable athermal a-Si resonator. The polymer cladding provides passive thermal compensation while $As_2S_3$ provides visible light sensitivity for post-fabrication trimming.

As explained in section 4, a-Si racetrack rings with a cross-section (500 nm × 205 nm) corresponding to the single mode TM operation were fabricated. 50 nm of $As_2S_3$ was then thermally evaporated [108] on top of the devices. Two different polymers were chosen for the top cladding to study the effect of annealing on the photo-sensitivity of $As_2S_3$: 1. SU8 with $n(\lambda = 1550nm) = 1.58$ and TO $= -1.1\times10^{-4}$ $K^{-1}$ was the first polymer. Rings with SU8 cladding were not subject to annealing. 2. EP polymer with $n(\lambda = 1550nm) = 1.38$ and TO $= -2.65\times10^{-4}$ $K^{-1}$ was the second cladding choice and was spin coated at Enablence Inc. The EP polymer clad devices were further UV cured for 20 minutes using a 5 mW/cm$^2$ short arc mercury lamp. The samples were subsequently baked in vacuum at 150$^o$C for 4 hours to stabilize the polymer properties.

In both the cases, the device cross-sections (Fig. (8-1)) have been designed to ensure that the fundamental TM mode expands through the $As_2S_3$ layer into the polymer cladding in such a way that the effective index behavior of the device is properly weighted over the indices of $SiO_2$ under-cladding ($n(\lambda = 1550nm) = 1.46$), a-Si core ($n(\lambda = 1550nm) = 3.48$), $As_2S_3$ ($n(\lambda = 1550nm) = 2.4$) and the polymer top cladding. Consequently, the effective TO behavior of the device is determined by the optical mode contained in each of the layers: $SiO_2$ (TO coefficient $= 1 \times 10^{-5}$ $K^{-1}$), a-Si (TO coefficient $= 2.3 \times 10^{-4}$ $K^{-1}$), $As_2S_3$(TO coefficient $= 4 \times 10^{-5}$ $K^{-1}$) and polymer.

## 8.2 Prototype performance: Trimming and thermo-optic measurements

### 8.2.1 SU8 clad devices

The TO coefficient ($-1.1 \times 10^{-4}$ $K^{-1}$) of SU8 is not sufficient to compensate for the a-Si's positive TO ($2.3 \times 10^{-4}$). So, the transmission measurements of SU8 clad a-Si racetrack rings; with a radius of 20 $\mu$m, coupling length of 100 $\mu$m between the bus and the ring and a gap of 600 nm; at various temperatures reveal positive TO shifts (Fig. (8-2)) for the considered cross-section (inset of Fig. (8-2)).

Further, visible light radiation (450-650 nm) from a halogen lamp, with an intensity of 10 mW/cm$^2$, was coupled to an optical fiber with a mode field diameter of 30 $\mu$m and then placed on top of the chip to selectively expose the resonator. The visible light sensitivity of $As_2S_3$ is reflected in its refractive index variation which changes the effective index and the resonance of the a-Si resonator. SU8 clad devices were not subjected to any annealing cycle and their photo-trimming performance corresponds to the behavior of as-deposited, unannealed 50 nm thick $As_2S_3$ films. The refractive index of $As_2S_3$ increases during the first 30 minutes of exposure followed by a decrease of the index during the next 90 minutes of exposure (Fig. (8-3)). This establishes the presence of 2 competing photo-sensitive mechanisms in as-deposited, unannealed $As_2S_3$ films. To understand the governing mechanisms, it is useful to measure the photo-sensitivity of the annealed $As_2S_3$ films that have an EP top-cladding.

### 8.2.2 EP clad devices

As described above, the EP clad devices (inset of Fig. (8-4)) that had been baked at 150$^o$C for 4 hours serve 2 purposes: 1. The higher TO coefficient of the EP compared

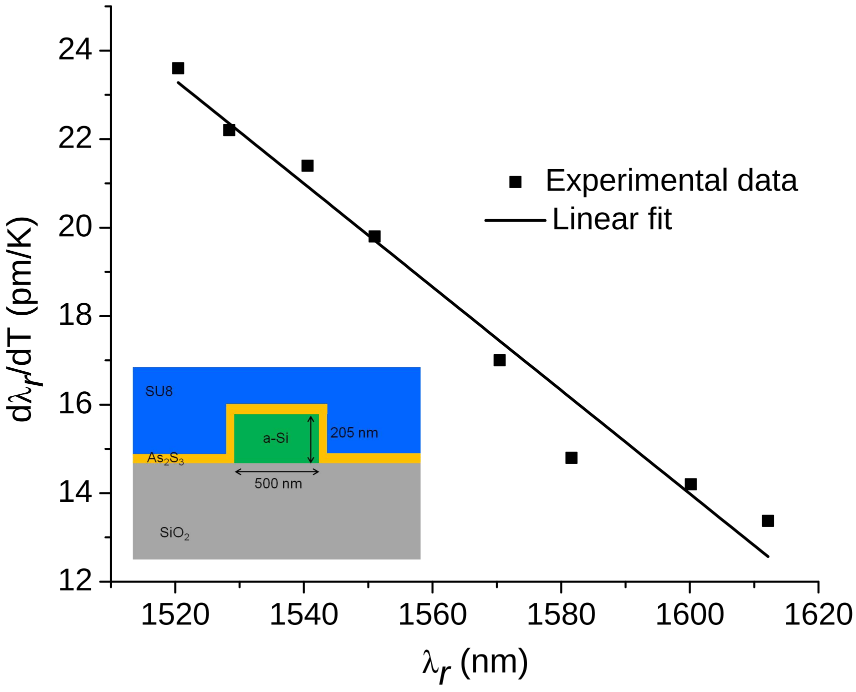

Figure 8-2: The TO performance of SU8 clad a-Si devices shows positive shifts over the measured wavelength spectrum due to the insufficient TO coefficient of SU8.

to the SU8 proves sufficient to achieve athermal operation of a-Si resonator of the fabricated cross-section. 2. The influence of annealing on the photo-sensitivity of the 50 nm thick $As_2S_3$ film can be investigated. The prototype (inset of Fig. (8-4)) with a bending radius of 20 $\mu$m, coupling length of 100 $\mu$m between the bus waveguide and the resonator, and a gap of 600 nm in the coupling section was measured.

The photo-sensitiviy of annealed $As_2S_3$ results in a blue-shift of resonance across 1 FSR (2.09 nm) after 245 minutes of exposure to visible light. A total wavelength shift of about 10 nm (≈1.21 THz) at a trimming rate of 8.5 pm/min (≈1 GHz/min), with no evidence of saturation, is observed after 1200 minutes of exposure (Fig. (8-4)). This corresponds to a variation of about $2.36 \times 10^{-2}$ in the effective index of the waveguide and 0.13 in the refractive index of the $As_2S_3$ glass. The trimming rate can be further increased by increasing the intensity of the visible light source since the wavelength shift is linearly dependent on the trimming light intensity [105].

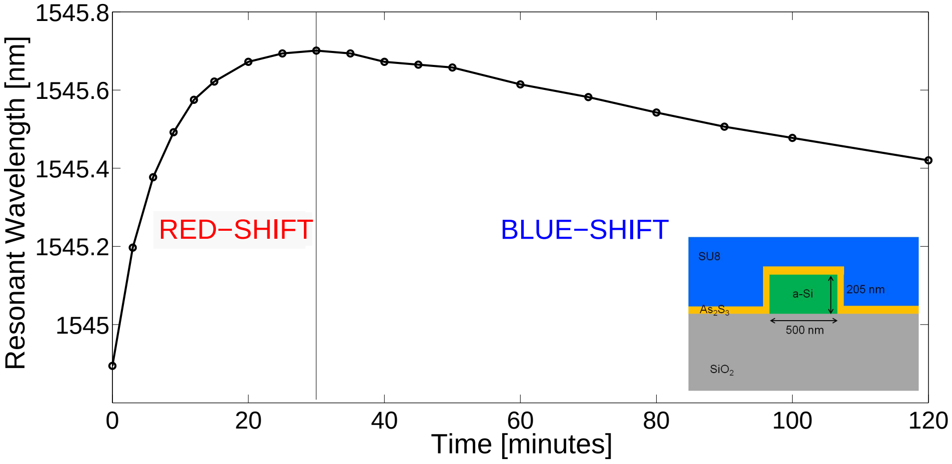

Figure 8-3: Exposure to visible light increases the refractive index of unannealed, as-deposited 50 nm thick $As_2S_3$ for the first 30 minutes and decreases its index for the next 60 minutes thereby revealing the possibility of 2 competing photo-sensitive mechanisms in $As_2S_3$.

The athermal operation of the device, corresponding to TM operation, was investigated before and after the trimming process. Pre-trimming TO measurements (black squares in Fig.(8-5)), between 20-40$^o$C, revealed no appreciable TO shift around 1570 nm. Moreover, across a bandwidth of about 50 nm, the temperature dependence of the waveguide is lower than 5 pm/K, with the variation in wavelength arising from waveguide dispersion. This temperature dependence is one order of magnitude lower than standard SOI waveguides (50 pm/K and 70 pm/K for TM and TE polarization, respectively). The post-trimming TO measurement (red circles in Fig. (8-5)) shows a blue-shift in the athermal resonance from 1570 nm to 1560 nm. The unaltered post-trimming athermal performance around 1560 nm (Fig.(8-5)) indicates nullification of the increased index-contrast at the a-Si/$As_2S_3$ interface with a corresponding decrease in the index-contrast at $As_2S_3$/EP interface. This demonstrates the possibility of tuning the "athermal point" of the waveguide across a large bandwidth (10 nm).

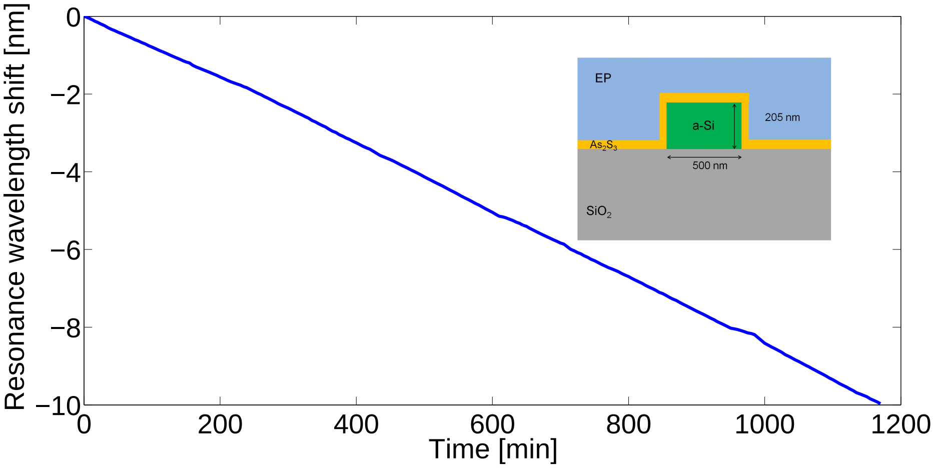

Figure 8-4: Resonance at 1570 nm, which corresponds to athermal operation, blue-shifts linearly at a rate of 8.5 pm/min (≈1 GHz/min) during the visible light exposure resulting in a total shift of 10 nm (≈1.21 THz) after 1200 minutes.

## 8.3 Discussion: Photo-sensitive mechanism of $As_2S_3$

$As_2S_3$ has a band-gap ($E_g$: 2.4 eV) that falls in the visible region of the electromagnetic spectrum. Thus, the photo-sensitivity arises due to the exposure to near-$E_g$ radiation. $As_2S_3$ exhibits no long-range order, and hence, is intrinsically metastable. Changing its structure and bonds is easy due to its inherent structural flexibility. In $As_2S_3$, the S atom has a lone pair of electrons that can undergo light-induced reactions to produce structural defects resulting in single or three-fold coordinated S species. These photo-induced changes may be reversible depending on the composition and the experimental parameters. In the context of this thesis, the focus will be on the photo-induced modifications that influence the refractive index of $As_2S_3$ and can be grouped into 2 major categories:

1. Mechanisms that increase the $n$ of $As_2S_3$: The most common photo-sensitive mechanism that can increase the index of $As_2S_3$ is photodarkening (PD). This occurs when amorphous $As_2S_3$ is illuminated with photon energy close to $E_g$ resulting in a red-shift of the absorption edge and a decrease of $E_g$. As a consequence, the refractive index increases. A number of models have been proposed

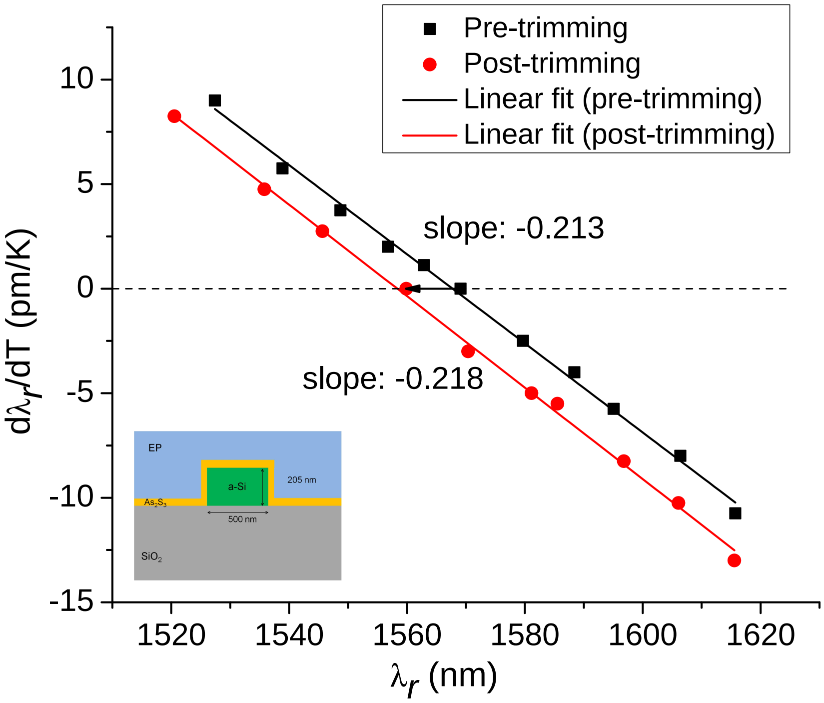

Figure 8-5: The measured TO performance, before (black square) and after (red circles) trimming in the temperature range 20-40$^{o}$C, reveals that the slope of the curve is unaltered after trimming. Further, the trimming process blue-shifts the "athermal point" from a wavelength of about 1570 nm to 1560 nm.

for PD. While some are based on bond-breaking and rearrangements, others are based on modifications to the coordination spheres with unaltered bonds. However, there exists no conclusive mechanism that is suitable for a range of chemical compositions. A detailed review of all the proposed mechanisms of PD in chronological order is presented elsewhere [109]. The most recent explanation for PD was provided by Ganjoo and Shimakawa [110, 111] where they tried addressing all the inconsistencies in the previous models. They proposed a model for the structure of $As_2S_3$ in which the $As_2S_3$ has a short-range order and is arranged into a stack of layers. They attributed the photo-sensitivity to a repulsion and slip motion (RS model) of the structural layers. During illumination, the photocreated electrons reside in the conduction band tails while the photocreated holes diffuse away through the valence band and the valence band tails leaving behind a negatively charged layer. A slip motion between the layers alters the lone pair interactions (LP-LP interaction) that reduces the band gap giving rise to the PD effect [110, 111]. According to this model, no PD occurs in very thin films as the holes cannot diffuse away from the illuminated region, thus the surface continues to maintain electrical neutrality. This seems to be consistent with the absence of PD in $As_2S_3$ films that are thinner than 50 nm as observed by Tanaka et al. [112]. However, the RS model [110, 111] does not distinguish between the PD response of stoichiometric and non-stoichiometric $As_2S_3$ as observed by Tanaka et al. [112]. In other words, PD is not observed for stoichiometric $As_2S_3$ films thinner than 50 nm, but is still observed for 50 nm thick non-stoichiometric $As_2S_3$ and the RS model does not explain this discrepancy.

Another photo-induced modification, photo-polymerization can explain the difference in the behavior of stoichiometric and non-stoichiometric $As_2S_3$. In fact, photo-polymerization has been shown as the major contribution to PD during the early stages of irradiation [113]. The evaporative deposition of a-$As_2S_3$ results in a significant concentration of $As_4S_4$, $As_2S_4$, $As_4S_5$ and $S_2$ in the film. Such structural blocks open up and polymerize on illumination or annealing. Thus, the photo-polymerization occurs through the creation of non-equilibrium holes and electrons. As described by Street [114], defect pairs $D+$ and $D-$ induced by photon absorption react with As-As bonds to form As-S bonds as the film photo-polymerizes towards the equilibrium composition. This is correlated with the red-shift of the absorption band and the refractive index. The same polymerization can be achieved by annealing thereby proving its equivalence to photo-polymerization as an approach towards stoichiometric composition. This mechanism can also explain the discrepancy between the PD response of non-stoichiometric and stoichiometric $As_2S_3$ films that are thinner than 50 nm [112].

In this thesis, the red-shift associated with the illumination of unannealed, 50 nm thick $As_2S_3$ film with SU8 over-cladding (Fig. (8-3)) seems to suggest the occurence of photo-polymerization towards the stoichiometric composition. This is further reinforced by the absence of red-shift during the exposure of annealed, 50 nm thick $As_2S_3$ film with the EP over-cladding (Fig. (8-4)). Also, the absence of PD and red-shift in the annealed, 50 nm thick $As_2S_3$ film with EP cladding is consistent with reported results [112].

2. Mechanisms that decrease the $n$ of $As_2S_3$: Photo-volume expansion (PVE) [115–120] is the most significant photo-induced modification that is associated with a decrease of $n$. Also, PD and PVE has been known to occur simultaneously and there have been many proposed mechanisms to explain this behavior [109]. However, the RS model [110,111], described earlier, is the latest effort to incorporate both the phenomena in the same model. As explained earlier, photon illumination results in negatively charged layers (due to the photocreated electrons). The RS model attributes the PVE due to Coulombic repulsion between the charged layers [110, 111].

   In this thesis, the observed blue-shift in the resonance wavelength (Fig. (8-4)), corresponding to a decrease in the index of $As_2S_3$, suggests that the dominant photosensitive mechanism in the annealed $As_2S_3$ film is PVE. The variation of trimming rates with the thickness of $As_2S_3$ seems to reinforce that PVE is the dominant photo-sensitive mechanism (Fig.(8-6)). In fact, for PVE, the variation of index ($\Delta n$) on illumination should be inversely proportional to the initial thickness ($t_{As_2S_3}$) of the $As_2S_3$ film ($\frac{\Delta n}{n} = \frac{\Delta t}{t_{As_2S_3}}$) for a given exposure dosage.

## 8.4 Concluding remarks

This chapter introduces a multi-layer approach to address the fabrication tolerance of athermal a-Si rings. This consists of a photo-sensitive $As_2S_3$ inter-clad region between the a-Si core and polymer over-clad. The thickness of $As_2S_3$ should be thick enough to influence the effective index of the device while being sufficiently

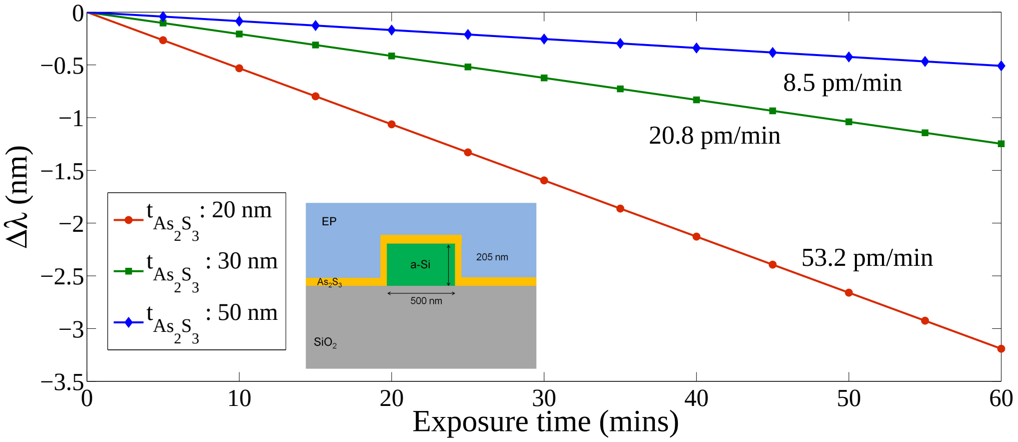

Figure 8-6: The trimming rate increases with decreasing thickness of the $As_2S_3$, thereby establishing a clear thickness dependent photo-sensitive mechanism (PVE) for the proposed device cross-section (inset). The variation of index ($\Delta n$) is inversely proportional to the initial thickness of the $As_2S_3$ film for a given exposure time.

thin to ensure the desired mode extension in the polymer region. Also, there exists an optimum $As_2S_3$ thickness (50 nm in the demonstrated prototype) where the TO performance of the device is unaltered after the resonance trimming. Additionally, visible light response of $As_2S_3$ can be altered though an annealing cycle. Finally, an initial red-shift (associated with the densification towards equilibrium stoichiometry) is seen in the trimming response for extremely thin ($<$ 50 nm) unannealed $As_2S_3$ films. However, annealed films exhibit only a blue-shift (associated with photo-volume expansion) during the post-fabrication trimming with the trimming rate increasing with decreasing thickness.

Having addressed all the crucial components of a photonic circuit in an electronic-photonic architecture; device design, material selection, multi-layer stacking and post-fabrication correction; the final step involves the system design, which is covered in the next chapter.

# Chapter 9

# System Integration: Design and trade-offs of athermal add-drop filters

This chapter considers an athermal device as a part of a photonic circuit and investigates the associated trade-offs and optimizations involved in the system design. Considering the ATAC system described earlier(section 1.2.1), hub-to hub communication occurs over a broadcast optical network, *ONet* (Fig. (9-1)). In such a scenario, where *ONet* uses WDM, each hub is assigned a unique wavelength for communication [9]. Consequently, every hub has add-drop filters to extract a definite fraction (1/N for N hubs) of every wavelength. The performance of the *ONet* is affected by the add-drop filter characteristics in a number of ways. Firstly, the number of wavelengths that can be used for communication (channel count) depends on the FSR of the add-drop filter. In other words, any add-drop filter in a hub should filter out exactly one wavelength from the set of wavelengths. Secondly, the spacing between the wavelengths (channel spacing) is determined by the Q factor of the filter. Low loss, high Q factor filters allow closer channel spacing for a given cross-talk. Finally, the power handling capacity of the add-drop filters can limit the acheivable channel bandwidth/affordable clockspeed (increases for higher power). If a single channel has to communicate with lots of receivers, high power handling capacity can also translate into large number of receivers for a given receiver sensitivity. The aggregate bandwidth density performance of the system is affected by both channel count and power handling capacity that are in turn controlled by add-drop filter parameters. This chapter tries to understand the influence of the athermal constraint on the add-drop filter performance and its effect on aggregate bandwidth density.

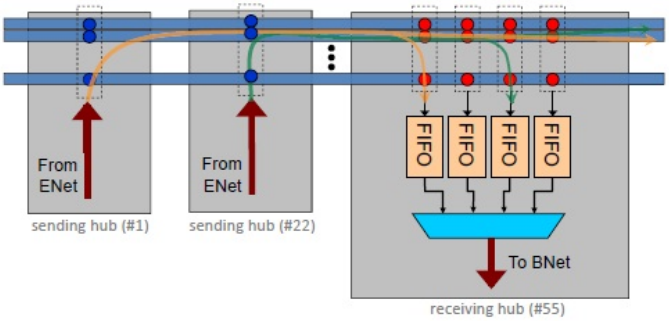

Figure 9-1: Hub-to-hub communication over the *ONet* in an ATAC architecture(reproduced from [9]).

## 9.1 Athermal constraint: Material solution

The motivation behind using Si ring resonators for WDM filter applications arises from its high-index contrast and high mode confinement. As a result, Si rings can have small bending radii resulting in a large FSR. However, the athermal operation of these rings requires reduced confinement ($\Gamma = 0.58$) for the mode to penetrate the cladding. The result is a lower effective index (1.78) waveguide with a higher radiative bending loss. This design rule leads one to inquire whether a lower-index contrast (LIC) waveguide core material with a lower TO coefficient, such as $Si_3N_4$ (TO: $4 \times 10^{-5}\ K^{-1}$), would perform as well or better for athermal WDM applications. We use the bend radius ($R_b$) as a variable in the figure of merit for the ring resonator, and calculate the $R_b$ for TM mode to be consistent with our experimental results. We start the comparison by finding the confinement factor required for athermal operation of nitride rings with the same polymer cladding used for a-Si rings. We then proceed to find the bending radius for both Si and $Si_3N_4$ for a given bending loss [121], which we fixed at 4.34 dB/cm (or 1 $cm^{-1}$).

| **Material** | $n$ | $\Gamma$ | $n_{eff}$ | $n_g$ | $R_b(\mu\text{m})$ |
|---|---|---|---|---|---|
| a-Si | 3.48 | 0.58 | 1.78 | 3.68 | 3.5 |
| $Si_3N_4$ | 2.05 | 0.9 | 1.75 | 2.2 | 5.5 |

Table 9.1: Performance comparison of two athermal waveguide designs, for an a-Si core and a $Si_3N_4$ core, with the same EP polymer overclad.

The advantage of high-index contrast (HIC) (a-Si) is neutralized under the constraint of athermal operation, and the $R_b$ performance is similar to the lower-index $Si_3N_4$ core (Table 9.1). Further, $Si_3N_4$ rings have a higher FSR due to their smaller group index ($n_g$), and they could additionally prove useful for athermal WDM applications where the FSR is the primary performance driver. When developing scaling rules for the material selection for athermal performance, it is important to realize that HIC systems lose their benefits over LIC systems in terms of small $R_b$ and high FSR, and the two performances becomes comparable. Another key advantage associated with the selection of a lower index contrast systems like $Si_3N_4$ is that their lower TO coefficients allow the use of a wider range of commercially available, CMOS BEOL compatible polymers to achieve athermal behavior as described below.

### 9.1.1 Material Selection for CMOS BEOL compatibility: core-cladding combination

The CMOS BEOL process flow involves metallization and annealing steps at temperatures between 400$^o$C - 450$^o$C. Further, the high metal levels use 248 nm lithography with dose levels between 20 - 50 mJ/cm$^2$ [86]. Though, the hyperlinked fluoropolymer (EP) under study can handle the expected UV dose levels without any significant degradation, the thermal decomposition might make it incompatible with the metallization and annealing steps. This encourages the use of polymers with high decomposition temperatures ( $T_{degradation}$ >450$^o$C) for back-end compatibility. BCB and polyimides belong to polymer classes with high thermal stability [56, 76, 122]. However, such polymer choices have low TO coefficients [123] that might be insufficient to compensate for the high TO coefficient of the Si cores (Table (9.2)). Hence, $SiN_x$

with a lower TO coefficient (Table (9.2)) might prove to be a better core choice for BEOL interconnects. Further, it is important to note that the BCB and polyimides have glass transitions occurring beyond 350$^{o}$C and 310$^{o}$C respectively [122]. Hence, the cooling rate might have to be optimized after the metallization step to ensure the desired optical functionality in these polymers. For a given polymer cladding choice, it is shown that the athermal constraint results in comparable n$_{eff}$ of the device for both the Si and SiN$_x$ cores [84]. So, the choice between the Si and SiN$_x$ core is not clear under the athermal constraint and the polymer cladding choice for CMOS compatibility could prove to be a crucial parameter in the figure-of-merit.

| **Core** | **Core TO**$(\times 10^{-4})$ | **Possible claddings** | **Cladding TO**$(\times 10^{-4})$ | **Cladding T**$_{degradation}(^{o}C)$ |
|---|---|---|---|---|
| a-Si | 2.3 | EP | $-2.65$ | $\approx 375$ |
| Si | 1.86 | EP | $-2.65$ | $\approx 375$ |
| SiN$_x$ | 0.4 | BCB | $-0.25$-$-1.15$ | $\approx 400 - 450$ |
| SiN$_x$ | 0.4 | Fluorinated polyimides | $-0.4$-$-1.04$ | $\approx 400 - 450$ |

Table 9.2: Polymer cladding choices for a given core for athermal application. SiN$_x$ core having a low TO coefficient can be compensated with a low TO coefficient polymer. Such polymers have a high decomposition temperature and hence are compatible with back-end CMOS processes.

## 9.2 Athermal constraint: Design solution

A highly confined SOI ring (450 nm × 220 nm) designed for a single TE mode of operation has a low bending loss (Fig. (9-2)) for a small bending radius ($R_b < 5\mu m$). This results in a small footprint and a high FSR performance. However, the passive athermal design requires mode expansion into the polymer cladding resulting in a low confinement. Hence, the bending loss of an athermal ring (channel cross-section) becomes significant for a small bending radius ($R_b < 5\mu m$). It is important to note that for a channel cross-section, the mode expands into both the polymer over-cladding and the SiO$_2$ under-cladding. Hence, athermal operation requires the polymer to not only compensate for the positive TO effects of the Si core but also account for the mode expansion in the buried oxide (BOX) layer. Thus, the effective index of the athermal channel cross-section is around 1.88 for TE operation (316 nm × 220 nm), while it is 1.85 for TM operation (658 nm × 220 nm). However, an alternate athermal design scheme could involve the use of slotted waveguides [19–22]. Athermal operation coupled with mode pinning in the slots reduces the leakage around bends for a given bending radius. FIMMWAVE simulations indicate that the vertical slot width should be 15 nm for a 500 nm × 220 nm SOI cross-section ($n_{eff}$ : 2.19) with EP over-cladding to achieve athermal TE operation. Similarly for the TM mode, athermal operation requires a 10 nm tall horizontal slot for a 250 nm × 400 nm ($n_{eff}$: 2.12) Si waveguide (Fig. (9-2)). Also, for the slotted cross-sections, most of the TO compensation arises from the polymer in the slot as opposed to the over-cladding region. Such high power in the slot can be further leveraged by using the polymer only in the slot regions and using $SiO_2$ as both the under-cladding and the over-cladding material. However, this requires a wider slot (50 nm) in case of TE operation and taller slot (24 nm) in case of TM operation resulting in a lower neff when compared to the slotted configurations shown in Fig. (9-2). Furthermore, it is useful to point out that the high $n_{eff}$ of athermal slotted rings and the lower expansion to the BOX region encourages the use of thinner BOX layer as compared to athermal channel cross-sections.

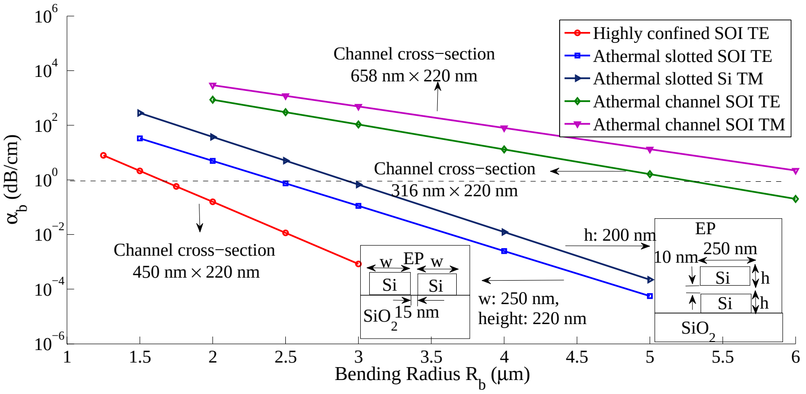

Figure 9-2: Bending loss performance at 1550 nm of various proposed athermal cross-sections compared with a standard SOI waveguide choice (450 nm × 220 nm).

The bending loss ($\alpha_b$) performance follows an exponential relation (Eq. (9.1)) with varying $R_b$ as deduced from the FIMMWAVE simulations (Fig. (9-2)). The $\alpha_b$ at 1550 nm goes beyond 1 dB/cm for $R_b$ corresponding to 6 $\mu$m for an athermal TM channel cross-section, 5 $\mu$m for an athermal TE channel cross-section and 1.6 $\mu$m for a highly confined TE cross-section (Fig. (9-2)). However, the footprint and the FSR performance of an athermal design is significantly improved due to the high $n_{eff}$ and mode-pinning of the slotted cross-sections where $R_b$ is 2.5 $\mu$m for TE operation and 3 $\mu$m for TM operation for a $\alpha_b$ of 1 dB/cm.

$$\alpha_b = A\exp(-CR_b) \tag{9.1}$$

where $\alpha_b$ is in dB/cm, $R_b$ is in $\mu$m, and $A$ (dB/cm), $C$ ($\mu m^{-1}$) are constants that depend on the confinement factor (waveguide geometry, index contrast and wavelength) and effective index of the waveguide. Lower the magnitude of $A$ and higher the magnitude of $C$, lower is the leakage around the bends resulting in a lower loss.

## 9.3 Channel design of an athermal add-drop filter

Silicon rings designed as add-drop filters are desired to have a high Q factor and a high FSR. For a first-order filter with a Lorentzian peak behavior, a high Q factor results in sharp channels, thereby, enabling a closer channel spacing (Fig. (9-3)) for a given channel cross-talk ($-20$ dB in our study). A high FSR results in a large channel count for a given channel spacing.

For a large $R_b$ and a small FSR, the intrinsic Q factor of the ring is dominated by the scattering loss ($\alpha_{sc}$) which is independent of the size of the ring. Hence, the channel spacing for a given cross-talk ($-20$ dB) remains constant for large rings. So, as the $R_b$ decreases, the FSR increases resulting in a linear increase in the channel count (Fig. (9-4)). However, at a small $R_b$ ($< 5\mu m$), the bending loss ($\alpha_b$) contribution to the intrinsic Q factor starts becoming significant. This increases the channel spacing required for a given channel cross-talk. So, the superior FSR performance of a small $R_b$ is nullified by the increased channel spacing, thereby decreasing the channel count (Fig. (9-4)). There exists an optimum bending radius ($R_b^{opt}$) (Eq. (9.2)) and an

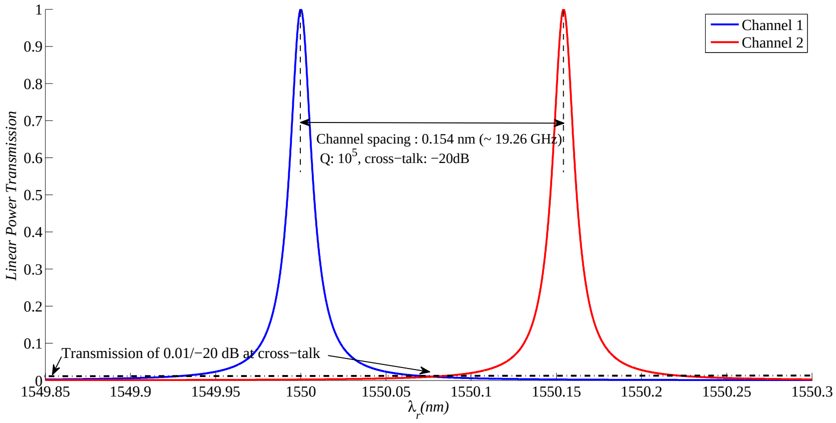

Figure 9-3: For a first order silicon add-drop filter with Lorentzian behavior, a Q factor of $10^5$ requires a channel spacing of 0.154 nm ($\approx$ 19.26 GHz) to keep the cross-talk with the neighboring channel to $-20$ dB (or 0.01 linear transmission). Hence, to get 100 channels with $-20$ dB cross-talk, a ring with Q factor of $10^5$ and FSR of 15.4 nm is desired.

optimum FSR ($FSR^{opt}$) which maximizes the channel count (Fig. (9-4)).

$$\alpha_b(R_b^{opt}) \times (CR_b^{opt} - 1) = \alpha_{sc} \tag{9.2}$$

Where $C$ is the constant pointed out in Eq. (9.1), $\alpha_b(R_b^{opt})$ corresponds to bending loss at optimum radius and $\alpha_{sc}$ corresponds to scattering loss. Increasing the $\alpha_{sc}$ decreases the $R_b^{opt}$ where the bending loss becomes comparable to the scattering loss resulting in an increased optimum FSR, $FSR^{opt}$.

If $\alpha_{sc}$ is assumed to be around 2 dB/cm, which is comparable to the low loss values reported for SOI waveguides in literature [124–129], the channel count limits of an athermal SOI ring and a highly confined SOI ring can be compared (Fig. (9-4)). The channel count of a highly confined TE cross-section increases with the FSR up to 46.5 nm ($R_b = 1.93$ $\mu$m) due to its low bending loss. On the other hand, athermal channel TE and athermal channel TM cross-sections show a significant decrease in the channel count performance beyond an $FSR^{opt}$ of 14.6 nm ($R_b = 6.22$ $\mu$m) and 12.25 nm ($R_b = 7.47$ $\mu$m) respectively due to the increased contribution of bending loss (Fig. (9-4)). A significant improvement in the channel count, $FSR^{opt}$ (36.5 nm

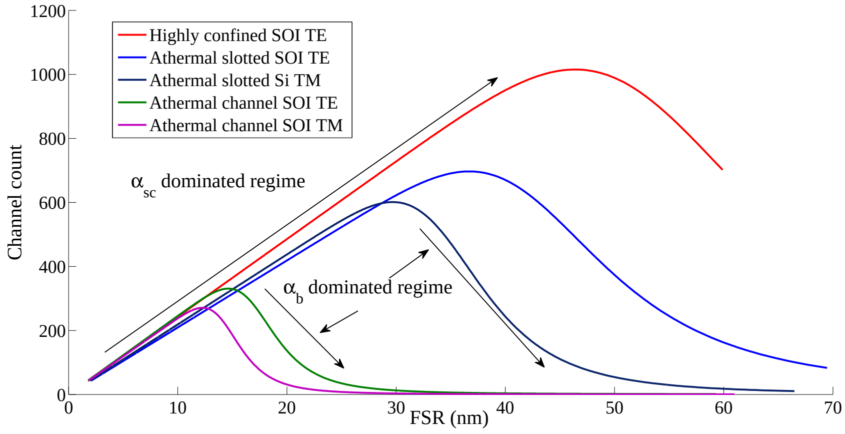

Figure 9-4: Channel count variation with FSR of various athermal cross-sections compared with a standard SOI cross-section. For an $\alpha_{sc}$ of 2 dB/cm and a $-20$ dB cross-talk, the channel count performance of highly confined SOI TE cross-section is superior to an athermal cross-section due to low bending loss.

for slotted TE and 30 nm for slotted TM) and footprint ($R_b = 2.85$ $\mu$m for slotted TE and 3.32 $\mu$m for slotted TM) performances is achieved by using slotted cross-sections for athermal design. The difference in slope of the linear regime is due to a lower group index of the slotted waveguide in comparison to a channel waveguide for a given FSR (Fig. (9-4)). It is important to note that the maximum channel count (*chcmax*) in all the cases is well beyond ($> 256$) what one requires in the immediate future.

## 9.4 Influence of scattering loss in the athermal design selection

Considering *chcmax* as a variable in the figure of merit driving the design selection, the choice between various athermal cross-sections might be determined by the $\alpha_{sc}$ that can be achieved. For a given scattering loss and cross-talk ($-20$ dB, $Tr_{cross-talk} = 0.01$), the athermal slotted TE cross-section has a higher *chcmax* than the athermal channel cross-sections. However, it is important to realize that *chcmax* decreases with increasing $\alpha_{sc}$ (Fig. (9-5)). In order to achieve a channel count of 256, the loss should be less than 2.12 dB/cm for an athermal channel TM cross-section, 2.62 dB/cm for an athermal channel TE cross-section, 5.05 dB/cm for an athermal slotted TM cross-section and 6.08 dB/cm for an athermal slotted TE cross-sections. In other words, the loss threshold for achieving a given channel count is improved by the adoption of slotted structures for athermal design.

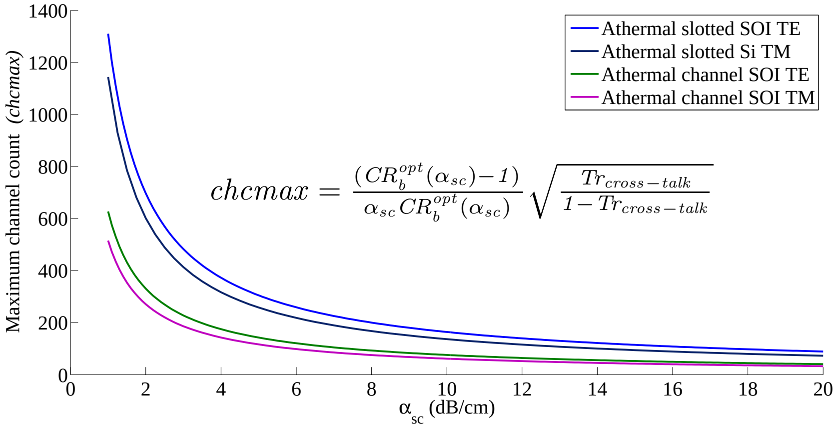

Figure 9-5: Dependency of maximum channel count (*chcmax*) on scattering loss for the athermal cross-sections under study. The *chcmax* decreases drastically with increasing scattering loss.

## 9.5 Power handling capacity

The superior footprint performance of a standard SOI cross-section compared to an athermal cross-section results in a better channel count performance (Fig. (9-4)). However, the standard highly confined SOI resonator has an inherent limitation in terms of its power handling capacity. In other words, two photon absorption or free carrier absorption induced thermal effect at high launch powers, red-shifts the response of an SOI filter thereby limiting its power handling and data capacity. Such a limitation is overcome in an athermal design which is unaltered by the TO effects associated at high power. The power handling capacity can be characterized through the transmission measurements (Fig. (9-6)) at two different wavelengths, 1536 nm and 1576.8 nm (closer to the athermal operation point), for different launch power levels (from 6 to 28 dBm). Red-shifts in the resonances at high input powers are due to thermal effects induced by TPA/FCA. The decrease in the resonance shift from 92 pm (@1536 nm) to 20 pm (@1576.8 nm) for 27 dBm of input power confirms the greater extent of thermal compensation for a resonance closer to athermal operation (Fig. (9-6)). There is no appreciable shift in the measured spectral response around 1576.8 nm up to an input power of 18 dBm (Fig. (9-7)). The design of the waveguide can be optimized to further increase the achieved thermal compensation, thereby enabling power insensitive operation. High data capacity requiring high power operation can thus be achieved in an athermal design.

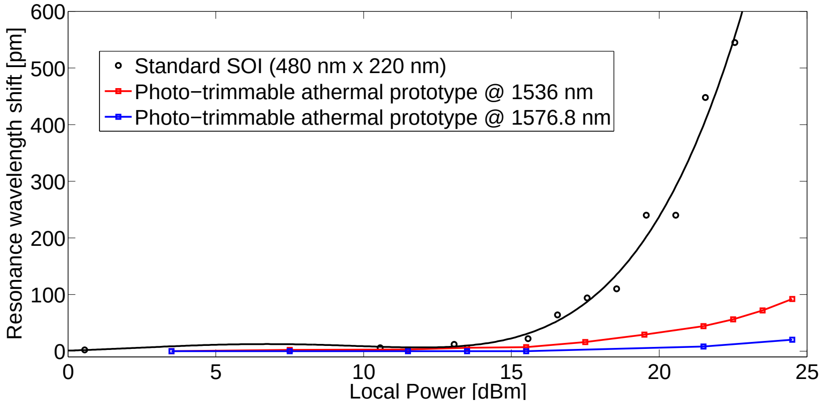

Figure 9-6: Power-dependent resonance shift is measured for two wavelengths, 1536 nm and 1576.8 nm (around the athermal operation point), at launch powers ranging from 6 to 27 dBm. Thermal effects, induced by TPA/FCA at high power levels, are compensated to a larger extent by a resonance closer to athermal operation (1576.8 nm).

## 9.6 Aggregate waveguide bandwidth performance

For a given resonance shift (≈10 pm), the power handling capacity thus improves 10 folds when going from a standard SOI waveguide design (15.8 mW) to an athermal waveguide design (158 mW) [130, 131]. As a result, for a given receiver sensitivity, an athermal add-drop filter can communicate with 10 times more receivers than the standard highly confined SOI filter. Alternatively, the higher power handling capacity can also translate as a higher bit rate (higher clockspeed) for a given receiver sensitivity. It is useful to define the receiver weighted aggregate bandwidth that is proportional to the product of channel count and the power handling capacity and treat it as a new figure of merit to compare the various design cross-sections (Fig. (9-2)). Assuming a given receiver sensitivity of 100 nW/Gb/s, higher power can either result in higher number of receivers or higher bit rate. The high power operation of an athermal WDM link outweighs its footprint limitations as is reflected in its superior aggregate bandwidth performance compared to a standard SOI WDM link (Fig. (9-8)). The variation of bandwidth with the FSR is a result of the channel count behavior for varying FSR (Fig. (9-4)). The slotted athermal SOI TE cross-section has a combination of high channel count (Fig. (9-4)) and high power capacity resulting in the highest aggregate bandwidth performance among the athermal designs under consideration.

## 9.7 Concluding remarks

From the system design perspective, increasing the add-drop channel count increases the total bandwidth of an electronic-photonic integrated chip. Silicon based add-drop filters have a high FSR that enables large channel counts. However, the low confinement of the passive athermal design limits the maximum FSR. This chapter establishes the existence of an optimum FSR that maximizes the channel count and derives the governing relation. The high effective index of an athermal slotted cross-section and the mode-pinning in slot results in its superior bending performance compared to the channel cross-sections. The channel count performances of four athermal design choices have been compared for a given channel cross-talk and scattering loss. A vertically slotted cross-section proves to be the best choice in terms of maximizing the channel count of an athermal add-drop filter for a given scattering loss. Also, the strong dependence of maximum channel count on the scattering loss and its influence in the final design choice is understood. Finally, this chapter shows that the power advantage of an athermal filter outweighs its channel count limitations resulting in a

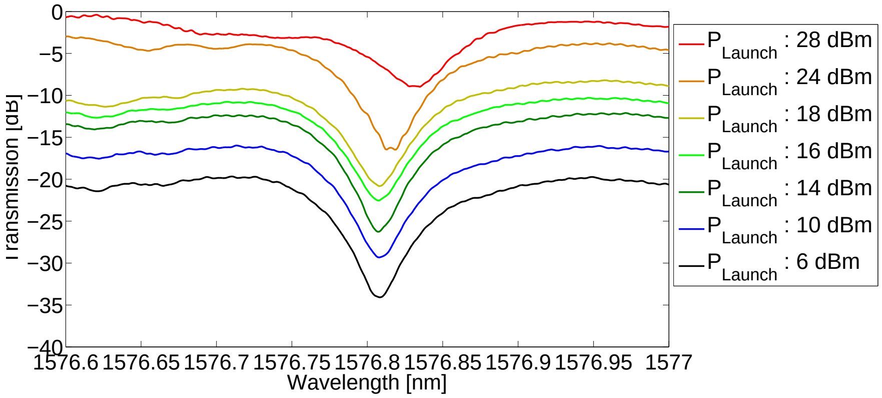

Figure 9-7: Normalized frequency domain response of the resonator around 1576.8 nm for increasing launch power ($P_L$) shows no appreciable power-dependent resonance shift upto 18dBm of $P_L$.

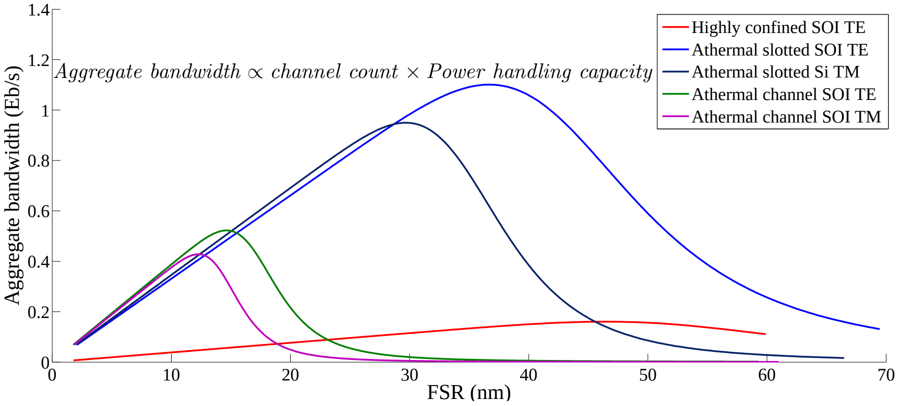

Figure 9-8: Aggregate bandwidth variation with FSR of the athermal cross-sections under study compared with a standard highly confined SOI waveguide. The aggregate bandwidth is proportional to the product of the channel count and the power handling capacity of a given add-drop filter for a given receiver sensitivity.

significantly higher receiver weighted aggregate bandwidth compared to a standard SOI add-drop filter.

The influence of the athermal constraint on the system behavior completes the study of an athermal photonic circuit in this thesis. The key findings of the thesis are listed in the next chapter.

# Chapter 10

# Key findings and Future work

## 10.1 Key findings

This thesis has addressed various components of an athermal photonic circuit on a silicon platform. This includes device design, material selection, dielectric encapsulation for multi-layer stacking, post-fabrication resonance trimming and system integration of athermal silicon add-drop filters. The key findings in each design space can be listed as follows:

1. Passive athermal prototype with the lowest reported TO peak shift of 0.5 pm/K for silicon resonators: The negative TO coefficient of polymers is utilized to achieve passive thermal compensation.

2. Athermal filter waveguide dimensions depends on the wavelength to be filtered out: The design rule has an associated dispersion effect that needs to be accounted for in order to achieve the desired confinement factor.

3. Observation and explanation of residual second order effects at very small TO peak shifts: The dependence of the index of a material with temperature is not strictly linear and has a quadratic component of the order of $10^{-5} - 10^{-6}\ K^{-2}$ that becomes significant when dealing with effective index variation of a similar magnitude. The temperature dependence of the material TO coefficient and

the core confinement factor was experimentally measured through the quadratic variation of resonance with temperature of athermal devices.

4. Co-polymer cladding provides an extra degree of freedom to design $n$ and TO independently: The material design space was explored by analyzing two silicon-polymer composite structures, deposited using iCVD, pPFDA and p(PFDA-*co*-DVB), for thermal compensation. This work shows that for a fluorinated acrylate polymer, reducing the C-F bond density decreases the molar volume and increases the refractive index. The TO coefficient of the co-polymer can be designed by choosing a cross-linker of a desired thermal volume expansion coefficient.

5. Hermetic sealing using dielectric cap encourages the possibility of multi-layer stacking on polymer clad devices: This is carried out by a low temperature HD-PCVD technique to retain the polymer functionality. The deposited dielectric layer prevents oxygen diffusion into the polymer thereby ensuring robust performance of the polymer cladding. Stiffer dielectrics also improve the mechanical stability of the polymer-dielectric bi-layer stacks.

6. Thin photosensitive layer of $As_2S_3$ enables visible light trimming for fabrication tolerances: Athermal behavior requires that the thickness of $As_2S_3$ inter-clad is of the order of 10's of nanometers to ensure mode expansion into the polymer over-cladding. This work shows that the photo-sensitive behavior is enhanced for thickness values that are less than the absorption length due to uniform absorption of the entire film. Further, the annealing of $As_2S_3$ densifies the film towards equilibrium stoichiometry (thereby eliminating the red-shift) and locks the photo-sensitive response to one trimming direction. The photo-volume expansion of $As_2S_3$ under visible light illumination decreases its refractive index. Furthermore, the optimization of $As_2S_3$ thickness is desired to retain the athermal behavior after resonance trimming.

7. The high power handling capacity of athermal rings outweighs its low FSR

thereby enabling higher aggregate bandwidth compared to conventional rings: Positive-negative TO composite structure is not influenced by thermal effects induced at high launch powers. This combined with superior bending performance of the athermal slotted cross-section is shown to have the highest aggregate bandwith density.

## 10.2 Future work

### 10.2.1 Design of athermal higher order filters

Higher order ring filters are preferred for DWDM application due to their flat pass band and steeper roll-off (Section 3.4). For a given effective TO coefficient of the waveguide and a given transmission loss and radius of the rings, the resonance wavelength of both 1st order and 2nd order filters (mid-point of the pass band) shift by the same extent (Fig. (10-1)). However, 2nd order ring has a flatter and broader pass band, which could be more robust to small temperature fluctuations as opposed to the first order filters. For instance, if a 2nd order filter is designed to have a 0.04 nm pass band (Fig. (10-2)), it provides the desired transmission behavior over a wider temperature range ($\Delta T\ (in\ K) = \frac{Pass\ bandwidth\ (in\ nm)}{TO\ resonance\ shift\ (in\ nm/K)}$) as opposed to a single ring filter that has a much smaller pass-band. The next step would involve fabrication of athermal higher-order filters and validation of the simulation results.

The passive athermal design rule involves expanding the mode into the cladding, thereby constraining the minimum achievable bending radius (or the maximum FSR) due to a large bending loss at low radius. Bending loss simulations (Fig. (9-2)) indicate that the maximum achievable FSR is around 16 nm for an athermal first-order ring filter (channel cross-section). It is desirable to design filters with an FSR of around 30 nm for DWDM applications with large channel counts (32/64). The vernier effect in higher-order filters can be leveraged to address the FSR limitation of an athermal first-order filter.

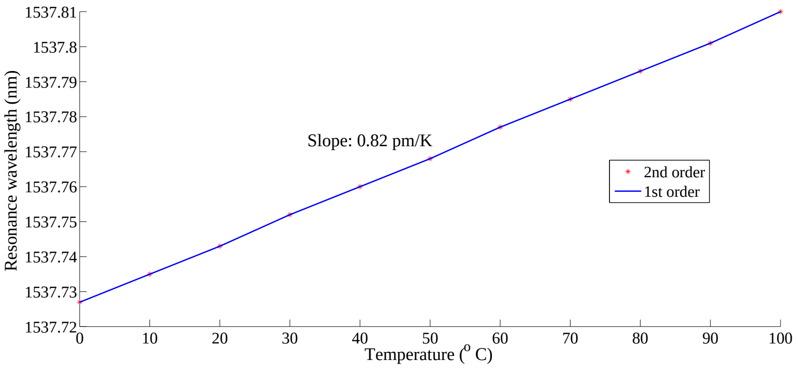

Figure 10-1: The simulated resonance shift of a 1st order and 2nd order filters with the same effective TO coefficient, loss and ring radii. The effective TO resonance shift is the same in both cases ruling out any unexpected effects arising due to higher order behavior in second order ring.

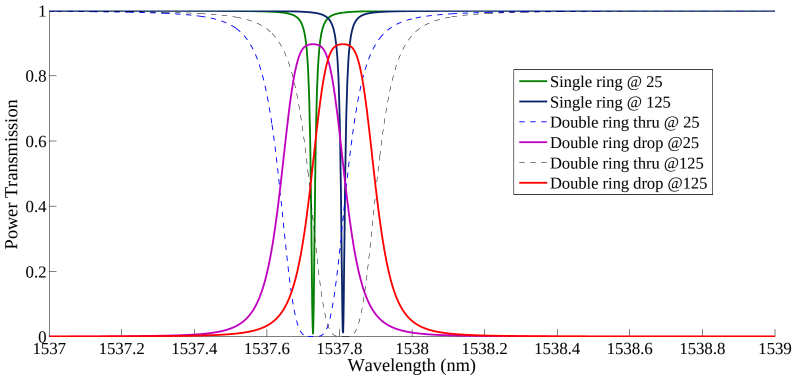

Figure 10-2: The simulated transmission spectrum of 1st and 2nd order filters (with the same effective TO) at 2 different temperatures (25$^o$C and 125$^o$C) shows the possibility of robust performance of 2nd order filters to small temperature fluctuations due to wider pass band. The Tolerable temperature fluctuation ($\Delta T\ (in\ K)$) is given by $\frac{Pass\ bandwidth\ (in\ nm)}{TO\ resonance\ shift\ (in\ nm/K)}$

### Athermal vernier filters

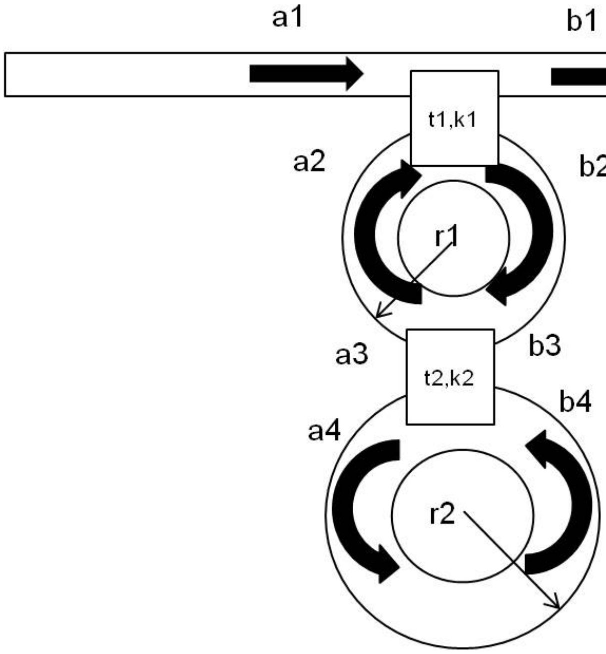

Figure 10-3: Schematic of a vernier filter configuration with 2 coupled rings of different radii (r1 and r2). Owing to different radii, both the rings have different FSR. The resonance of such a double-ring configuration is satisfied only when a given wavelength satisfies the resonance in both the rings.

The passive athermal design employed in this thesis can be extended to design athermal vernier filters. A vernier filter in an all-pass configuration consists of 2 coupled rings of different radii that get information from an input bus waveguide (Fig. (10-3)). Owing to different radii, both the rings have different FSR. The resonance of such a double-ring configuration is satisfied only when a given wavelength satisfies the resonance in both the rings. Hence, the resultant $FSR_{vernier}$ of the vernier filter is given by $FSR_{vernier} = m \cdot FSR_1 = n \cdot FSR_2$ [132], where $m$ and $n$ are integers. So, it is possible to leverage the interference effects of a coupled ring system to address the FSR limitation of an athermal single ring filter.

The design approach involves starting with two rings of comparable radii (r1=6 $\mu$m, r2= 6.25 $\mu$m). An asymmetry in the coupling conditions of the 2 rings (Fig. (10-3)) requires r2 to be slightly different from r1 to ensure resonance matching between the rings. Considering the same loss in both the rings ($\alpha1 = \alpha2 = 5\ dB/cm$, the vernier filter system can be analyzed in a manner similar to the scattering matrix approach described in section (3.1.1) assuming k1=0.09 and k2=0.03 (Fig. (10-3)). The transmission spectrum of such a system has an FSR of 17.8 nm (Fig. (10-4)).

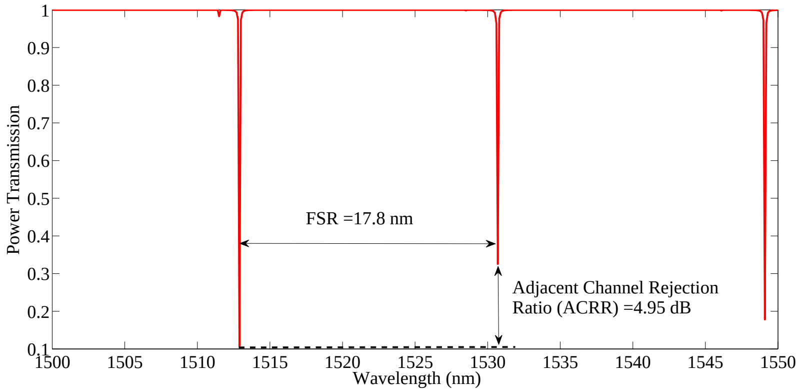

Figure 10-4: Transmission of a double ring system in an all-pass configuration where r1= 6 $\mu$m, r2= 6.25 $\mu$m, k1= 0.09, k2= 0.03 and transmission loss of both the rings, $\alpha 1 = \alpha 2$ equals 5 dB/cm.

Considering DWDM applications where the desired FSR is 30 nm, having a transmission peak at 1530.6 nm (Fig. (10-4)) can result in unwanted filtering (cross-talk) of adjacent channels by the add-drop filter. This cross-talk can be quantified by Adjacent Channel Rejection Ratio (ACRR in dB) defined as $10\log(\frac{P_{1530.6}}{P_{1512.8}})$, where $P_{1530.6}$ and $P_{1512.8}$ are the powers transmitted at 1530.6 nm and 1512.8 nm respectively. The current design has an ACRR of 4.95 dB. The first step involves increasing the transmission (suppressing the resonance) at 1530.6 nm thereby increasing the ACRR. This involves optimization of r2. The transmission at 1530.6 nm increases with r2 and saturates at 0.8 for r2 = 11.6 $\mu$m (Fig. (10-5)). However, beyond 11.6 $\mu$m, the ACRR decreases drastically thereby fixing the optimum r2 at 11.6 $\mu$m (Fig. (10-6)).

The maximum ACRR is still around 8.6 dB for r2 = 11.6 $\mu$m (Fig. (10-6)). The next step involves maximizing the ACRR by optimizing the ring-bus coupling coefficient (k1) and ring-ring coupling coefficient (k2) (Fig. (10-3)). $P_{1530.6}$ reaches a peak of 0.9622 at k2=0.025 for various values of k1 (Fig. (10-7)). Though $P_{1530.6}$ increases beyond k2=0.04 and saturates at 0.99 beyond k2=0.08, we choose k2=0.025

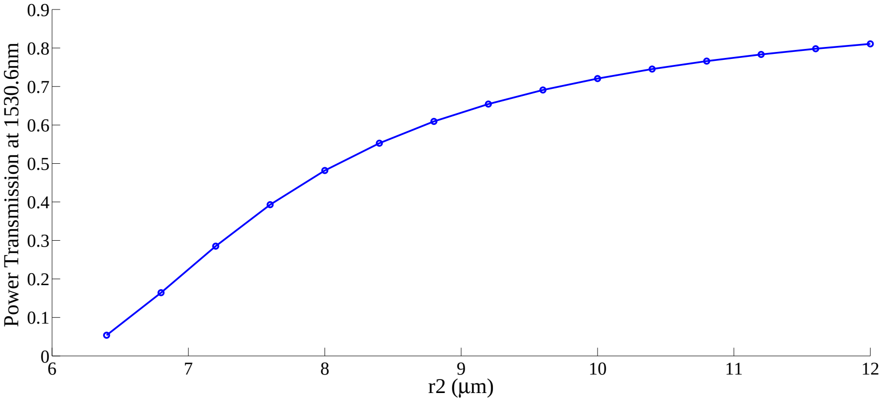

Figure 10-5: Power transmission at 1530.6 nm increases with r2 and saturates at 0.8 for r2=11.6 $\mu$m.

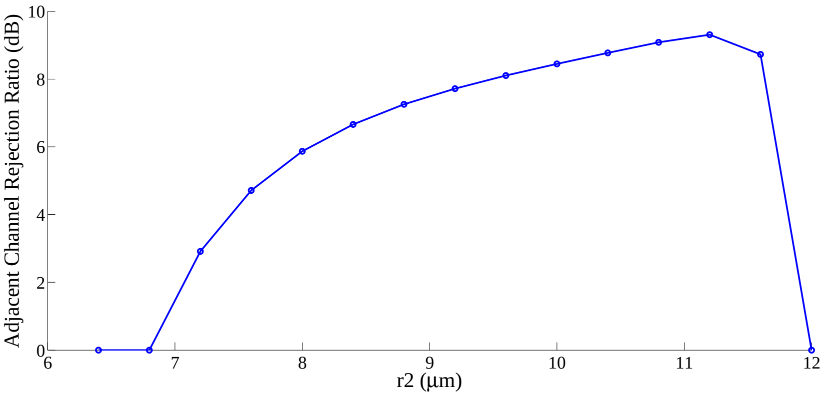

Figure 10-6: ACRR increases with r2 and reacheas a maximum at 9.3 dB for r2=11.2 $\mu$m before decreasing for any further increase of r2.

as the optimum value as it corresponds to a lower coupling loss (lower k corresponds to a lower coupling loss and a higher Q factor of the ring). Finally, the optimum k1 is found to be 0.065 (Fig. (10-8) for an optimized r2=11.6 $\mu$m and k2=0.025, where the ACRR reaches a maximum value of 25 dB.

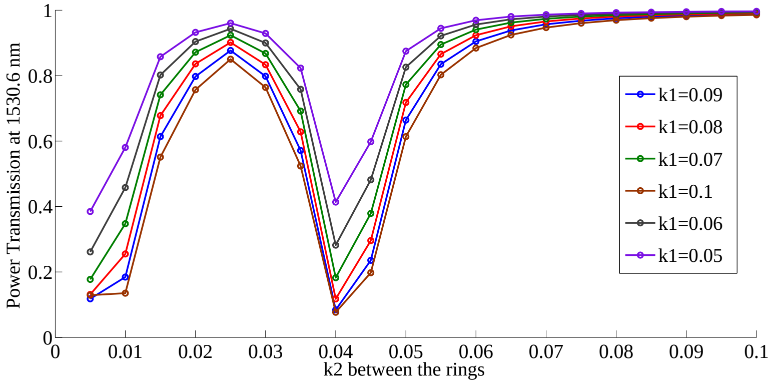

Figure 10-7: Transmission at 1530.6 nm reaches a peak of 0.9622 for k2=0.025 for various values of k1. It decreases beyond k2=0.025 before increasing around k2=0.04 and saturating beyond 0.08 at a power transmission of 0.99.

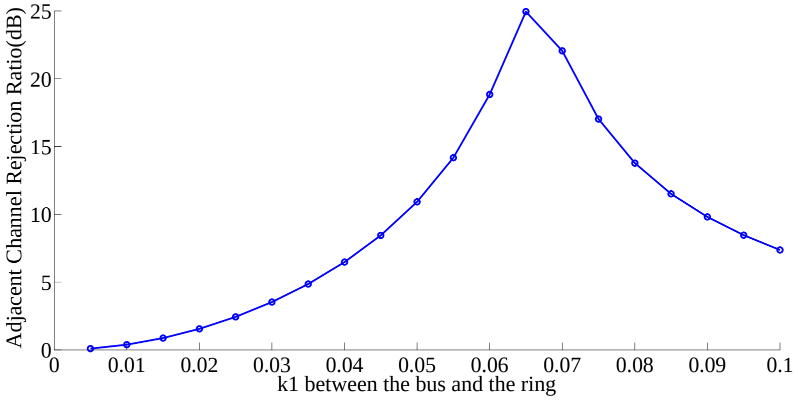

Figure 10-8: ACRR reaches a maximum of 25 dB for k1=0.065, k2=0.025 and r2=11.6 $\mu$m.

The ACRR variation with r2 (Fig. (10-9)) reveals that the maximum value is 25 dB for r2 = 11.6 $\mu$m. As a consequence of the high ACRR (25 dB), the FSR of the new design is found to be around 36.2 nm (Fig. (10-10)). The realized FSR is higher than the desired value of 30 nm. The final parameters of the optimum vernier filter can be listed as:

1. r2: 11.6 $\mu$m
2. k1: 0.065
3. k2: 0.025
4. ACRR: 25 dB
5. FSR: 36.2 nm

The future direction involves fabrication of the proposed vernier filters and validating the improved FSR performance of athermal vernier filters. This thesis concludes with the proposal of another possible future direction involving athermal all-optical orthogonal frequency division multiplexing.

### 10.2.2 Athermal all-optical orthogonal frequency division multiplexing

#### All-optical OFDM receiver

An all-optical orthogonal frequency division multiplexing (AO-OFDM) has been proposed as an attractive solution to overcome the speed limitations of electronic digital signal processing (DSP) based fast fourier transform/inverse fast fourier transform (FFT/IFFT) [133, 134]. An all-optical discrete fourier transform (DFT) (Fig. (10-11(a))) can be performed by integrated passive optical components with an appropriate temporal delay and phase shifters. AO-OFDM receivers based on N×N multi-mode interference (MMI) splitters (Fig. (10-11(b))) coupled with delay lines and phase shifters [133], arrayed waveguide gratings (AWG) [134], asymmetric Mach-Zehnder interferometers (AMZI) [135, 136] and two-stage cascaded AMZIs [137] have been demonstrated. All the proposed devices require careful design of the optical delay lines and the phase shifters to achieve the desired FFT operation. This includes

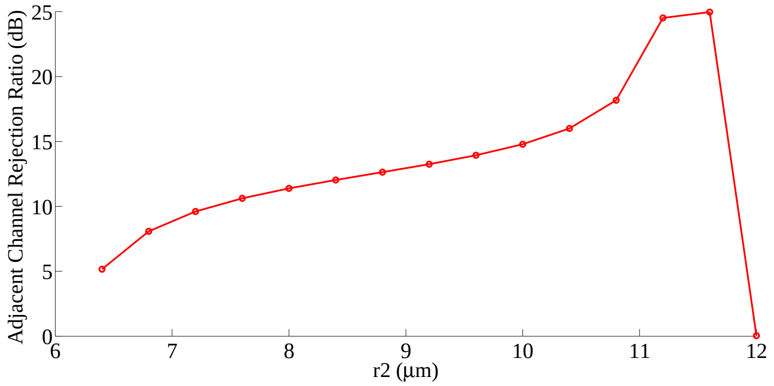

Figure 10-9: ACRR variation with r2 confirms the optimized vernier filter design performance for r2= 11.6 $\mu$m.

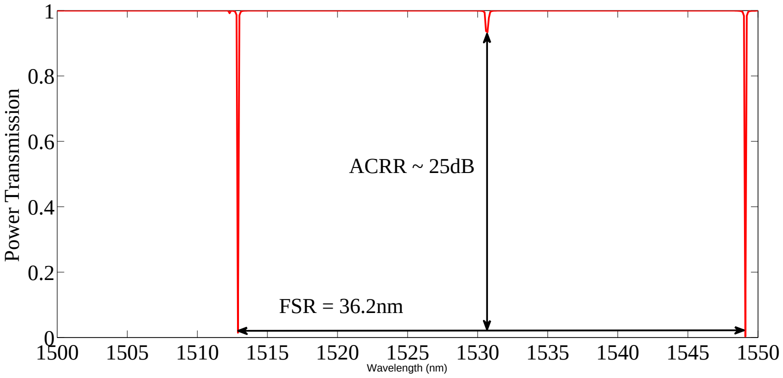

Figure 10-10: Transmission spectrum of optimized vernier filter in all-pass configuration where r2=11.6 $\mu$m, k1=0.065, k2=0.025. Final ACRR is 25 dB and FSR is 36.2 nm

robust performance under temperature fluctuations that can alter the optical path length of the receiver circuit. For instance, an increase in the temperature increases the index of array waveguide and the slab region thereby altering the phase shift response in addition to limiting the channel spacing of the AWG based AO-OFDM receiver in [134]. Similarly, the design of N×N MMI splitters (Fig. (10-11(b))) for simultaneous demultiplexing of N subcarriers in [133] requires port dependent phase change to get the desired frequency response at the output ports. Even though the MMI splitter is not as sensitive as a ring resonator to temperature changes since the MMI operates based on the interference between the modes, the design rule calls for a definite phase relation at the input ports. Any temperature change affects all the optical delay lines by the same extent thereby preserving the relative temporal delay among different paths. However, the operation of TO phase shifters might have to change dynamically to account for the TO induced variations in temporal delay in each arm to maintain the desired phase relation at the input port of the N×N MMI. Further, the footprint associated with the TO phase shifters limit the density of integration. We propose an athermal N×N MMI splitter based AO-OFDM receiver with athermal optical delay lines that would be robust to temperature fluctuations.

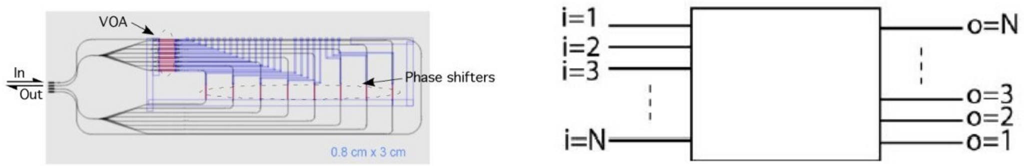

(a)

(b)

Figure 10-11: 10-11(a) Schematic of all-optical DFT circuit (reproduced from [133]). 10-11(b) Schematic of N×N MMI (reproduced from [133]).

### Athermal N×N MMI splitter based AO-OFDM

The proposed passive athermal solution is an extension of this thesis work based on polymer claddings with a negative TO coefficient. The silica core choice has an inherent advantage of a low TO coefficient ($1\times10^{-5}\ K^{-1}$) that provides a lot of freedom for polymer choice whose TO coefficient can vary between $-1\times10^{-4}\ K^{-1}$ - $-4\times10^{-4}\ K^{-1}$.

For instance, polymers based on fluorinated polyimide or perfluorocyclobutyl (PFCB) aryl ether polymers with high decomposition temperatures (around 400 - 450$^o$C) can be chosen to be compatible with CMOS back-end process flow. The athermal operation of the optical delay lines ensures a stable temporal relation between the input ports of an N×N MMI splitter. However, FFT requires the addition of a phase shifter in each delay line to induce a desired phase shift to maintain the phase relation at the input port of the MMI splitter. Athermal design rules out the possibility of a TO phase shifter and invokes the need for an alternative phase shifter design. We propose following solutions from material and design perspectives to overcome this problem:

1. Material solution: As mentioned above, the passive thermal compensation of silica based core can be realized by most polymer materials. The requirement of phase modulation and athermal operation motivates the need for an electro-optic (EO) polymer cladding with sufficient TO coefficient ($< -1 \times 10^{-5}\ K^{-1}$). Both these requirements can be met by poling the polymer cladding locally with non-linear optic (NLO) chromophores. Successful incorporation of NLO chromophores in a high $T_g$ polyimide host has been demonstrated to exhibit EO effect with long term stability at high temperatures [56]. The scattering loss associated with such a composite has been minimized by controlling the homogeneity of chromophore dispersion before and after the poling. Hence, while optical delay lines with polyimide cladding are athermal, EO based phase shifters can be realized locally by poling polyimide with NLO chromophores. It is important to understand that the athermal requirement fixes the confinement factor in the silica core and the polymer cladding. So, the magnitude of EO based phase shift is limited by the extent of light in the polymer cladding. However, this limitation can be overcome by extending the length of such a modulator. A similar approach is also possible with PFCB as the host polymer for NLO chromophores. Finally, the trimming of such devices for fabrication variation can be carried out by UV curing of the polymer layer.

2. Design solution: Alternatively, a silica based ring coupled to each delay line

fulfils the requirement of phase shifting. The ring parameters can be chosen based on the desired phase shift in each delay line. Further, the dispersion associated with the phase shift in each delay line can be tailored by choosing a cascaded ring system. Also, it is important to realize that the TO response of the ring is influenced by the waveguide dispersion. However, the athermal operation of silica waveguides is achieved for fairly large waveguide dimensions (due to the low TO coefficient of silica) where the dispersion of the TO response might not be significant over the wavelength range of interest. Finally, the FSR of the ring is determined by the radius which is limited by the bending loss of the silica ring. However, an alternative design scheme involving slotted rings can overcome this limitation. Further, the resonance variation due to the fabrication tolerance of the rings can be trimmed by UV curing of polymer cladding (most of the polymer materials are sensitive to UV radiation). Finally, one can envision simultaneous demultiplexing and phase modulation using rings thereby ruling out the need for MMI based demultiplexing.

### Athermal AO-OFDM transmitter

At the transmitter side, the main optical components of AO-OFDM are laser source and modulator.

1. Athermal laser source: Increasing the temperature of a laser material decreases its band gap thereby shifting the central wavelength of the gain spectrum to longer wavelengths. Conventionally, a laser source is maintained at a constant temperature using a thermo-electric cooler to overcome this limitation. However, an on-chip WDM laser based of germanium is desired to have a stable emission wavelength spectrum without a lot of control overhead. The passive solution to temperature dependent material gain spectrum involves mode-locking the laser output by a suitable cavity design resulting in a frequency comb generation [37]. The octave spanning frequency comb spectrum using silica based toroidal resonators and silicon nitride based micro-resonators utilizing optical parametric oscillation have been demonstrated [37]. Also, the TO coefficients

of both silica and silicon nitride can alter the emission wavelength spectrum with varying temperature depending on the device's resonance. Our proposed passive athermal solution can be extended to frequency comb generation using silica/silicon nitride based resonators. Thus a stable emission spectrum is maintained at all temperatures when a continuous laser source (germanium) is amplified (Optical amplifier) and transmitted through an athermal silica/silicon nitride resonator that creates a temperature independent frequency comb. The low confinement requirement of athermal design is not a concern for the comb generation as the resonators have large bending radii to meet the desired high Q and low FSR of the comb. However, the bandwidth of the frequency comb is limited by the dispersion of the cavity. Hence, the dispersion compensated resonator design is desired to increase the bandwidth. Additionally, the dispersion compensation solution should be consistent with the desired cross-section for athermal behavior. Finally, the design solution should also address the dispersion of the TO response of the ring. Solutions involving cascaded rings can provide more controlling parameters while optimizing the dispersion characteristics of such a system.

2. Athermal modulators: Lastly, the need for athermal operation of active devices like modulators becomes extremely relevant while considering ring modulators whose spectrum changes with temperature. The aforementioned material design solution can be extended for a silica core based EO ring modulator with NLO chromophore poled polyimide cladding. On the other hand, athermal silicon based EO ring modulators might require reactive ion etching (RIE) through the polymer cladding layer and electro-less deposition of copper vias (low temperature deposition) to create a metal contact with Si core. This requires careful selection of polymer cladding and optimization of processing techniques for polymer etching and metal deposition techniques.

# Bibliography

[1] G. Moore, "Cramming more components onto integrated circuits," *Electronics Magazine*, vol. 38, no. 8, p. 114, 1965.

[2] D. Muller, "A sound barrier for silicon?," *Nature Materials*, vol. 4, pp. 645–647, 2005.

[3] A. Agarwal and M. Levy, "The kill rule for multicore," *Proceedings of the 44th annual conference on Design automation - DAC '07*, p. 750, 2007.

[4] C. Shannon, "Communication In The Presence Of Noise," *Proceedings of the IEEE*, vol. 86, pp. 447–457, Feb. 1998.

[5] R. Kirchain and L. Kimerling, "A roadmap for nanophotonics," *Nature Photonics*, vol. 1, no. June, pp. 303–305, 2007.

[6] L. C. Kimerling and J. Michel, "Monolithic Microphotonic Integration on the Silicon Platform," *ECS Transactions*, vol. 41, no. 7, pp. 3–13, 2011.

[7] L. Kimerling, L. Negro, S. Saini, Y. Yi, and D. Ahn, "Monolithic silicon microphotonics," *Silicon Photonics, Topics in Applied Physics*, vol. 94, pp. 89–121, 2004.

[8] M. Taylor, W. Lee, J. Miller, D. Wentzlaff, I. Bratt, B. Greenwald, H. Hoffmann, P. Johnson, J. Kim, J. Psota, a. Saraf, N. Shnidman, V. Strumpen, M. Frank, S. Amarasinghe, and a. Agarwal, "Evaluation of the raw microprocessor: an exposed-wire-delay architecture for ILP and streams," *Proceedings. 31st Annual International Symposium on Computer Architecture, 2004.*, pp. 2–13, 2004.

[9] G. Kurian, J. Miller, J. Psota, J. Eastep, J. Liu, J. Michel, L. C. Kimerling, and A. Agarwal, "ATAC: A 1000-core cache-coherent processor with on-chip optical network," *Proceedings of Parallel Architectures and Compilation Techniques (PACT)*, no. September, 2010.

[10] G. Kurian, C. Sun, C.-H. O. Chen, J. E. Miller, J. Michel, L. Wei, D. a. Antoniadis, L.-S. Peh, L. Kimerling, V. Stojanovic, and A. Agarwal, "Cross-layer Energy and Performance Evaluation of a Nanophotonic Manycore Processor System Using Real Application Workloads," *2012 IEEE 26th International Parallel and Distributed Processing Symposium*, pp. 1117–1130, May 2012.

[11] M. Georgas, J. Leu, and B. Moss, "Addressing link-level design tradeoffs for integrated photonic interconnects," *Custom Integrated Circuits Conference*, vol. 978-1-4577, no. 11, pp. 1–8, 2011.

[12] M. Rasras, D. Gill, and S. Patel, "Demonstration of a fourth-order pole-zero optical filter integrated using CMOS processes," *Journal of Lightwave Technology*, vol. 25, no. 1, pp. 87–92, 2007.

[13] B. Saleh and M. Teich, *Fundamentals of photonics.* John Wiley & Sons, 1st ed., 1991.

[14] B. L. Heffner and P. R. Hernday, "MEASUREMENT OF POLARIZATION MODE DISPERSION," *Hewlett-Packard Journal*, no. February, pp. 27–33, 1995.

[15] Photon Design, "Modes of an SOI waveguide."

[16] A. Sudbo, "Film mode matching: a versatile numerical method for vector mode field calculations in dielectric waveguides," *Pure and Applied Optics*, vol. 2, pp. 211–233, 1993.

[17] A. Sudbo, "Numerically stable formulation of the transverse resonance method for vector mode-field calculations in dielectric waveguides," *IEEE Photonics Technology Letters*, vol. 5, no. 3, pp. 342–344, 1993.

[18] A. Sudbo, "Improved formulation of the film mode matching method for mode field calculations in dielectric waveguides," *Pure and Applied Optics*, vol. 4, pp. 381–388, 1994.

[19] J.-M. Lee, D.-J. Kim, G.-H. Kim, O.-K. Kwon, K.-J. Kim, and G. Kim, "Controlling temperature dependence of silicon waveguide using slot structure.," *Optics express*, vol. 16, pp. 1645–52, Feb. 2008.

[20] Q. Xu, V. Almeida, R. Panepucci, and M. Lipson, "Experimental demonstration of guiding and confining light in nanometer-size low-refractive-index material," *Optics letters*, vol. 29, no. 14, pp. 1626–1628, 2004.

[21] V. R. Almeida, Q. Xu, C. A. Barrios, and M. Lipson, "Guiding and confining light in void nanostructure," *Optics Leters*, vol. 29, no. 11, pp. 1209–1211, 2004.

[22] R. Sun, P. Dong, N.-n. Feng, C.-y. Hong, J. Michel, M. Lipson, and L. Kimerling, "Horizontal single and multiple slot waveguides: optical transmission at lambda = 1550 nm," *Optics express*, vol. 15, pp. 17967–72, Dec. 2007.

[23] H. Haus, *Waves and fields in optoelectronics.* 1984.

[24] B. Little, S. Chu, W. Pan, and Y. Kokubun, "Microring resonator arrays for VLSI photonics," *IEEE Photonics Technology Letters*, vol. 12, pp. 323–325, Mar. 2000.

[25] B. Little, S. Chu, H. Haus, J. Foresi, and J.-P. Laine, “Microring resonator channel dropping filters,” *Journal of Lightwave Technology*, vol. 15, pp. 998–1005, June 1997.

[26] T. Barwicz, M. Popović, P. Rakich, M. Watts, H. Haus, E. Ippen, and H. Smith, “Microring-resonator-based add-drop filters in SiN: fabrication and analysis.,” *Optics express*, vol. 12, pp. 1437–42, Apr. 2004.

[27] S. Chu, B. Little, W. Pan, T. Kaneko, S. Sato, and Y. Kokubun, “An eight-channel add-drop filter using vertically coupled microring resonators over a cross grid,” *IEEE Photonics Technology Letters*, vol. 11, pp. 691–693, June 1999.

[28] F. Morichetti and A. Melloni, “Polarization converters based on ring-resonator phase-shifters,” *Photonics Technology Letters, IEEE*, vol. 18, no. 8, pp. 923–925, 2006.

[29] T. Krauss and P. Laybourn, “Monolithic integration of a semiconductor ring laser and a monitoring photodetector,” *SPIE, Integrated Optical Circuits*, vol. 1583, pp. 150–152, 1991.

[30] T. Chu and N. Fujioka, “C and L Bands Wavelength Tunable Laser with Silicon Photonic-wire Waveguide Micro-ring Resonators,” *Integrated Photonics Research, OSA*, pp. 3–5, 2010.

[31] K. Nemoto, T. Kita, and H. Yamada, “Narrow spectral linewidth wavelength tunable laser with Si photonic-wire waveguide ring resonators,” *Group IV Photonics (GFP)*, vol. 4, pp. 216–218, 2012.

[32] T. Segawa and S. Matsuo, “Monolithically integrated wavelength-routing switch with double-ring-resonator-coupled tunable lasers,” *Integrated Photonics Research, OSA*, pp. 1–3, 2010.

[33] V. Almeida, C. Barrios, R. Panepucci, and M. Lipson, “All-optical control of light on a silicon chip,” *Nature*, vol. 431, no. October, pp. 1081–1084, 2004.

[34] P. Dong, R. Shafiiha, S. Liao, H. Liang, N.-N. Feng, D. Feng, G. Li, X. Zheng, A. V. Krishnamoorthy, and M. Asghari, “Wavelength-tunable silicon microring modulator.,” *Optics express*, vol. 18, pp. 10941–6, May 2010.

[35] P. Dong, S. F. Preble, and M. Lipson, “All-optical compact silicon comb switch.,” *Optics express*, vol. 15, pp. 9600–5, July 2007.

[36] A. Knights and E. Huante-Ceron, “Comb-laser driven WDM for short reach silicon photonic based optical interconnection,” *Group IV Photonics*, vol. 2, pp. 210–212, 2012.

[37] T. Kippenberg, R. Holzwarth, and S. Diddams, “Microresonator-based optical frequency combs,” *Science*, vol. 332, no. April, pp. 555–559, 2011.

[38] A. Yariv, "Universal relations for coupling of optical power between microresonators and dielectric waveguides," *Electronics Letters*, vol. 36, no. 4, pp. 1–2, 2000.

[39] LUMERICAL, "Ring Resonator Tutorial — FDTD Solutions Knowledge Base."

[40] A. Yariv, Y. Xu, R. K. Lee, and A. Scherer, "Coupled-resonator optical waveguide: a proposal and analysis.," *Optics letters*, vol. 24, pp. 711–3, June 1999.

[41] J. Hryniewicz, P. Absil, B. Little, R. Wilson, and P.-T. Ho, "Higher order filter response in coupled microring resonators," *IEEE Photonics Technology Letters*, vol. 12, pp. 320–322, Mar. 2000.

[42] J. Poon, J. Scheuer, S. Mookherjea, G. Paloczi, Y. Huang, and A. Yariv, "Matrix analysis of microring coupled-resonator optical waveguides.," *Optics express*, vol. 12, pp. 90–103, Jan. 2004.

[43] J. K. S. Poon, J. Scheuer, Y. Xu, and A. Yariv, "Designing coupled-resonator optical waveguide delay lines," *Journal of the Optical Society of America B*, vol. 21, no. 9, p. 1665, 2004.

[44] S. Emelett and R. Soref, "Design and simulation of silicon microring optical routing switches," *Journal of lightwave technology*, vol. 23, no. 4, pp. 1800–1807, 2005.

[45] C. Madsen and J. Zhao, *Optical filter design and analysis: a signal processing approach.* John Wiley & Sons, 1999.

[46] S. Sze and K. Ng, *Physics of semiconductor devices.* 2006.

[47] R. Street, *Hydrogenated amorphous silicon.* 2005.

[48] D. Sparacin, R. Sun, a.M. Agarwal, M. Beals, J. Michel, L. Kimerling, T. Conway, a.T. Pomerene, D. Carothers, M. Grove, D. Gill, M. Rasras, S. Patel, and a.E. White, "Low-Loss Amorphous Silicon Channel Waveguides for Integrated Photonics," *3rd IEEE International Conference on Group IV Photonics, 2006.*, pp. 255–257, 2006.

[49] H. Hurwitz and R. Jones, "A new calculus for the treatment of optical systems i. description and discussion of the calculus," *J. Opt. Soc. Am*, 1941.

[50] G. Ghosh, "Model for the thermo-optic coefficients of some standard optical glasses," *Journal of Non-Crystalline Solids*, vol. 189, pp. 191–196, Aug. 1995.

[51] G. Ghosh, "Temperature dispersion of refractive indices in crystalline and amorphous silicon," *Applied physics letters*, vol. 66, no. 26, pp. 3570–3572, 1995.

[52] J. McCaulley, V. Donnelly, M. Vernon, and I. Taha, "Temperature dependence of the near-infrared refractive index of silicon, gallium arsenide, and indium phosphide," *Physical Review B*, vol. 49, no. 11, pp. 7408–7417, 1994.

[53] S. Wemple, “Refractive-index behavior of amorphous semiconductors and glasses,” *Physical Review B*, vol. 7, no. 8, 1973.

[54] G. Gulsen and M. N. Inci, “Thermal optical properties of TiO2 films,” *Optical Materials*, vol. 18, pp. 373–381, 2002.

[55] P. Alipour, A. Atabaki, A. A. Eftekhar, and A. Adibi, “Titania-clad microresonators on SOI with athermal performance,” *CLEO,OSA*, 2010.

[56] H. Ma, a.K. Y. Jen, and L. Dalton, “Polymer-Based Optical Waveguides: Materials, Processing, and Devices,” *Advanced Materials*, vol. 14, pp. 1339–1365, Oct. 2002.

[57] W. Groh and A. Zimmermann, “What is the lowest refractive index of an organic polymer?,” *Macromolecules*, vol. 24, pp. 6660–6663, 1991.

[58] V. Raghunathan, J. L. Yagüe, J. Xu, J. Michel, K. K. Gleason, and L. C. Kimerling, “Co-polymer clad design for high performance athermal photonic circuits,” *Optics Express*, vol. 20, p. 20808, Aug. 2012.

[59] J. T. Robinson, K. Preston, O. Painter, and M. Lipson, “First-principle derivation of gain in high-index- contrast waveguides,” *Optics Express*, vol. 16, no. 21, pp. 16659–16669, 2008.

[60] Y. Kokubun, S. Yoneda, and H. Tanaka, “Temperature-independent narrowband optical filter at 1.3 ÎÂ¼m wavelength by an athermal waveguide,” *Electronics Letters*, vol. 32, no. 21, pp. 1998–2000, 1996.

[61] Y. Kokubun, S. Yoneda, and S. Matsuura, “Temperature-independent optical filter at 1.55 ÎÂ¼m wavelength using a silica-based athermal waveguide,” *Electronics Letters*, vol. 34, no. 4, pp. 367–369, 1998.

[62] S. T. Chu, W. Pan, S. Suzuki, B. E. Little, S. Sato, and Y. Kokubun, “Temperature Insensitive Vertically Coupled Microring Resonator Add / Drop Filters by Means of a Polymer Overlay,” *IEEE Photonics Technology Letters*, vol. 11, no. 9, pp. 1138–1140, 1999.

[63] J.-M. Lee, D.-J. Kim, H. Ahn, S.-H. Park, and G. Kim, “Temperature Dependence of Silicon Nanophotonic Ring Resonator With a Polymeric Overlayer,” *Journal of Lightwave Technology*, vol. 25, pp. 2236–2243, Aug. 2007.

[64] N. Winnie, J. Michel, L. Kimerling, and L. Eldada, “Polymer-cladded athermal high-index-contrast waveguides,” *Proc. of SPIE Vol*, pp. 1–8, 2008.

[65] W. Ye, J. Michel, and L. Kimerling, “Athermal high-index-contrast waveguide design,” *IEE Photonics Technology Letters*, vol. 20, no. 11, pp. 885–887, 2008.

[66] W. Ye, J. Michel, L. Eldada, and D. Pant, “Thermo-optical Compensation In High-index-contrast Waveguides Using Polymer Claddings,” *Integrated Photonics Research, OSA*, pp. 3–5, 2008.

[67] W. Ye, R. Sun, and J. Michel, "Thermo-optical Compensation in High-index-contrast Waveguides," *Group IV Photonics*, pp. 1–3, 2008.

[68] J. Teng, P. Dumon, W. Bogaerts, H. Zhang, X. Jian, X. Han, M. Zhao, G. Morthier, and R. Baets, "Athermal Silicon-on-insulator ring resonators by overlaying a polymer cladding on narrowed waveguides.," *Optics express*, vol. 17, pp. 14627–33, Aug. 2009.

[69] L. Zhou, K. Kashiwagi, K. Okamoto, R. P. Scott, N. K. Fontaine, D. Ding, V. Akella, and S. J. B. Yoo, "Towards athermal optically-interconnected computing system using slotted silicon microring resonators and RF-photonic comb generation," *Applied Physics A*, vol. 95, pp. 1101–1109, Feb. 2009.

[70] M. M. Milošević, N. G. Emerson, F. Y. Gardes, X. Chen, a. a. D. T. Adikaari, and G. Z. Mashanovich, "Athermal waveguides for optical communication wavelengths.," *Optics letters*, vol. 36, pp. 4659–61, Dec. 2011.

[71] B. Guha, B. B. C. Kyotoku, and M. Lipson, "CMOS-compatible athermal silicon microring resonators.," *Optics express*, vol. 18, pp. 3487–93, Feb. 2010.

[72] H. Huang, S.-T. Ho, D. Huang, Y. Tu, and W. Liu, "Design of temperature-independent arrayed waveguide gratings based on the combination of multiple types of waveguide.," *Applied optics*, vol. 49, pp. 3025–34, June 2010.

[73] S. Lin, E. Schonbrun, and K. Crozier, "Optical manipulation with planar silicon microring resonators.," *Nano letters*, vol. 10, pp. 2408–11, July 2010.

[74] S. Lin and K. Crozier, "An integrated microparticle sorting system based on near-field optical forces and a structural perturbation," *Optics Express*, vol. 20, no. 4, pp. 1–7, 2012.

[75] G. Cocorullo, F. D. Corte, and L. Moretti, "Measurement of the thermo-optic coefficient of a-Si: H at the wavelength of 1500 nm from room temperature to 200 C," *Journal of Non-Crystalline Solids*, vol. 302, pp. 310–313, 2002.

[76] L. Eldada and L. Shacklette, "Advances in polymer integrated optics," *Selected Topics in Quantum Electronics*, vol. 6, no. 1, pp. 54–68, 2000.

[77] D. Chen, H. R. Fetterman, A. Chen, W. H. Steier, L. R. Dalton, W. Wang, and Y. Shi, "Demonstration of 110 GHz electro-optic polymer modulators," *Applied Physics Letters*, vol. 70, no. 25, pp. 3335–3337, 1997.

[78] Y. Shi, W. Lin, D. J. Olson, J. H. Bechtel, H. Zhang, W. H. Steier, C. Zhang, and L. R. Dalton, "Electro-optic polymer modulators with 0.8 V half-wave voltage," *Applied Physics Letters*, vol. 77, no. 1, pp. 1–3, 2000.

[79] W. H. Steier, A. Chen, S.-S. Lee, S. Garner, H. Zhang, V. Chuyanov, L. R. Dalton, F. Wang, A. S. Ren, C. Zhang, G. Todorova, A. Harper, H. R. Fetterman, D. Chen, A. Udupa, D. Bhattacharya, and B. Tsap, "Polymer electro-optic

devices for integrated optics," *Chemical Physics*, vol. 245, pp. 487–506, July 1999.

[80] A. Donval, E. Toussaere, R. Hierle, and J. Zyss, "Polymer based polarization insensitive amplitude modulator: conception, technology and demonstration," *Synthetic Metals*, vol. 115, pp. 21–27, Nov. 2000.

[81] M. Lee, Y. Min, and J. Ju, "Polymeric electrooptic 2X2 switch consisting of bifurcation optical active waveguides and a Mach-Zehnder interferometer," *IEEE Journal on Selected Topics in Quantum Electronics*, vol. 7, no. 5, pp. 812–818, 2001.

[82] X. Lu, D. An, L. Sun, Q. Zhou, and R. T. Chen, "Polarization-insensitive thermo-optic switch based on multimode polymeric waveguides with an ultralarge optical bandwidth," *Applied Physics Letters*, vol. 76, no. 16, p. 2155, 2000.

[83] U. Siebel, R. Hauffe, and K. Petermann, "Crosstalk-enhanced polymer digital optical switch based on a W-shape," *IEEE Photonics Technology Letters*, vol. 12, no. 1, pp. 40–41, 2000.

[84] V. Raghunathan, W. N. Ye, J. Hu, T. Izuhara, J. Michel, and L. Kimerling, "Athermal operation of silicon waveguides: spectral, second order and footprint dependencies.," *Optics express*, vol. 18, pp. 17631–9, Aug. 2010.

[85] R. Greiner and F. Schwarzl, "Thermal contraction and volume relaxation of amorphous polymers," *Rheologica acta*, vol. 23, pp. 378–395, 1984.

[86] T. Osada and M. Godwin, "International Technology Roadmap for Semiconductors: Interconnect," tech. rep., 2009.

[87] M. Gupta and K. Gleason, "Initiated chemical vapor deposition of poly (1H, 1H, 2H, 2H-perfluorodecyl acrylate) thin films," *Langmuir*, vol. 22, no. 10, pp. 10047–10052, 2006.

[88] K. Lau and K. Gleason, "Initiated chemical vapor deposition (iCVD) of poly (alkyl acrylates): an experimental study," *Macromolecules*, vol. 39, pp. 3688–3694, 2006.

[89] K. Lau and K. Gleason, "Initiated chemical vapor deposition (iCVD) of poly (alkyl acrylates): A kinetic model," *Macromolecules*, vol. 39, pp. 3695–3703, 2006.

[90] S. Brunauer, P. Emmett, and E. Teller, "Adsorption of gases in multimolecular layers," *Journal of the American Chemical Society*, vol. 60, no. 2, pp. 309–319, 1938.

[91] W. Beach, "A model for the vapor deposition polymerization of p-xylylene," *Macromolecules*, vol. 11, no. 1, pp. 72–76, 1978.

[92] P. J. Flory, *Principles of Polymer Chemistry.* Cornell University Press, 1953.

[93] A. Adamson and A. Gast, *Physical chemistry of surfaces.* John Wiley & Sons, 6th ed., 1997.

[94] V. Raghunathan, T. Izuhara, J. Michel, and L. Kimerling, "Stability of polymer-dielectric bi-layers for athermal silicon photonics.," *Optics express*, vol. 20, pp. 16059–66, July 2012.

[95] L. H. Lee and K. K. Gleason, "Cross-Linked Organic Sacrificial Material for Air Gap Formation by Initiated Chemical Vapor Deposition," *Journal of The Electrochemical Society*, vol. 155, no. 4, p. G78, 2008.

[96] L. Junyan, H. Ling, and Z. Yuansuo, "Synthesis and property investigation of three core-shell fluoroacrylate copolymer latexes," *Journal of Applied Polymer Science*, vol. 112, pp. 1615–1621, May 2009.

[97] C. D. Petruczok and K. K. Gleason, "Initiated Chemical Vapor Deposition-Based Method for Patterning Polymer and Metal Microstructures on Curved Substrates.," *Advanced materials*, vol. Early View, pp. 1–6, Sept. 2012.

[98] D. C. Corporate, "Specialty Monomers- DVB."

[99] MATBASE, "Commodity polymers- PMMA."

[100] S. Matsuo and M. Kiuchi, "Low temperature chemical vapor deposition method utilizing an electron cyclotron resonance plasma," *Jpn. J. Appl. Phys*, vol. 22, no. 4, pp. L210–L212, 1983.

[101] C. Doughty, D. Knick, J. Bailey, and J. E. Spencer, "Silicon nitride films deposited at substrate temperatures ¡ 100Â° C in a permanent magnet electron cyclotron resonance plasma," *Journal of Vacuum Science & Technology A: Vacuum, Surfaces, and Films*, vol. 17, pp. 2612–2618, 1999.

[102] K. Seaward, J. Turner, and A. Nel, "Role of ions in electron cyclotron resonance plasma-enhanced chemical vapor deposition of silicon dioxide," *Journal of Vacuum Science & Technology B: Microelectronics and Nanometer Structures*, vol. 13, no. 1, pp. 118–124, 1995.

[103] G. I. Isai, *ECR plasma deposited SiO2 and Si3N4 layers: A Room Temperature Technology.* PhD thesis, University of Twente, 2003.

[104] M. Dahimene, "The performance of a microwave ion source immersed in a multicusp static magnetic field," *Journal of Vacuum Science & Technology B: Microelectronics and Nanometer Structures*, vol. 4, p. 126, Jan. 1986.

[105] A. Melloni and A. Canciamilla, "Exploiting photosensitivity in chalcogenide-assisted integrated optics," *Integrated Photonics Research, OSA*, vol. 2, pp. 7–9, 2011.

[106] A. Canciamilla, F. Morichetti, S. Grillanda, P. Velha, M. Sorel, V. Singh, A. Agarwal, L. C. Kimerling, and A. Melloni, “Photo-induced trimming of chalcogenide-assisted silicon waveguides.,” *Optics express*, vol. 20, pp. 15807–17, July 2012.

[107] N. Carlie, J. D. Musgraves, B. Zdyrko, I. Luzinov, J. Hu, V. Singh, A. Agarwal, L. C. Kimerling, A. Canciamilla, F. Morichetti, A. Melloni, and K. Richardson, “Integrated chalcogenide waveguide resonators for mid-IR sensing: leveraging material properties to meet fabrication challenges.,” *Optics express*, vol. 18, pp. 26728–43, Dec. 2010.

[108] J. Hu, M. Torregiani, F. Morichetti, N. Carlie, A. Agarwal, K. Richardson, L. C. Kimerling, and A. Melloni, “Resonant cavity-enhanced photosensitivity in As2S3 chalcogenide glass at 1550 nm telecommunication wavelength.,” *Optics letters*, vol. 35, pp. 874–6, Mar. 2010.

[109] C. Lopez, *Evaluation of the photo-induced structural mechanisms in chalcogenide glass materials*. PhD thesis, University of Central Florida, 2004.

[110] K. Shimakawa, N. Yoshida, A. Ganjoo, Y. Kuzukawa, and J. Singh, “A model for the photostructural changes in amorphous chalcogenides,” *Philosophical Magazine letters*, vol. 77, no. 3, pp. 153–158, 1998.

[111] A. Ganjoo and K. Shimakawa, “DYNAMICS OF PHOTODARKENING IN AMORPHOUS CHALCOGENIDES,” *Journal of Optoelectronics and Advanced Materials*, vol. 4, no. 3, pp. 595–604, 2002.

[112] K. Tanaka, S. Kyohya, and A. Odajima, “Anomaly of the thickness dependence of photodarkening in amorphous chalcogenide films,” *Thin Solid Films*, vol. 111, no. 3, pp. 195–199, 1984.

[113] M. Bertolotti, F. Michelotti, P. Cherbari, M. Popescu, and S. Zamfira, “The kinetics of the laser induced structural changes in As2S3 amorphous films,” *Journal of Non-Crystalline Solids*, vol. 192 & 193, pp. 657–660, 1995.

[114] R. Street, “Non-radiative recombination in chalcogenide glasses,” *Solid State Communications*, vol. 24, pp. 363–365, 1977.

[115] H. Hisakuni and K. Tanaka, “Giant photoexpansion in As2S3 glass,” *Applied Physics Letters*, vol. 65, no. 23, p. 2925, 1994.

[116] B. Singh, S. Rajagopalan, and P. Bhat, “Giant photocontraction effect in amorphous chalogenide thin films,” *Journal of Non-Crystalline Solids*, vol. 36, pp. 1053–1059, 1980.

[117] K. Tanaka, “Photoexpansion in As2S3 glass,” *Physical Review B*, vol. 57, pp. 5163–5167, Mar. 1998.

[118] K. Tanaka, "Spectral dependence of photoexpansion in As2S3 glass," *Philosophical magazine letters*, no. April 2012, 1999.

[119] V. K. Tikhomirov, K. Asatryan, T. V. Galstian, R. Vallee, and a. B. Seddon, "Photoinduced volume changes related to photoinduced anisotropy in chalcogenide glasses," *Philosophical Magazine Letters*, vol. 83, pp. 117–124, Jan. 2003.

[120] Z. Yang, N. C. Anheier, H. a. Qiao, and P. Lucas, "Simultaneous microscopic measurements of photodarkening and photoexpansion in chalcogenide films," *Journal of Physics D: Applied Physics*, vol. 42, p. 135412, July 2009.

[121] N. Feng and G. Zhou, "Computation of Full-Vector Modes for Bending Waveguide Using Cylindrical PerfectlyMatched Layers," *Journal of Lightwave Technology*, vol. 20, no. 11, pp. 1976–1980, 2002.

[122] M. Hasegawa and K. Horie, "Photophysics, photochemistry, and optical properties of polyimides," *Progress in Polymer Science*, vol. 26, pp. 259–335, Mar. 2001.

[123] G. Coppola, L. Sirleto, I. Rendina, and M. Iodice, "Advance in thermo-optical switches: principles, materials, design, and device structure," *Optical Engineering*, vol. 50, no. 7, p. 071112, 2011.

[124] K. K. Lee, D. R. Lim, L. C. Kimerling, J. Shin, and F. Cerrina, "Fabrication of ultralow-loss Si/SiO(2) waveguides by roughness reduction.," *Optics letters*, vol. 26, pp. 1888–90, Dec. 2001.

[125] S. Spector and M. Geis, "Hybrid multi-mode/single-mode waveguides for low loss," *Integrated Photonics Research, OSA*, 2004.

[126] S. Xiao, M. H. Khan, H. Shen, and M. Qi, "Compact silicon microring resonators with ultra-low propagation loss in the C band.," *Optics express*, vol. 15, pp. 14467–75, Oct. 2007.

[127] Y. Vlasov and S. McNab, "Losses in single-mode silicon-on-insulator strip waveguides and bends.," *Optics express*, vol. 12, pp. 1622–31, Apr. 2004.

[128] F. Xia, L. Sekaric, and Y. Vlasov, "Ultracompact optical buffers on a silicon chip," *Nature Photonics*, vol. 1, pp. 65–71, Jan. 2007.

[129] P. Dumon and W. Bogaerts, "Low-loss SOI photonic wires and ring resonators fabricated with deep UV lithography," *IEEE Photonics Technology Letters*, vol. 16, no. 5, pp. 1328–1330, 2004.

[130] a. Canciamilla, M. Torregiani, C. Ferrari, F. Morichetti, R. M. De La Rue, a. Samarelli, M. Sorel, and a. Melloni, "Silicon coupled-ring resonator structures for slow light applications: potential, impairments and ultimate limits," *Journal of Optics*, vol. 12, p. 104008, Oct. 2010.

[131] V. Raghunathan, "High capacity, photo-trimmable athermal silicon waveguides," *Group IV Photonics*, vol. 7, pp. 45–47, 2012.

[132] S. Suzuki, K. Oda, and Y. Hibino, "Integrated-optic double-ring resonators with a wide free spectral range of 100 GHz," *Journal of Lightwave Technology*, vol. 13, no. 8, pp. 1766–1771, 1995.

[133] I. Kang, M. Rasras, X. Liu, S. Chandrasekhar, M. Cappuzzo, L. T. Gomez, Y. F. Chen, L. Buhl, S. Cabot, and J. Jaques, "All-optical OFDM transmission of 7 x 5-Gb/s data over 84-km standard single-mode fiber without dispersion compensation and time gating using a photonic-integrated optical DFT device.," *Optics express*, vol. 19, pp. 9111–7, May 2011.

[134] Z. Wang, K. S. Kravtsov, Y.-K. Huang, and P. R. Prucnal, "Optical FFT/IFFT circuit realization using arrayed waveguide gratings and the applications in all-optical OFDM system.," *Optics express*, vol. 19, pp. 4501–12, Feb. 2011.

[135] H. Sanjoh, E. Yamada, and Y. Yoshikuni, "Optical orthogonal frequency division multiplexing using frequnecy/time domain filtering for high spectral efficiency up to 1 bit/s/Hz," *OFC*, vol. ThD1, pp. 401–402, 2002.

[136] A. Sano, H. Masuda, E. Yoshida, T. Kobayashi, E. Yamada, Y. Miyamoto, F. Inuzuka, Y. Hibino, Y. Takatori, K. Hagimoto, T. Yamada, and Y. Sakamaki, "30 x 100-Gb/s all-optical OFDM transmission over 1300 km SMF with 10 ROADM nodes," *Optical Communications, ECOC, Post deadline submissions*, no. 1.7, pp. 5–6, 2007.

[137] D. Hillerkuss, M. Winter, M. Teschke, a. Marculescu, J. Li, G. Sigurdsson, K. Worms, S. Ben Ezra, N. Narkiss, W. Freude, and J. Leuthold, "Simple all-optical FFT scheme enabling Tbit/s real-time signal processing.," *Optics express*, vol. 18, pp. 9324–40, Apr. 2010.

# List of Publications Based on this Thesis

1. Vivek Raghunathan, Jeujun Hu, Winnie.N.Ye, Jurgen Michel and Lionel C.Kimerling, "Athermal Silicon Ring resonators", *Integrated Photonic Research, Silicon and Nanophotonics, Optical Society of America*, p.IMC5, 2010.

2. Vivek Raghunathan, Winnie.N.Ye, Jeujun Hu, Tomoyuki Izuhara, Jurgen Michel and Lionel C. Kimerling, "Athermal Operation of Silicon waveguides: spectral, second order and footprint dependencies", *Optics Express*, vol.18, no.17, pp.17631-17639, 2010.

3. Vivek Raghunathan, Tomoyuki Izuhara, Jurgen Michel and Lionel C. Kimerling, "Stability of polymer-dielectric bi-layers for athermal silicon photonics", *Optics Express*, vol.20, no.14, pp.16059-16066, 2012.

4. Vivek Raghunathan, Jose Luis Yague, Jingjing Xu, Jurgen Michel, Karen K. Gleason and Lionel C. Kimerling, "Co-polymer clad design for high performance athermal photonic circuits", *Optics Express*, vol.20, no.19, pp.20808-20813, 2012.

5. Vivek Raghunathan, Stefano Grillanda, Antonio Canciamilla, Vivek Singh, Francesco Morichetti, Anuradha.M.Agarwal, Jurgen Michel, Andrea Melloni and Lionel C. Kimerling, "Trimming of athermal Silicon Resonators", *Integrated Photonic Research, Silicon and Nanophotonics, Optical Society of America*, p.IW4C.5, 2012.

6. Vivek Raghunathan, Stefano Grillanda, Antonio Canciamilla, Vivek Singh, Francesco Morichetti, Anuradha.M.Agarwal, Jurgen Michel, Andrea Melloni and Lionel C. Kimerling, “High capacity photo-trimmable athermal silicon waveguides”, *IEEE International Conference on Group IV photonics*, WB7, pp.45-47, 2012.